Escola de Camins
Escola Tècnica Superior d'Enginyeria de Camins, Canals i Ports
UPC BARCELONATECH

TREBALL FINAL DE MÀSTER

ADVANCED MODELLING OF ADHESIVE BONDS IN AUTOMOTIVE COMPONENTS BY THE FINITE ELEMENT METHOD

Treball realitzat per:
Alfredo Alameda González

Dirigit per:
Dr. Riccardo Rossi
Eduardo Martín-Santos

Màster en:
Numerical Methods in Engineering

Barcelona, gener 2019

Departament d'Enginyeria Civil i Ambiental

UNIVERSITAT POLITÈCNICA DE CATALUNYA

ESCOLA TÈCNICA SUPERIOR D'ENGINYERS DE CAMINS, CANALS I PORTS DE BARCELONA

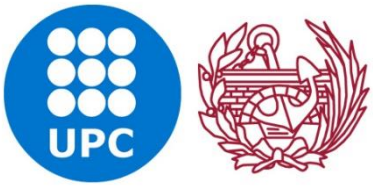

ADVANCED MODELLING OF ADHESIVE BONDS IN AUTOMOTIVE COMPONENTS BY THE FINITE ELEMENT METHOD

by

ALFREDO ALAMEDA GONZÁLEZ

MASTER ON NUMERICAL METHODS IN ENGINEERING

January 2019

Abstract

In the design of new components within the automotive framework, simulation methodologies are widely applied in order to reduce experimental costs. The growing trend in the industry includes new light weight designs and multi-material components. This leads to the need of considering some aspects in simulation, that were not required in the immediate past for the design of classical materials.

Among others, the use of structural adhesives has to be taken into account as a primary joining method above traditional procedures such as welds, bolts or rivets. This creates a need of improving the modelling of adhesively bonded joints between components, in order to get stable simulations and to include some effects, as partial or total de-bonding of parts during a crash event.

The main target of this work is to improve the adhesive joint modelling techniques, from the characterization of the material properties to its inclusion in adhesively bonded components. This methodology is validated by comparing the simulation results obtained from Finite Element Method (FEM) models with available experimental data from a series of both normalized and automotive-component related tests.

Acknowledgements

This Master Thesis is the culmination of an effort that began years ago, when I was an inexperienced engineer that wanted to give meaning to his carrer. I would like to thank all the people that, to a greater or lesser extent, have contributed to the realization of this purpose. Dr. Emilio Martínez Pañeda firstly was the responsible for introducing me the topic of numerical methods and the importance of the Finite Element Method as one of the most advanced engineering techniques nowadays. Without his friendship and his selfless advice nothing of this could have been possible or even conceivable.

I wish to thank Mònica Cartanyà and Eduardo Martín-Santos, from the Body Development department of the company Applus IDIADA for the trust they placed on me, and the rest of the exceptional engineers from the Materials Science and Industrial Vehicle teams – specially to Alejandro Domínguez – for sharing with me all their knowledge and their outstanding expertise. I hope everything I have learned next to them is just a small portion of what is left.

And above all, I would like to thank Sara for her admirable understanding, her priceless support and all her affection and patience during these long years. Unlike the concepts treated in this work, my immense appreciation and love to her cannot be expressed with numbers.

Contents

List of figures and tables

Figure 8.14: Comparison of results obtained from roof opening tests performed on models A and B

Chapter 1

Introduction and Objectives

The purpose of this first chapter is to briefly review the evolution in the use of numerical methods for crash simulations in the automotive industry, highlighting its growing importance and its undeniable utility nowadays. Next the motivations on which this thesis is based, as well as the main objectives to be achieved are exposed. Finally, a summary of the following chapters into which this work has been divided is presented.

1.1. Background

The enormous progress accomplished in recent times in the field of numerical methods and the evolution in computational power and efficiency – both at hardware and software level – has radically changed the process of component design and development in the automotive industry. The predictions obtained by means of these techniques are increasing in reliability and therefore are more and more used in an extensive way throughout the decision-making process in these days.

However, the growing integration of numerical simulations in industrial design increases their reliability requirements. In many automotive engineering fields like development of vehicle occupant protection systems, material fatigue analysis or pedestrian safety, the obtention of accurate results is fundamental, so constant research and development in this regard is of vital importance. This becomes specially critical in some regulations for homologations, which can be surpassed only by simulation, not requiring experimental tests or correlation.

Several years ago it was necessary to build a large series of physical prototypes during each and every one of the development phases of a vehicle. These were built without integrating a corresponding numerical approach, relegating simulation to play a secondary role in the industry. Numerical methods had a specific character, focused on solving very specific problems, or they served just as a guide when looking for possible strategies to follow.

Nowadays every car manufacturer company uses a wide variety of numerical software for the development of their products, specifically those that make use of the Finite Element Method (FEM) to perform crash simulations. One of the most used, specially for crash-related disciplines, is commercial software LS-Dyna®, which is based on a explicit time integration scheme.

Starting from an initial vehicle concept, the physical behaviour of the vehicle is characterized by several material models as well as by the creation of different boundary conditions and other characteristics. In this way all the effects and interactions on the car body, its occupants or other possible external agents are properly captured and analyzed, facilitating the decision-making process and thus, reducing the component developing costs.

1.2. Motivation

One of the main challenges nowadays is the accurate prediction of the failure in the structural parts of the vehicle. The introduction of new materials (high-strength steels, aluminum, composites) is aimed at lightening the weight of the structure, seeking to reduce fuel consumption. This is specially critical with the increasing implementation of electric motors, whose power train represents a remarkable increase in the total weight of the vehicle.

The traditional joining methods in the industry – such as welds, bolds or rivets – are a significant barrier to the abovementioned trend towards lightweight, multimaterial automotive design. Besides, improvements in performance and strength of structural adhesives in the last years make adhesive bonding to become of a special importance. Therefore, a special emphasis must be made on the adequate numerical representation of the physical behaviour in these components.

A proper numerical simulation involves an adequate characterization of the materials that belong to the component. In first place, the material type must be identified and a numerical model must be proposed. This has to be capable of adequately capturing, according to the needs of the analyst and the available means, the physics of the component. Next, the experimental tests necessary to collect the data that allow to calibrate the material model parameters must be performed. Once calibrated, the model is validated using component tests. It is after this process that the material model is ready to take part in full vehicle crash simulations.

In the case of structural adhesives, a suitable material model must be characterized by:

- A reliable computation of stresses on the adhesive layer.
- An accurate description of the failure.
- Good efficiency in terms of computational cost.
- A simple identification and calibration of material parameters.

1.3. Objectives

The main objective of this thesis is the proposal of a methodology for the inclusion of accurate definitions for the simulation of structural adhesive joints. By means of this, plasticity and damage in adhesives are intended to be included in the vehicle crash-related design, improving its reliability. For this, the Finite Element Method is proposed. Due to its wide extension of application in the automotive framework, the LS-Dyna sofware is selected.

The proposed methodology is based on experimental data collected after performing simple, normalized tests that create homogeneous stress states on the adhesive layer. These will allow the understanding first and the characterization of the behaviour of certain structural adhesives under pure (normal and shear) and combined stress conditions. Finally, a material card is created, being able to reproduce the different effects observed in the characterization campaign. In addition, the use of contacts and cohesive elements for the stable modelling of adhesive layers is also examined troughout this work.

The obtained material card together with the exposed procedures will then be used in the simulation of component-level models that will allow us to accomplish a complete characterization of the material and to explore the possibilities and performance of the adhesive modelling technique.

The extensive application of the developed methodology will then suppose an enormous increase in the efficiency and reliability of crash simulations. By means of this, the vehicle design is improved, being more precise by simulation and thus, reducing time and computational cost.

1.4. Outline of the Thesis

After this introductory chapter in which the motivations and the objectives to be achieved in this thesis have been presented, in chapter number two a brief study is made, through specialized literature, of the current technologies within the adhesive bonding framework. Chapter number three contains an overview of the Finite Element Method, that is the numerical method in which the further explained simulation techniques are based.

At the fourth chapter the main mathematical approaches for modelling the physical behaviour of adhesives are exposed. Next, along chapters number five and six, the state of the art in material modelling of structural adhesives using LS-Dyna® is presented, followed by a the proposal of a methodology for the modelling of adhesive layers in FEM simulations.

Chapter seven describes the different test specimens used in order to characterize a structural adhesive, showing an exposition of the simulation results compared to the collected experimental

data. Chapter eight shows a series of component-level models used in order to validate the created methodology. Finally, in chapter number nine, the reached conclusions after the completion of this Master Thesis are presented and possible future lines of research to be worked on are proposed.

Chapter 2

Literature Review on Adhesives

The objective of this chapter is to provide the reader with a brief approach to adhesives technology through the study of specialized literature. This will be done without addressing the numerical simulation of their physical behaviour at the moment, which will be the subject of the following chapters. For this, a short introduction about adhesive materials occupies the first section. Below the basic concepts and the most relevant adhesion theories are presented. Later, the stress mechanisms acting on adhesive joints will be briefly discussed. Finally, an approach to the considerations in the design of adhesive joints is introduced.

2.1. Overview

Adhesives surround us both in nature and in our daily lives. They have been used for centuries, when first adhesive joints were made through the use of materials directly taken from nature, such as tree sap, bee wax or tar. Subsequently, processed products were used from animal proteins, resins or natural rubbers, as latex. With the subsequent development of the chemical industry and synthetic polymers, capacity of adhesive materials has been increased enormously in both typology and variety of applications.

Nowadays, hundreds of companies are engaged in developing, manufacturing and advertising a wide range of this type of products, which are used in virtually any facet of human activity. From the most common office material to the most cutting-edge computer hardware, passing through the textile industry, construction or manufacturing of automotive and aeronautical components. Many of the elements that are part of our current life could not exist if it were not for the adhesive bonding technology.

In recent years, the execution of joints by means of adhesives in structural components has increased remarkably. This is specially caused by the apparition of components manufactured in advanced materials, as fibre reinforced composites or aluminum. Traditional mechanical joining (such as welding or bolts) results in fibre cutting and therefore in a large concentration of stresses at the junctions. All this contributes to a notable reduction in the structural integrity of the component due to size-related effects. Adhesive bonding methods however are an alternative that produces continuous and lightweight joints, which also offer the possibility of being manufactured in an easy

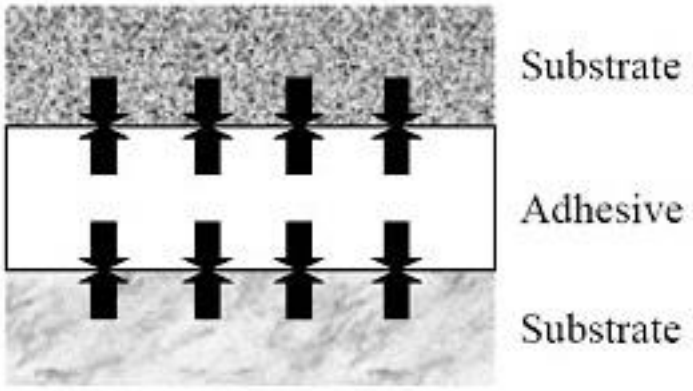

Figure 2.1: Schematic view of attractive forces (adhesion) between dissimilar surfaces (adhesives.org)

and versatile way. As previously discussed, adhesive joining has become a main technique in leading industries such as aeronautics and aerospace, automotive, electronics, and has begun to be an alternative increasingly demanded in more traditional industries such as construction.

2.2. Basic concepts on adhesives

An adhesive material can be defined as a non-metallic substance that, placed between two surfaces (also known as adherends or substrates), solidifies to produce a material bond between them. Another possible definition is that of a substance capable of maintaining at least two surfaces together in a firm and durable manner. The concept of 'adhesive' should not be confused with that of 'sealant', since despite being two similar materials in terms of appearance and chemical composition, the latter are defined as substances capable of joining two or more surfaces filling the space between them in such a way as to provide a protective barrier against external erosive agents.

Both adhesive materials and sealants share the following characteristics:

- They must behave like a liquid at some point in the joining process, so that they can be molded and 'moisten' the surfaces to be bonded. In other words, they must create a close contact with said surfaces.

- They create a superficial bond between the substrates by means of adhesion mechanisms (development of intermolecular forces).

- They have to be hardened in order to support variable and continuous loads throughout their lifetimes.

- They transfer and distribute the loads between the joined components, working together with them in order to provide a lasting bond.

- They have to fill the possible gaps, cavities, imperfections or existing spaces between the substrates.

Despite having so much in common, adhesives usually show higher mechanical properties than sealants. Thus, adhesives are chosen for showing high resistance to pure tensile and pure shear stress. This leads us to the particularization of 'structural adhesives', which will be the subject of this thesis from now on.

This term is reserved for those adhesives designed to be used in engineering applications for being able to withstand large tangential stresses, usually greater than 6-10 MPa, in a static or cyclical way for long periods of time. Examples of this type of adhesives are epoxies, thermosynthetic acrylics, polyurethanes, etc. For a proper design, it is also expected that structural adhesives have a longer lifetime than the elements to be joined.

2.3. Adhesion/cohesion theory

The functioning of an adhesive bond is based on the concepts of the adhesion / cohesion theory. First, adhesion is the force that holds substrates and adherends together in opposition to the stresses exerted to separate them. In other words, it is an attraction between two substances of different nature that results from the appearance of intermolecular forces (van der Waals forces) between them. Figure 2.1 shows a schematic view of this mechanism.

Second, cohesion is the attraction of intermolecular type between the particles of the adhesive itself (or any other material) that keeps such body as a united entity, as can be seen schematically in Figure 2.2.

The capability to bear the combination of adhesion and cohesion efforts determine the effectiveness of an adhesive bond. In this way, a bond of this type will fail both if the adhesive is separated from the substrate (adhesive failure) or if the adhesive becomes damaged itself (cohesive failure). The latter might exist both within the adhesive and the substrate. In the cohesive failure of the adhesive, the failure strength cause a layer of adhesive to remain attached to each of the substrates, since the adhesive fixation to the substrate is stronger than the cohesive resistance of the adhesive itself. Occasionally, when the adhesive and cohesive Ultimate Strengths in the adhesive are

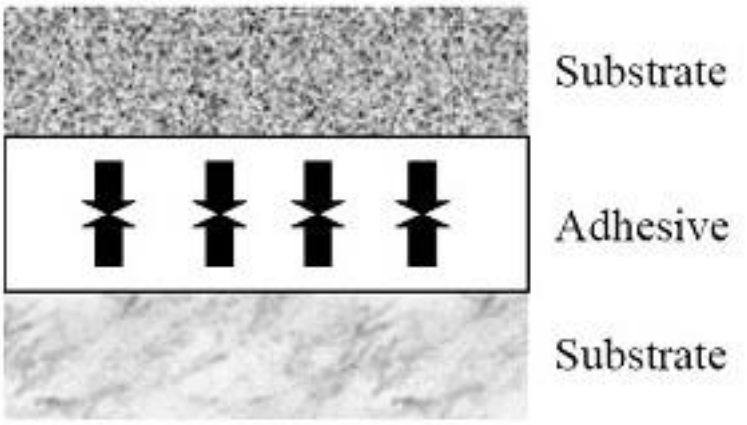

Figure 2.2: Schematic view of the internal strength (cohesion) inside a material (adhesives.org)

sufficiently large, the substrate fails before the adhesive and the bond area remains intact. Then we speak of cohesive failure of the adherend. Figure 2.3 shows schematically the different failure modes.

2.4. Types of stresses on an adhesive joint

As stated above, one of the decisive variables when designing an adhesive joint is the type and magnitude of the stresses that this is required to hold. The four main types of stresses that may appear in a joint are described next.

On the one hand, pure stress modes (normal and shear stress) allow the full bonded area to work and to contribute to the joint strength. On the contrary, peel and cleavage stress create situations where forces are concentrated on a small portion of the joint, causing damage and failure in the adhesive at much lower levels than expected if pure normal or shear type of stresses happened. Figure 2.4 shows the four different types of loads introduced in this section.

In the case of normal stress, the direction of the force is exerted in a direction perpendicular to the plane of the joint and in a distributed manner throughout its extension. In the case of shear stress, the direction of the force is contained in the plane of the joint, and causes one of the substrates to slide parallel to the opposite one. Most of the adhesives show a better performance when main stresses on the joint are of the normal and shear types.

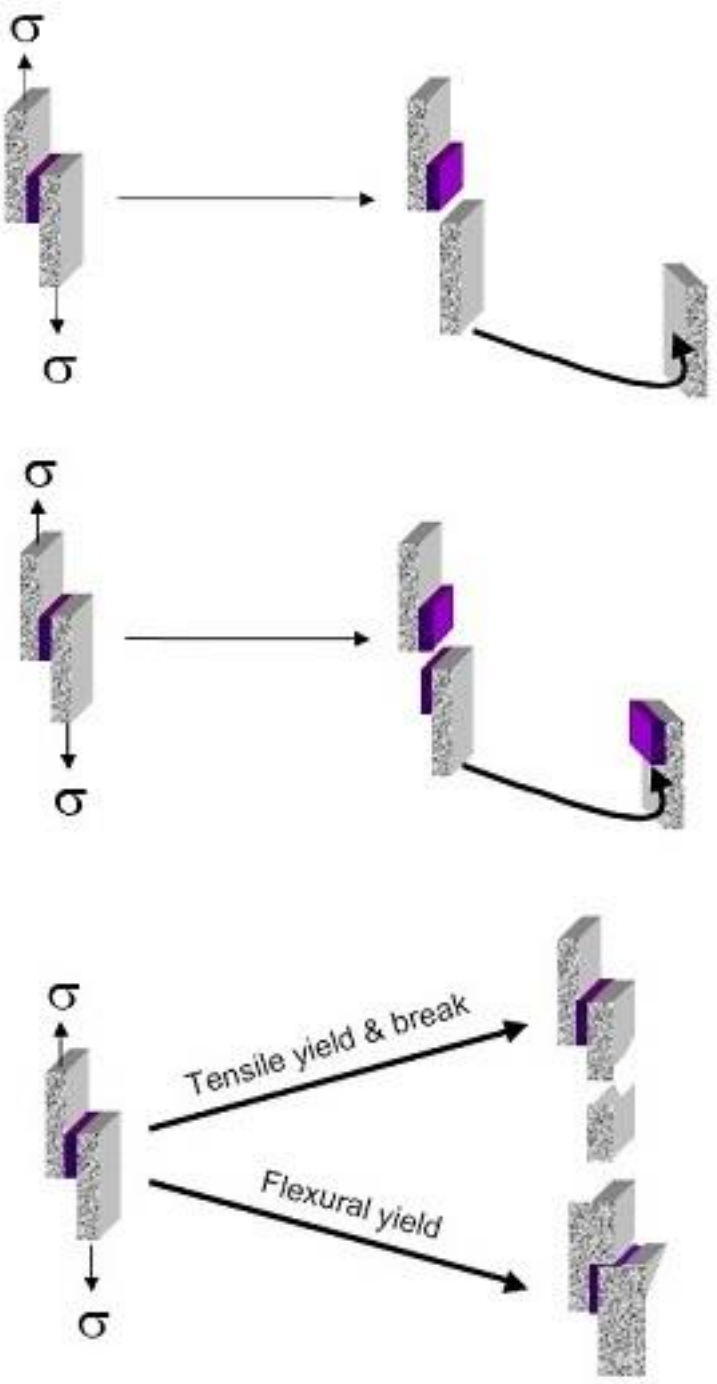

Figure 2.3: Schematic view of the different failure modes of an adhesive bond. From top to bottom: adhesive failure, cohesive failure and cohesive failure of the substrate. (adhesives.org)

However, in most service conditions adhesives finally behave in complex stress states – i.e. peel and cleavage stresses. In the case of cleavage stress, the force is concentrated on one of the two ends of the joint, creating a leverage effect with its support at the opposite end. Theoretically, this

side is subjected to a stress equal to zero. In the case of peel stress, force is concentrated entirely along a line of flexible substrate at the end of the adhesive joint.

2.5. Design of adhesive bonds

Design of adhesive bonds is an complex process involving a large number of variables and boundary conditions, as well as a series of unforeseen events that can result in a total failure of the joint.

In addition to the benefits they provide when manufacturing certain types of products, this type of joints are increasingly used in certain industries as a substitute for mechanical joining (bolts and rivets) and welding, since they provide a series of advantages to be considered. In addition, the constant process of research and development in the industry translates into a continuous increase in the versatility and the resistant capacity of this type of materials.

Adhesives usually generate a strong bond at low temperatures in a great part of substrates with different coefficients of thermal expansion or thermal conductivity among themselves, which otherwise would make welding impossible. Many polymeric adhesives are viscoelastic and behave like tough, relatively flexible materials, with the ability to expand or contract. This allows the bonding between materials with different stiffnesses. Toughness defines the joint with resistance to thermal cycles and the propagation of cracks. Besides, adhesive joints distribute the stresses between the substrates in a uniform way, eliminating the local stresses that can appear by other bonding methodologies – i.e. welding, mechanical fasteners...

Adhesives show great advantages for component design. Unlike what happens with bolted or riveted joints, adhesives generate smoother contours without interferences, beneficial from an aerodynamic and aesthetic point of view. In addition, they also offer better specific properties than other methods of mechanical fastening. Certain substrates showing small dimensions (specially on the thickness) usually lead to large distortion in the manufacturing process, if other methods as welding are applied. This is the reason why a large part of medical or microelectronic precision products are often bonded by adhesives. In comparison with methods such as rivets or fasteners, the reduction in the number of perforations to be made in the chain production of certain components can also lead to considerable cost savings.

Certain additional properties of the adhesives should not to be overlooked, since in addition to mechanical bonding they can lead to other design improvements: they can be used as sealants, vibration dampers, noise, thermal or electrical insulators and filler of gaps in a joint, all in one single product.

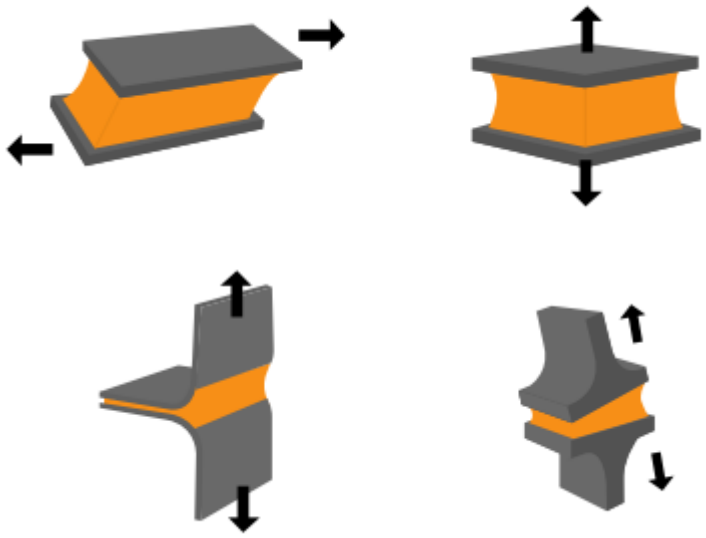

Figure 2.4: Schematic view of the different types of stresses appearing on an adhesive bond (from left to right and from top to bottom) pure shear, pure normal, peel and cleavage. (3m.com)

However, it must be borne in mind that the most serious limitation regarding the use of polymeric adhesives is that their strength is easily degradable under certain environmental conditions such as humidity, high temperatures or the presence of chemical agents. This strength will be even more rapidly degraded if the component is subjected to cyclical stresses. Thus, all these drawbacks must be taken into consideration in the design process of a component, and the chosen adhesive should provide a longer useful life than that of the substrates. In practically all structural adhesives, the direction in which the stresses act is more decisive than in the mechanized joints. As already mentioned above, adhesives work correctly under normal and shear type forces, but their performance is greatly reduced under cleavage and peel stresses. In addition, slow and critical processing requirements of some adhesives can be a major disadvantage particularly in high-volume production operations. Several production concerns must be considered when bonding operations are first projected. All adhesives require clean surfaces to obtain the optimal results. If adhesive has multiple components, they must be carefully weighed and mixed. Rigid process controls are also necessary because adhesive properties are dependent of curing parameters and surface preparations. All these disadvantages contribute to a "hidden cost" of using adhesives, and they have to be carefully predicted and evaluated during the design process.

Beyond the properties of the adhesive or substrate material, and the loads existing on the joint, the key factor for the satisfactory functioning of an adhesive union is its geometric design. A key principle in engineering is the design of components capable of transmitting forces as well as of

supporting stresses of different nature over extended periods of time. Therefore, sufficiently large joint areas have to be created and excessive load concentrations within the joint must be prevented. For all these reasons, it is the designer's task to evaluate all these variables and decide in which cases an adhesive bond is the ideal solution to the existing needs.

There are a large number of advantages in combining adhesive and mechanical joints, since results of this combination are superior to any of the separate methods. For instance, within the aeronautical framework it is common to find adhesives reinforced by rivets. In this case, the adhesive can distribute the load, avoiding stress concentration on the rivets and often is also used as sealant, sealing up the holes required in rivet welding.

Chapter 3

Overview of the Finite Element Method

The Finite Element Method (FEM) is nowadays the most extended numerical technique in the field of solid mechanics for determining an approximated solution for the equations of motion in complex geometries. These usually appear in the form of differential equations. The method is used in order to analyze a wide range of complex problems in any field of civil, mechanical, aeronautical or biomedical engineering, among others. Its implementation in commercial softwares provides for design engineers with simple and powerful computational procedure for the analysis of continuous systems with arbitrary geometries and material properties subjected to any type of loading.

Generally speaking, the FEM consists in the transformation of a continuous system with an infinite number of degrees of freedom into a equivalent, discrete one, with an approximate geometry and physical properties, but with a finite number of degrees of freedom. The accuracy of the computed solution will depend on the used degree of approximation. Such degrees of freedom are related to the external forces (or any other disturbance) by means of a system of algebraic equations representing the general equilibrium state of the structure.

The process of design, modelling and solution of any engineering problem can be summarized by means of the flowchart shown in Figure 3.1.

The present chapter briefly discusses the derivation of the weak form of the motion equations, its spatial discretization as well as the approximation of the integral equations.

3.1. Weak form of the balance equation

D'Alembert's principle is a statement of the fundamental classical laws of motion. It states that the sumatory of the differences between the forces acting on a system of mass particles and the time derivatives of the momenta, projected onto any virtual displacement is zero. This principle transforms the differential equation of the local equilibrium of moments into a scalar integral equation.

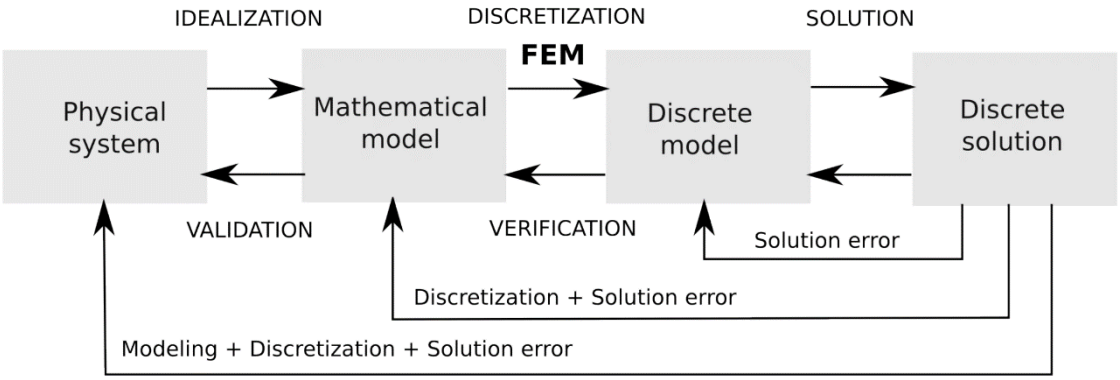

Figure 3.1: Flowchart of the process followed in order to find a solution to a raised engineering problem by means of the Finite Element Method (Salas A., Damage and modelling of composite materials for the automotive industry, 2017)

Since no further assumptions are made, this procedure is general and applicable, for example, to problems with friction, contact or inelastic material behaviour. The establishment of the so-called weak form of the moment balance equation begins with the local equilibrium equation in the instantaneous configuration $\chi(\mathfrak{B})$ and the boundary conditions regarding displacement $\bar{\boldsymbol{u}}$ and a stress vector $\bar{\boldsymbol{t}}$ on the corresponding boundaries $\partial\mathfrak{B}_u$ and $\partial\mathfrak{B}_\sigma$,

$$\rho\dot{\boldsymbol{v}} = \operatorname{div}\boldsymbol{\sigma} + \mathbf{k}_\mathrm{f}\rho \tag{3.1}$$

$$\begin{aligned} \mathbf{u} &= \bar{\mathbf{u}} \text{ on } \partial\mathfrak{B}_\mathrm{u} \\ \boldsymbol{\sigma}\,\mathbf{n} &= \bar{\mathbf{t}} \text{ on } \partial\mathfrak{B}_\sigma \end{aligned} \tag{3.2}$$

Where ρ is a scalar indicating density, $\boldsymbol{\sigma}$ is a tensor which describes the stress state of the system, $\dot{\boldsymbol{v}}$ and $\mathbf{k}_\mathrm{f}$ are vectors representing the material derivative of velocity and body forces respectively.

In order to set up the weak form, the equilibrium equation is multiplied by a vector-valued virtual displacement scalar δu. The subsequent integration of the local balance equation with the virtual displacement δu over the body volume $\chi(\mathfrak{B})$ leads to the functional representing the variational problem:

$$\delta\Pi_{\chi(\mathfrak{B})} = \int_{\chi(\mathfrak{B})} \operatorname{div}\boldsymbol{\sigma}\cdot\delta\mathrm{u}\;\mathrm{d}V + \int_{\chi(\mathfrak{B})} \rho(\mathbf{k}_\mathrm{f} - \dot{\mathbf{v}})\cdot\delta\mathrm{u}\;\mathrm{d}V = 0 \tag{3.3}$$

Subsequent partial integration of the first term of the previous equation and the application of the Gauss integral theorem, as well as the incorporation of the stress boundary condition from the beginning becomes:

$$\delta\Pi_{\chi(\mathfrak{B})} = \int_{\chi(\mathfrak{B})} \boldsymbol{\sigma} \cdot \operatorname{grad}\delta\mathrm{u}\ \mathrm{d}V - \int_{\chi(\mathfrak{B})} \rho(\mathbf{k}_\mathrm{f} - \dot{\mathbf{v}}) \cdot \delta\mathrm{u}\ \mathrm{d}V - \\ - \int_{\chi(\partial\mathfrak{B}_\sigma)} \overline{\mathbf{t}} \cdot \delta\mathrm{u}\ \mathrm{d}A = 0 \tag{3.4}$$

The scalar product $\boldsymbol{\sigma} \cdot \operatorname{grad}\delta u$ can be obtained by exploiting the symmetry properties of the Cauchy stress tensor:

$$\boldsymbol{\sigma} = \boldsymbol{\sigma}^{\mathrm{T}} \tag{3.5}$$

The expression is thus simplified so that only the symmetric component is used for the gradient of the virtual displacement grad δu:

$$\nabla^{\mathrm{S}}\delta\mathbf{u} = \operatorname{sym}(\operatorname{grad}\delta\mathrm{u}) = \frac{1}{2}[\operatorname{grad}\delta\mathrm{u} + \operatorname{grad}^{\mathrm{T}}\delta\mathrm{u}] \tag{3.6}$$

The previous functional, together with the symmetric nabla operator ∇^S in the above equation leads to D'Alembert's principle in the instantaneous configuration:

$$\delta\Pi_{\chi(\mathfrak{B})} = \int_{\chi(\mathfrak{B})} \boldsymbol{\sigma} \cdot \nabla^{\mathrm{S}}\delta\mathrm{u}\ \mathrm{d}V - \int_{\chi(\mathfrak{B})} \rho(\mathbf{k}_\mathrm{f} - \dot{\mathbf{v}}) \cdot \delta\mathrm{u}\ \mathrm{d}V - \int_{\chi(\partial\mathfrak{B}_\sigma)} \overline{\mathbf{t}} \cdot \delta\mathrm{u}\ \mathrm{d}A = 0 \tag{3.7}$$

The previous expression can be divided into the virtual work due to the internal forces δW_{int} and, on the other hand, the virtual work due to the volume and surface external loads δW_{ext}:

$$\delta W_{\mathrm{int}} = \int_{\chi(\mathfrak{B})} \boldsymbol{\sigma} \cdot \nabla^{\mathrm{S}}\delta\mathrm{u}\ \mathrm{d}V \tag{3.8}$$

$$\delta W_{\mathrm{ext}} = \int_{\chi(\mathfrak{B})} \rho\mathbf{k}_\mathrm{f} \cdot \delta\mathrm{u}\ \mathrm{d}V + \overline{\mathbf{t}} \cdot \delta\mathrm{u}\ \mathrm{d}A \tag{3.9}$$

3.2. Spatial discretization

In the previous section the derived variational equation represents the weak form of the moment balance equation; the solution to this equation can be satisfied only in the integral form. The solution of these equations over the whole computational area, that is to say the region of interest of the body $\mathfrak{B}$ to be examined, is in most practical applications not completely solvable. For this reason,

numerical methods are developed and used. In this case the Finite Element Method (FEM) provides an approximate but reliable solution to the problem.

The approximations to the exact solution include the geometric discretization of the body $\mathcal{B}$ by means of a division into n_e finite elements, the element-wise choice of shape functions N_I with a finite number of degrees of freedom (e.g. strains and stresses) and the approximate solution of the corresponding volume and area integrals. There should be no overlap between individual (or finite) elements. Each individual element Ω_e is composed of n_k discrete points, the so-called nodes, normally located at the element vertices.

Most FE solvers use isoparametric elements. These use the same shape functions for the description of the displacement field $\boldsymbol{u}$ over the element and for the interpolation of the element kinematics (e.g. element geometry in the output configuration $\boldsymbol{X}$ or the instantaneous configuration $\boldsymbol{x}$). For this, the displacement field $\boldsymbol{u}$ for an element e can be approximated using the mapping functions N_I and the node displacement vectors $\mathbf{u}_I^{\mathrm{k}}$ via the relationship:

$$\mathbf{u} \approx \mathbf{u}^{\mathrm{h}} = \sum_{I=1}^{n_k^e} N_I \, \mathbf{u}_I^{\mathrm{k}} = \mathbf{N}\mathbf{u}^{\mathrm{k}} \tag{3.10}$$

with $I = 1, \ldots, \mathrm{n}_{\mathrm{e}}^{\mathrm{k}}$ (where $\mathrm{n}_{\mathrm{e}}^{\mathrm{k}}$ is the number of nodes in the element). In the previous equation, the superscript h indicates the approximated field size and the superscript k indicates the field size at an element node. In the same way, the motion equations:

$$\mathbf{x} = \boldsymbol{\chi}(\mathbf{X}, t) \tag{3.11}$$

$$\mathbf{X} = \boldsymbol{\chi}^{-1}(\mathbf{x}, t) \tag{3.12}$$

of an isoparametric element are used together with the kinematic parameters for the approximation of the initial and instantaneous configuration:

$$\mathbf{X}^{\mathrm{h}} = \sum_{I=1}^{n_k^e} N_I \, \mathbf{X}_I^{\mathrm{k}} = \mathbf{N}\mathbf{X}^{\mathrm{k}} \tag{3.13}$$

$$\mathbf{x}^{\mathrm{h}} = \sum_{I=1}^{n_k^e} N_I \, \mathbf{x}_I^{\mathrm{k}} = \mathbf{N}\mathbf{x}^{\mathrm{k}} \tag{3.14}$$

The shape functions N_I are usually formed by polynomial expressions depending on the values of the unknown at the nodes of the element. They must also satisfy certain continuity

requirements over the element surface. By inserting the approximation expressed by Eqs. (3.10), (3.13) and (3.14) into the variational equation (3.7) one obtains the spatially discretized weak form of the moment balance equation, with the approximated volume integral:

$$\int_{\chi(\mathfrak{B})} (.)\mathrm{d}V \approx \int_{\chi(\mathfrak{B}^{\mathrm{h}})} (.)\mathrm{d}V^{\mathrm{h}} = \bigcup_{e=1}^{n_e} \int_{\chi(\Omega_e)} (.)\mathrm{d}\Omega \tag{3.15}$$

The solutions of the weak form (3.7) with the spatial discretization (3.15) generally do not fulfill exactly the initial moment balance equation. The operator ∪ represents the addition of the individual element integrals Ω_e over the entire discretized volume of the body $\mathfrak{B}^h$ consisting of n_e elements. For a complete discretization of the weak form in the instantaneous configuration, it is necessary to calculate the virtual inner work δW_{int} and the virtual work of volume and surface loads δW_{ext} to the spatial discretization form.

In this work, the description of material models for the description of structural adhesives and its modelling is primarily exposed, which is why only the discretization of the virtual inner work δA_{int} is described in detail for the instantaneous configuration. All the other terms can be transformed in the same way.

Into the virtual inner work δW_{int} of the instantaneous configuration, the symmetrical gradient of the virtual displacements $\nabla^S \delta \boldsymbol{u}_{\mathrm{e}}$ from Eq. (3.6) is used for a finite element e,

$$\nabla^{\mathrm{S}} \delta \mathbf{u}_{\mathrm{e}} = \sum_{I=1}^{n_k^e} \begin{bmatrix} N_{I,1} & 0 & 0 \\ 0 & N_{I,2} & 0 \\ 0 & 0 & N_{I,3} \\ N_{I,2} & N_{I,1} & 0 \\ 0 & N_{I,3} & N_{I,2} \\ N_{I,3} & 0 & N_{I,1} \end{bmatrix} \begin{bmatrix} \delta u_1^{\mathrm{k}} \\ \delta u_2^{\mathrm{k}} \\ \delta u_3^{\mathrm{k}} \end{bmatrix} = \sum_{I=1}^{n_k^e} \mathbf{B}_I \delta \mathbf{u}_I^{\mathrm{k}} \tag{3.16}$$

with the abbreviation:

$$N_{I,i} = \frac{\partial N_I}{\partial x_i} \tag{3.17}$$

The index $i = 1, \ldots 3$ indicates the coordinate directions of the spatial configuration. The virtual inner work (3.8) increases with Eqs. (3.15) and (3.16) taking the following form for FE elements:

$$\delta W_{\text{int}}^{\text{h}} = \bigcup_{e=1}^{n_e} \sum_{I=1}^{n_k^e} \delta \mathbf{u}_I^k{}^{\text{T}} \int_{\chi(\Omega_e)} \mathbf{B}_I^{\text{T}} \boldsymbol{\sigma} \, \text{d}\Omega \tag{3.18}$$

The integral in the above equation can be interpreted as a vector of internal forces $\mathbf{f}_{\text{int}\,I}^{\text{h}}(\mathbf{u}^{\text{h}})$:

$$\mathbf{f}_{\text{int}\,I}^{\text{h}}(\mathbf{u}^{\text{h}}) = \int_{\chi(\Omega_e)} \mathbf{B}_I^{\text{T}} \boldsymbol{\sigma} \, \text{d}\Omega \tag{3.19}$$

For the entire structure, the vector of internal forces then becomes:

$$\mathbf{f}_{\text{int}}^{\text{h}}(\mathbf{u}^{\text{h}}) = \bigcup_{e=1}^{n_e} \{ \sum_{I=1}^{n_k^e} \int_{\chi(\Omega_e)} \mathbf{B}_I^{\text{T}} \boldsymbol{\sigma} \, \text{d}\Omega \tag{3.20}$$

The stress state, represented by the vector $\boldsymbol{\sigma}^{\text{T}} = [\sigma_{11}\ \sigma_{22}\ \sigma_{33}\ \sigma_{12}\ \sigma_{23}\ \sigma_{13}]$ in the Voigt notation, must be calculated at the element level by means of suitable constitutive equations. If the approximation of the virtual work of the external volume and surface loads $\delta W_{\text{ext}}^{\text{h}}$ is also performed, the following representation for the weak form of the moment balance equation is then obtained:

$$\mathbf{M}_{\mathbf{m}} \dot{\mathbf{v}}^{\text{h}} + \mathbf{f}_{\text{int}}^{\text{h}}(\mathbf{u}^{\text{h}}) = \mathbf{f}^{\text{h}} \tag{3.21}$$

The system of differential equations (3.21) consists of the approximated acceleration vector $\dot{\mathbf{v}}^{\text{h}}$, the mass matrix $\mathbf{M}_{\mathbf{m}}$ and the internal force vector $\mathbf{f}_{\text{int}\,I}^{\text{h}}(\mathbf{u}^{\text{h}})$ in Eq. (3.20) and the external load vector $\mathbf{f}^{\text{h}}$, including boundary conditions. In addition to space, a discretization of Eq. (3.21) must also be performed over time. In static analysis, there is no effect of mass (inertia) or of damping. In dynamic analysis, nodal forces associated with mass/inertia and damping are included. Static analysis is done using an implicit solver in LS-Dyna®. Dynamic analysis can be done via the explicit solver or the implicit solver.

In nonlinear implicit analysis, solution of each step requires a series of trial solutions (iterations) to establish equilibrium within a certain tolerance. In explicit analysis, no iteration is required as the nodal accelerations are solved directly.

The time step in explicit analysis must be minor than the Courant time step (time it takes a sound wave to travel across an element), while the convergence criteria is accomplished. As such, implicit time steps are generally several orders of magnitude larger than explicit time steps.

Implicit analysis requires a numerical solver to invert the stiffness matrix once or even several times over the course of a load/time step. This matrix inversion ensures convergence of

results, but it is an expensive operation, especially for large models. Explicit does not require this step. Thus, since convergence is not checked, the analysis must be performed in small time increments.

Explicit analysis handles nonlinearities with relative ease as compared to implicit analysis. This would include treatment of contact and material nonlinearities.

In explicit dynamic analysis, nodal accelerations are solved directly (not iteratively) as the inverse of the diagonal mass matrix times the net nodal force vector where net nodal force includes contributions from exterior sources (body forces, applied pressure, contact, etc.), element stress, damping, bulk viscosity, and hourglass control. Once accelerations are known at time n, velocities are calculated at time $n + 1/2$, and displacements at time $n + 1$. From displacements, strain is computed. From strain comes stress, and the cycle is subsequently repeated.

Chapter 4

Constitutive Models

The balance equation and its discretization by means of the FEM were discussed in the previous chapter. Different stress-strain relations will occur in bodies with the same geometry and state of stresses, depending on the material descriptions used to characterize them. Thus, material-dependent physical behaviour must be mathematically described by creating constitutive equations, that is to say material models.

The present chapter provides a brief overview of elasto-viscoplasticity formulation of the finite deformation constitutive equations. Subsequently, the basics of fracture and damage mechanics are presented.

4.1. Elasto-viscoplasticity

In elasto-viscoplasticity, in contrast to classical elastoplasticity, material response besides the deformation itself depends on the strain rate. Classical plasticity theory includes the description of the elastic and plastic states by means of a flow condition. The plastic deformation is represented by an increase of the flow rule and the material hardening by additional evolution equations for the hardening variables. Therefore, the description of the fundamentals of plasticity theory is given in this section primarily for infinitesimal strains. The decomposition of the infinitesimal Green-Lagrange strain tensor is performed as follows:

$$\boldsymbol{\varepsilon} = \boldsymbol{\varepsilon}^{\mathrm{el}} + \boldsymbol{\varepsilon}^{\mathrm{pl}} \tag{4.1}$$

As well as,

$$\dot{\boldsymbol{\varepsilon}} = \dot{\boldsymbol{\varepsilon}}^{\mathrm{el}} + \dot{\boldsymbol{\varepsilon}}^{\mathrm{pl}} \tag{4.2}$$

Before plastic strain take place in the material, many materials can be considered purely elastic, as in the case of structural adhesives. In the elastic behaviour a linear, isotropic relationship between the Cauchy stress tensor $\boldsymbol{\sigma}$ and the elastic strain $\boldsymbol{\varepsilon}^{\mathrm{el}}$ is stablished:

$$\boldsymbol{\sigma} = \mathbb{C}[\boldsymbol{\varepsilon}^{\mathrm{el}}] \ , \text{ with } \mathbb{C} := 2G\left(\mathbb{I} - \frac{1}{3}\mathbf{1}\otimes\mathbf{1}\right) + K_{\mathrm{K}}\mathbf{1}\otimes\mathbf{1} \tag{4.3}$$

$\mathbb{C}$ is the fourth-order stiffness tensor entirely determined by the positive elastic constants of shear and compression moduli G and K_{K}. The distinction between the plastic and the elastic range is made by the flow function f. For the three-dimensional case this is a tensor function $f = f(\boldsymbol{\sigma}, \boldsymbol{q})$ (in the following expression) with the arguments Cauchy stress $\boldsymbol{\sigma}$ and inner variables $\boldsymbol{q}$. The flow condition for rate-independent plasticity is:

$$f := \hat{f} - Y_0 = 0 \tag{4.4}$$

and describes a so-called yield surface in the six-dimensional stress space with the scalar flow beginning Y_0 and the tensor function $\hat{f} = \hat{f}(\boldsymbol{\sigma}, \boldsymbol{q})$. Assuming material isotropy, this comparison function $\hat{f}$ depends on the invariants of the stress tensor I_1, I_2, I_3 or its deviators J_2, J_3. The invariants of the stress tensor are defined as:

$$I_1 := \mathrm{sp}\boldsymbol{\sigma} \ , \ I_2 := \frac{1}{2}\left(\mathrm{sp}^2\boldsymbol{\sigma} - \mathrm{sp}\boldsymbol{\sigma}^2\right) \ , \ I_3 := \det\boldsymbol{\sigma} \tag{4.5}$$

Together with the introduction of the deviatoric stress tensor (which deprecates the volumetric strain, taking into account the shape change only),

$$\boldsymbol{\sigma}^{\mathrm{D}} := \boldsymbol{\sigma} - \frac{1}{3}(\mathrm{sp}\boldsymbol{\sigma})\mathbf{1} \tag{4.6}$$

their invariants with the definition of the scalar product of tensors result in:

$$J_2 := \frac{1}{2}\boldsymbol{\sigma}^{\mathrm{D}} \cdot \boldsymbol{\sigma}^{\mathrm{D}} \ , \ J_3 := \det\boldsymbol{\sigma}^{\mathrm{D}} \tag{4.7}$$

The flow rule represents an evolution equation for the plastic strains:

$$\dot{\boldsymbol{\varepsilon}}^{\mathrm{pl}} = \lambda\frac{\partial f^*}{\partial \boldsymbol{\sigma}} = \lambda\mathbf{M} \tag{4.8}$$

The gradient **M** of the plastic potential f^* in Eq. (4.8) describes here the direction of flow and the scalar plastic multiplier $\lambda \geq 0$ the size of the plastic strain increment. An associated flow rule exists for the case $f^* = f$, otherwise one speaks of non-associated plasticity. Apart from the flow rule, the inner variable q and the gradient $\mathbf{h}(\boldsymbol{\sigma}, \boldsymbol{q})$ have to be specified along with its evolution,

$$\dot{\mathbf{q}} := \lambda \mathbf{h}(\boldsymbol{\sigma}, \mathbf{q}) \tag{4.9}$$

for a complete description of the plastic state. The previous equation, unlike the ideal plasticity, allows a phenomenological determination of the nonlinear material properties resulting from experimental data. The inner variables term indicates that the observation of this variable can not be made directly as in strain or temperature. However, various combinations of the invariants of the plastic flow (4.9) and other constants can be formed. The simplest representation of the strain hypothesis is therefore the Euclidean norm of the plastic strain rate (4.8):

$$\dot{\varepsilon}^{\mathrm{v}} := \|\dot{\boldsymbol{\varepsilon}}^{\mathrm{pl}}\| = \sqrt{\boldsymbol{\varepsilon}^{\mathrm{pl}} \cdot \boldsymbol{\varepsilon}^{\mathrm{pl}}} = \lambda \sqrt{\mathbf{M} \cdot \mathbf{M}} \tag{4.10}$$

In the case of the working hypothesis, instead of the norm (4.10) of the plastic strain rates, the plastic strain potential is used:

$$\dot{\varepsilon}^{\mathrm{vA}} := \frac{1}{Y_0} \boldsymbol{\sigma} \cdot \dot{\boldsymbol{\varepsilon}}^{\mathrm{pl}} = \frac{\lambda}{Y_0} \boldsymbol{\sigma} \cdot \mathbf{M} \tag{4.11}$$

Plastic deformations occur when the flow condition $f = 0$ in Eq. (4.4) is fulfilled. In non-ideal plastic material models, a hardening due to plastic deformation appears and there is a change in the flow area f of the space of stresses. This state is achieved by plastic flow with the flow rule (4.8) and $\lambda > 0$, so that the flow condition $f = 0$ and their temporal derivative $\dot{f} = 0$ must always be met. The temporal evolution of the flow condition $\dot{f} = 0$ is also called a consistency condition, which allows the determination of the plastic multiplier λ. For this, the complete time derivative of the flow condition (4.4) is formed and set to zero:

$$\dot{f} = \frac{\partial f}{\partial \boldsymbol{\sigma}} \cdot \dot{\boldsymbol{\sigma}} + \frac{\partial f}{\partial \mathbf{q}} \cdot \dot{\mathbf{q}} = 0 \tag{4.12}$$

Substituting the rate form ($\boldsymbol{\sigma} = \mathbb{C}[\dot{\varepsilon}^{\mathrm{el}}]$) of the stress-strain relation (4.3) with the elastic strain rate $\dot{\varepsilon}^{\mathrm{el}} = \varepsilon - \dot{\varepsilon}^{\mathrm{pl}}$ according to Eq. (4.2), the flow rule (4.8), the development equation (4.9), the inner variable q and the gradient of the flow function:

$$\mathbf{N} := \frac{\partial f}{\partial \boldsymbol{\sigma}} \tag{4.13}$$

in the consistency condition (4.12) leads to the plastic multiplier:

$$\lambda = \frac{\mathbf{N} \cdot \mathbb{C}[\dot{\boldsymbol{\varepsilon}}]}{\mathbf{N} \cdot \mathbb{C}[\mathbf{M}] - \frac{\partial f}{\partial \mathbf{q}} \cdot \mathbf{h}} \tag{4.14}$$

Back-substitution into the rate form of the equation (4.3) using the flow rule (4.8) and the decomposition of the infinitesimal Green-Lagrange strain tensor (4.1) yields the incremental stress-strain ratio (tangential stiffness ratio),

$$\dot{\boldsymbol{\sigma}} = \left[\mathbb{C} - \frac{\mathbb{C}(\mathbf{M} \otimes \mathbf{N})\mathbb{C}}{\mathbf{N} \cdot \mathbb{C}[\mathbf{M}] - \frac{\partial f}{\partial \mathbf{q}} \cdot \mathbf{h}} \right] [\dot{\boldsymbol{\varepsilon}}] = \mathbb{C}^{\mathrm{ep}}[\dot{\boldsymbol{\varepsilon}}] \tag{4.15}$$

with the elastoplastic tangent modulus $\mathbb{C}^{\mathrm{ep}}$. Table 1 shows the four possible cases for loading and unloading conditions, which result from the flow and consistency condition in equations (4.4) and (4.12).

In literature, different approaches for flow functions can be found. A characteristic for the classification of the approaches is the hardening behaviour. A distinction is made between flow functions with isotropic, kinematic and formative hardening. In isotropic hardening, the flow area widens equally:

$$f_1 = f_1(\boldsymbol{\sigma}, q) = \hat{f}_1(\boldsymbol{\sigma}) - Y_0 - R(q) \text{ with evolution equation for } q \tag{4.16}$$

The isotropic hardening can be described by a scalar inner variable q with the hardening stress $R(q)$. In the case of a translational displacement of the flow surface in the stress space while maintaining its shape, one speaks of a kinematic hardening:

$$f_2 = f_2(\boldsymbol{\sigma}, \mathbf{q}) = \hat{f}_2(\boldsymbol{\sigma} - \mathbf{q}) - Y_0 \text{ with evolution equation for } \mathbf{q} \tag{4.17}$$

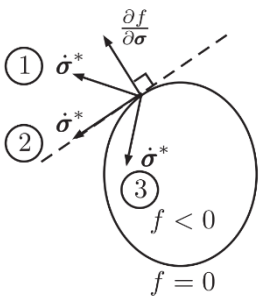

State	Flow and consistency condition
① Plastic loading	$f = 0 \wedge \dot{f} = 0 \rightarrow \lambda > 0$
② Neutral loading	$f = 0 \wedge \dot{f} = 0 \rightarrow \lambda = 0$
③ Elastic unloading	$f = 0 \wedge \dot{f} < 0 \rightarrow \lambda = 0$
Elastic loading	$f < 0 \wedge \dot{f} < 0 \rightarrow \lambda = 0$

Table 1: loading and unloading conditions of the flow function for rate-independent plasticity

The displacement of the flow surface is controlled by a second-order stress tensor **q**. The third variant is the formative hardening:

$$f_3 = f_3(\boldsymbol{\sigma}, \mathbf{q}) = \hat{f}_3(\boldsymbol{\sigma}, \mathbf{q}) - Y_0 \text{ with evolution equation for } \mathbf{q} \tag{4.18}$$

where the flow surface in the stress space rotates or changes its shape. A combination of both types of hardening is also possible. The material equations presented here apply only to rate-independent plasticity.

The rate-dependent material formulation not only takes into account the plasticity but also the viscous, time-dependent material properties. This fact is illustrated through the rheological model called Bingham body as shown in Figure 4.1. It consists in the parallel connection of a plastic friction element (characterized by a yield stress Y_0) and a damper element with viscosity μ^{vc}. To describe the elastic range, a linear-elastic spring with elasticity modulus E is arranged in series with the parallel connection.

From this simple rheological model, basic properties of viscoplasticity can be derived. The elastic strains $\boldsymbol{\varepsilon}^{\mathrm{el}}$ are further decoupled from the viscoplastic strains $\boldsymbol{\varepsilon}^{\mathrm{vp}}$ and additively give the total strains $\boldsymbol{\varepsilon}$ as in Eq. (4.1). Rate-dependent plastic flow effects start taking place when the applied stress exceeds the yield stress: $|\sigma| \geq Y_0$. At the junction of the parallel connection, a stress balance occurs between the stress in the elastic spring ($\sigma = \mathrm{E}\,\varepsilon^{\mathrm{el}}$) and the viscous stress in the damper ($\sigma^{\mathrm{vc}} := \eta^{\mathrm{vc}}\,\dot{\varepsilon}^{\mathrm{vc}}$):

$$|\sigma| = Y_0 + \eta^{\mathrm{vc}}|\dot{\varepsilon}^{\mathrm{vp}}| \;\rightarrow\; f := |\sigma| - Y_0 = |\sigma^{\mathrm{vc}}| \tag{4.19}$$

The previous equation leads directly to the definition of the flow function f for the one-dimensional rheological model. The viscoplastic material behaviour when $\eta^{\mathrm{vc}} \rightarrow 0$ recovers the rate-independent formulation $f = 0$, otherwise the flow condition assumes states greater than zero as a function of the viscoplastic strain rate $f = |\sigma_{\mathrm{vc}}| > 0$. Taking this into consideration, the stress balance (4.19) together with the definition of the Macauley bracket $\langle x \rangle := \frac{1}{2}(x + |x|)$ for observing viscoplastic flow satisfying the flow condition $f \geq 0$ also provides the evolution equation for inelastic strains:

$$|\dot{\varepsilon}^{\mathrm{vp}}| = \mu^{\mathrm{vc}} \langle |\sigma| - Y_0 \rangle = \mu^{\mathrm{vc}} \langle f \rangle = \mu^{\mathrm{vc}} |\sigma^{\mathrm{vc}}| = \lambda \tag{4.20}$$

(with the fluidity $\mu^{\mathrm{vc}} = 1/\eta^{\mathrm{vc}}$ [1/(MPa·s)], the reciprocal of viscosity η^{vc}).

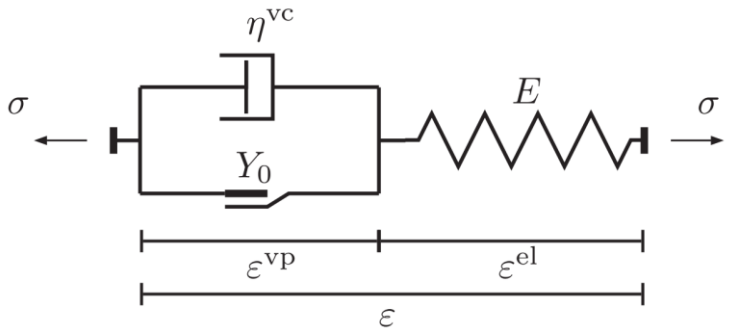

Figure 4.1: Rheological model of ideal elasto-viscoplasticity (Burbulla F. , Kontinuumsmechanische und bruchmechanische Modelle für Werkstoffverbunde, 2015)

The three-dimensional generalization of the approach involves the identification of the plastic multiplier in the three-dimensional case of the flow rule (4.8) with the one-dimensional case of Eq. (4.20):

$$\lambda := \mu^{\mathrm{vc}} Y_0 \Phi_{\mathrm{P}}\left(\frac{\langle f \rangle}{Y_0}\right) = \mu_0^{\mathrm{vc}} \Phi_{\mathrm{P}}(\langle f_0 \rangle) \ , \ \text{with} \ \langle f_0 \rangle = \frac{\langle f \rangle}{Y_0} \tag{4.21}$$

Here, $\mu_0^{\mathrm{vc}} := \mu^{\mathrm{vc}} Y_0$ [s^{-1}] is a normalized material parameter and Φ_{P} ($\langle f_0 \rangle$) is a dimensionless function depending on the flow function f. The flow rule (4.8) for the viscoplastic case is:

$$\dot{\boldsymbol{\varepsilon}}^{\mathrm{vp}} = \mu_0^{\mathrm{vc}} \Phi_{\mathrm{P}}(\langle f_0 \rangle) \frac{\partial f^*}{\partial \boldsymbol{\sigma}} \tag{4.22}$$

The dimensionless function Φ_{P} ($\langle f_0 \rangle$) can be specifically identified by means of experimental data. There are two main suggested approaches, a exponential approach:

$$\Phi_{\mathrm{P1}}(\langle f_0 \rangle) := \exp\left(\frac{\langle f \rangle}{Y_0}\right) - 1 \ \rightarrow \ |\sigma^{\mathrm{vc}}| = Y_0 \ln\left(\frac{|\dot{\varepsilon}^{\mathrm{vp}}|}{\mu_0^{\mathrm{vc}}} + 1\right) \tag{4.23}$$

and a potential approach:

$$\Phi_{\mathrm{P2}}(\langle f_0 \rangle) := \left(\frac{\langle f \rangle}{Y_0}\right)^n \ \rightarrow \ |\sigma^{\mathrm{vc}}| = Y_0 \sqrt[n]{\frac{|\dot{\varepsilon}^{\mathrm{vp}}|}{\mu_0^{\mathrm{vc}}}} \tag{4.24}$$

where the respective stresses follow the already exposed equations (4.20) and (4.21).

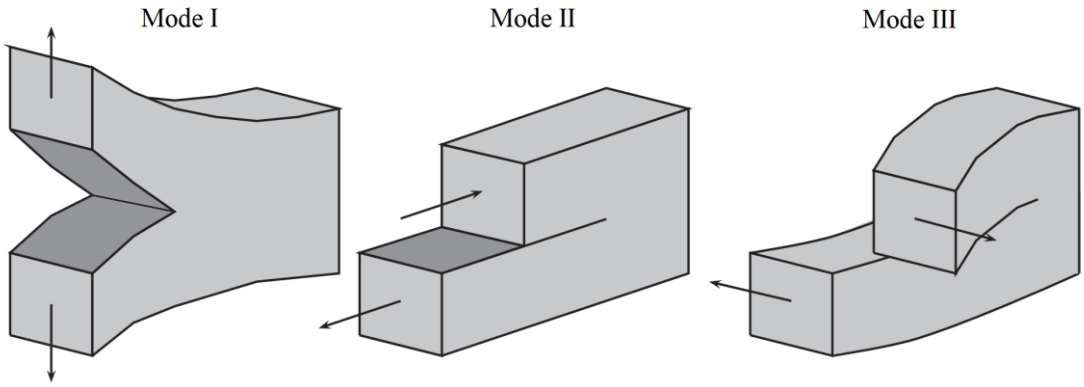

Figure 4.2: Fracture modes (Burbulla F. , Kontinuumsmechanische und bruchmechanische Modelle für Werkstoffverbunde, 2015)

The proposal of a rate- and temperature-dependent material model from Johnson and Cook is based on the static yield stress increase $Y_0 + R(q)$ of the isotropic hardening approach (4.16) using the total strain rate for the isothermal case $\dot{\varepsilon}$:

$$\hat{f} = [Y_0 + R(q)]\,(1 + C\langle \ln \dot{\varepsilon}^* \rangle) \;, \text{ with } \dot{\varepsilon}^* := \frac{\dot{\varepsilon}}{\dot{\varepsilon}_0} \tag{4.25}$$

The reference strain rate $\dot{\varepsilon}_0$ determines the transition from the quasi-static to strain rate-dependent yield stress, and C is a positive material parameter. This flow condition (4.25) is also an stress-based model, which can be formally expressed as in Eq. (4.23):

$$\begin{aligned} f - |\sigma^{\text{vc}}| = 0 = \hat{f} - [Y_0 + R(q)]\,(1 + C\langle \ln \dot{\varepsilon}^* \rangle) \;\rightarrow \\ \rightarrow\; |\sigma^{\text{vc}}| := [Y_0 + R(q)]\, C\langle \ln \dot{\varepsilon}^* \rangle \end{aligned} \tag{4.26}$$

The presented models will be equivalent if their viscous stresses σ_{vc} are the same. In contrast to classical plasticity, in the theory of viscosity the real time has to be taken into account. The time-independent mechanisms continue to cause the same plastic deformations in the material for $\sigma_{\text{vc}} = 0$.

4.2. Fundamentals of Fracture and Damage Mechanics

The classical considerations in Continuum Mechanics do not consider the formation of cracks and the creation of new surfaces in a body mass. Cracked bodies, on the other hand, are in the scope of the investigations in Fracture Mechanics. Continuum Damage Mechanics (CDM) is the link between these two disciplines and detects the formation of a macroscopic crack due to the formation and growth of microdefects and pores in a body. The description of these microdefects occurs in the

CDM at the macroscopic level through the definition of a loss of strength (degradation) of the material.

4.2.1. Energy release rate in Fracture Mechanics

The energy release $\mathcal{G}$ is the released energy at crack formation in relation to the newly created fracture surface. The Griffith theory of brittle fracture presupposes an elastic material behaviour of the body where the stored internal energy in the material is released, due to formation of new surfaces because of crack onset/propagation. Crack propagation occurs according to the energetic fracture criterion if the energy release $\mathcal{G}$ for a process corresponds to $\mathcal{G}_c$, commonly know as *Fracture toughness*. The critical energy release $\mathcal{G}_c$ is a material parameter that can be determined from experiments with controlled crack growth. The energy release rate $\mathcal{G}$ can be divided into three separate fracture modes, shown schematically in Figure 4.2.

$$\mathcal{G} := \mathcal{G}_{\mathrm{I}} + \mathcal{G}_{\mathrm{II}} + \mathcal{G}_{\mathrm{III}} \tag{4.27}$$

One tensile and two shear-related modes of propagation can be distinguished. Mode I corresponds to the traction mode. The shear stress mode II acts vertically and mode III acts parallel to the crack front. Explicit distinction between Mode II and III is extremely difficult from a practical point of view and it is usually not accessible experimentally. Therefore, the description of the shear mode is commonly simplified, considering exclusively the energy $\mathcal{G}_{\mathrm{T}}$:

$$\mathcal{G}_{\mathrm{T}} := \mathcal{G}_{\mathrm{II}} + \mathcal{G}_{\mathrm{III}} \tag{4.28}$$

In the following, a new variable $\mathcal{G}_{\mathrm{N}}$ will be introduced for Mode I:

$$\mathcal{G}_{\mathrm{N}} := \mathcal{G}_{\mathrm{I}} \tag{4.29}$$

Therefore, the energy release subscript N stands for the normal direction on the fracture surface, such as the subscript T in the previous expression indicates the tangential plane of the fracture surface.

4.2.2. Degradation models of Continuum Damage Mechanics

The ductile damage due to microcracks and cavitation occurs along with the plastic deformation of the body. Microcracking and pore formation takes place throughout the entire continuum; even in the initial state the body is provided with defects. Within the scope of CDM, the micro-stresses are averaged over a so-called representative volume element (RVE). The size of the

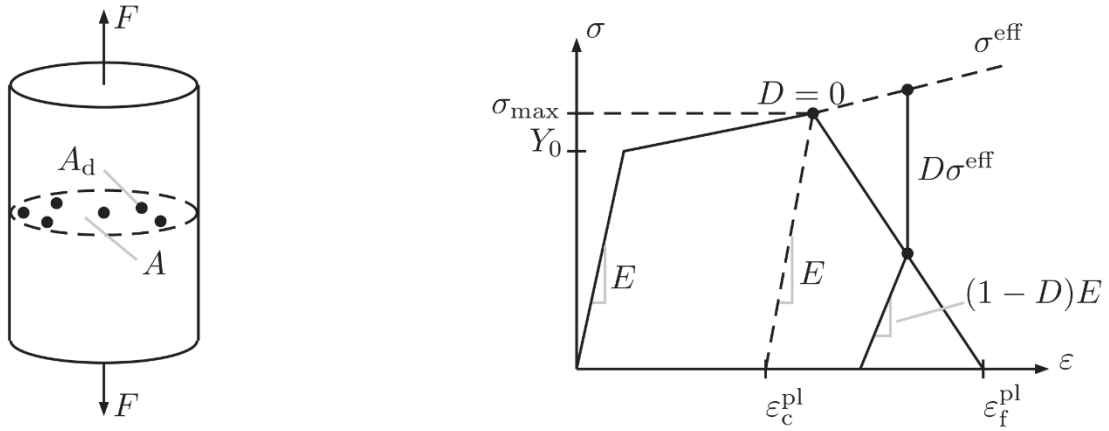

Figure 4.3: Left: Schematic representation of a body with cracks and pores; Right: Stress-strain curve under damage evolution (Burbulla, Matzenmiller, & Kroll, 2015)

RVE for imaging damage effects - depending on the size of the damage defects - amounts to approx. 1mm^3 for polymers and can certainly be transferred to the structural adhesives.

The undamaged surface is defined by A, A_d is the defect surface with cracks and pores – shown in Figure 4.3 (left). The growth of microcracks and pores in the control volume is expressed by a scalar damage variable. A damage approach using continuity $\Psi_\text{d} \coloneqq (A - A_\text{d})/A$ with $0 \leq \Psi_\text{d} \leq 1$ is presented, interpreting microcracking as a macroscopic loss of stiffness (degradation). Instead of continuity, a damage variable D can be defined as the ratio of defect area A_d to starting area A for isotropic damage models:

$$D \coloneqq \frac{A_\text{d}}{A}\ ,\ 0 \leqslant D \leqslant 1 \tag{4.30}$$

The damage value D develops from the value 0 in the undamaged state to the value 1 in the case of complete local damage of the material. At the onset of plastic deformation, the rate of damage to most engineering materials is low. Only after exceeding the limit $\varepsilon_\text{c}^\text{pl}$ – see Figure 4.3 right – the damage due to microcracks and micropores increases significantly. The macro-breaking sets for $D = 1$ at $\varepsilon_\text{f}^\text{pl}$.

The concept of effective stress σ^eff relates the applied force F to the undamaged surface $(A - A_\text{d})$ with cracks and pores:

$$\sigma^\text{eff} = \frac{F}{A - A_\text{d}} = \frac{F}{A(1-D)} = \frac{\sigma}{1-D} \tag{4.31}$$

The force F and the undamaged cross-sectional area $(A - A_{\mathrm{d}})$ can be eliminated for the one-dimensional case in the previous expression using the nominal stress $\sigma = F/A$, so that the nominal stresses can be converted directly into the effective ones. The assumptions can generally be applied in connection with isotropic damage (4.31) and the continuity Ψ_{d} for the spatial stress state, resulting into:

$$\boldsymbol{\sigma}^{\mathrm{eff}} := \frac{\boldsymbol{\sigma}}{1 - D} = \frac{\boldsymbol{\sigma}}{\Psi_{\mathrm{d}}} \tag{4.32}$$

The nominal stresses σ in the flow condition (4.4), in the flow rule (4.8) and in the plastic potential f^* are replaced by the effective stress (4.32) for the case of material damage. At the same time, the effective stress steadily increases in contrast to the nominal stress. Besides, the elastic stiffness $(1 - D)E$ undergoes a degradation process due to the development of damage D – shown in Figure 4.3 right.

Chapter 5

Material Model Description

In this chapter a general description of the structure of ductile modified structural adhesives is presented. The different flow criteria used in order to map their yield envelope are introduced as well. This chapter also describes in detail the formulation of an elasto-viscoplastic material model with damage, compiled as material type 252 *MAT_TOUGHENED_ADHESIVE_POLYMER in the commercial software LS-Dyna®, and the different parameters that form its material card. This material formulation will be used further on in the FEM models of tests specimens and components created to show its performance and capabilities.

5.1. Ductile modified structural adhesives

Thermosetting structural adhesives usually consist of an epoxy polymer matrix. Through a specific selection of the polymer system, the mechanical properties can be directly influenced, like the energy absorption capacity under impact. In that sense, there is a kind of matrix additives called flexibilizers (tougheners). The flexibilizer primarily changes the damage and fracture behaviour at almost constant maximum achievable load levels. Thus, there is a continuous softening and no sudden failure; one speaks then of ductile modified structural adhesives.

An external load of the structural adhesive leads to the formation of cavities in the matrix material and their integration into microcracks. The epoxy polymer matrix is deformed and local areas with large deformations appear, which leads to different modes of cracking. The crack tip can move around a rubber particle and detach it from the matrix composite – see Figure 5.1. On the other hand, there is a delay in the continuous crack propagation through branching on individual particles of the flexibilizer. The third form of damage is the formation of cavitation due to a separation of the rubber part. The dissipated energy used to break the flexibilizer is significantly higher in this process than in non-ductile modified adhesives.

In addition to the chemical composition and the microscopic structure of the adhesive, further knowledge in the field of mechanical properties is of great importance. The phenomenological

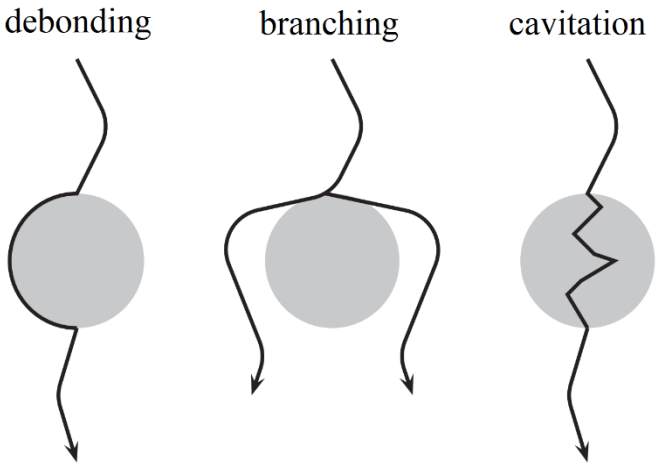

Figure 5.1: Schematic representation of crack formation in an adhesive system (Symietz and Lutz, 2006)

description of the mechanical material behaviour can be derived in principle from experimental observations. A pronounced elastoplastic material behaviour is shown in the shear stress-strain diagram in the left of Figure 5.2 for loading and unloading tests. It can be checked that a moderate loading and unloading cycle causes permanent deformations. For low stress levels, the process is virtually reversible and can be considered approximately linear elastic. The unusually clear demarcation of the elastic and plastic ranges for structural adhesives allows the use of flow surface models. As the velocity of the experiment increases, the adhesive shows an increase in the yield stress in the shear stress-strain diagram, qualitatively shown in the right-hand Figure 5.2. Therefore, elasto-viscoplastic material behaviour can be assumed.

5.2. State-of-the-Art in the modelling of ductile modified adhesives

As already mentioned, modified structural adhesives show an elasto-viscoplastic material behaviour. In the following, some basic flow criteria with the corresponding definitions from chapter 4 are presented. The Von Mises flow criterion for metallic materials – which are approximately plastically incompressible – leads to a sufficiently accurate mapping of the experimentally determined starting of flow Y_{M} for varying loads, and considers only the second invariant J_2 according to Eq. (4.7) of the stress deviator Eq. (4.6):

$$f_M := \sqrt{3J_2} - Y_{\mathrm{M}} = 0 \tag{5.1}$$

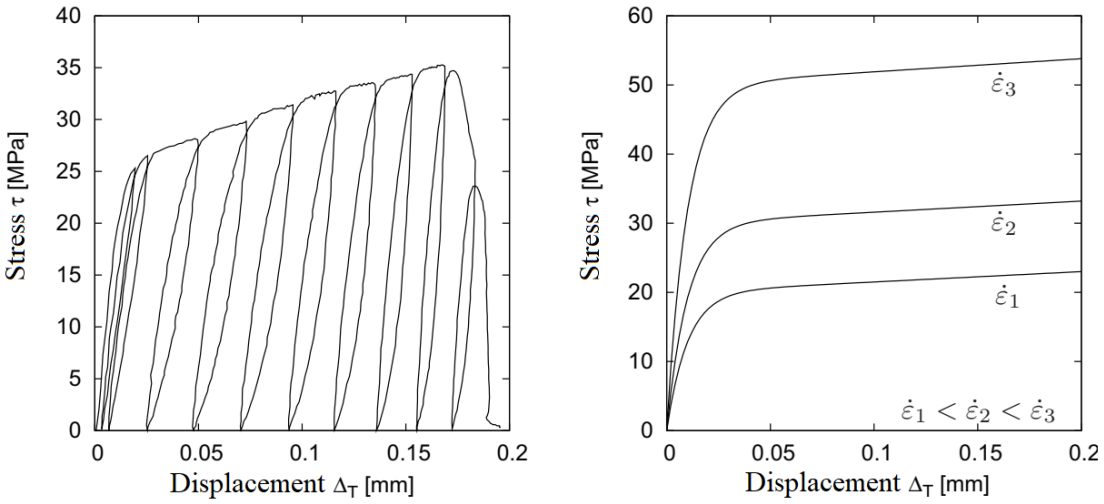

Figure 5.2: Left: Shear stress vs displacement curve of a cyclic loading and unloading test on a bonded double tube sample (Schlimmer et al., 2008, FOSTA-P676, Figure 22); Right: Qualitative representation of the rate dependency of yield stress

The value Y_M in Eq. (5.1) is determined from uniaxial tensile tests and the corresponding $Y_M/\sqrt{3}$ yield point lies on the $\sqrt{J_2}$ axis in Figure 5.3. In general, the first term in Eq. (5.1) is referred to as von Mises-equivalent stress σ_{eq}, which maps the three-dimensional stress state to a one-dimensional comparison state:

$$\sigma_{eq} := \sqrt{3J_2} \tag{5.2}$$

By contrast, polymeric engineering materials and adhesive systems are characterized by plastic compressibility. The material not only deforms but also undergoes dilatation due to micro-pores and cavitation under hydrostatic stress $\sigma_{eq} := I_1/3$. σ_m is the average of the normal stresses expressed by means of the first invariant I_1 of the stress tensor exposed in Eq. (4.5)

The influence of hydrostatic stress can be introduced by using the linear flow condition of Drucker & Prager,

$$f_{DP} := \sqrt{J_2} + a_{DP} I_1 - Y_{DP} = 0 \tag{5.3}$$

which was originally developed for frictional and geological materials. The von Mises flow condition (5.11) with the deviatoric stress tensor is independent of the hydrostatic stress and thus

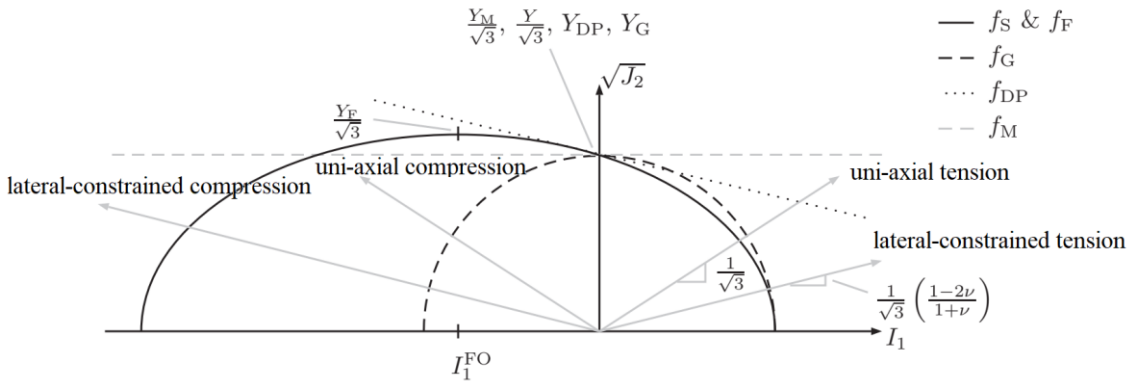

Figure 5.3: Comparison of flow conditions: SCHLIMMER f_S, FLECK f_F, GREEN f_G, DRUCKER&PRAGER f_{DP}, and VON MISES f_M. (Burbulla F. , Kontinuumsmechanische und bruchmechanische Modelle für Werkstoffverbunde, 2015)

appears in the I_1-$\sqrt{J_2}$ diagram in Figure 5.3 as a horizontal line. In contrast, the Drucker & Prager criterion in Eq. (5.3) is a straight line with the slope factor a_{DP} and the yield point Y_{DP}.

Fleck model uses a description for ductile modified adhesives which additionally shifts the quadratic flow function f_F with a constant a_F and the yield stress Y_F along the hydrostatic axis by the amount I_1^{FO}:

$$f_F := \sqrt{3J_2 + \frac{a_F^2}{9}(I_1 - I_1^{FO})^2} - Y_F = 0 \tag{5.4}$$

The $Y_F/\sqrt{3}$ yield point is not on the $\sqrt{J_2}$ axis as in previous equations (5.1) and (5.3), but lies at the apex of I_1^{FO} – see Figure 5.3. As a result, no experiment can be used as direct identification method. Therefore, at least three experiments are needed to set an elliptic compensation curve through the corresponding pour points of the individual experiments. The beginning of the elliptic flow condition with $I_1^{FO} = 0$ is the Green model for porous materials with a density-dependent function for the parameter value a_G:

$$f_G := \sqrt{J_2 + \frac{a_G}{3} I_1^2} - Y_G = 0 \tag{5.5}$$

For the flow condition (5.5) two tests are sufficient for the parameter identification; a test with deviatoric stress for the determination of Y_G and a tension or compression test for the determination of the parameter a_G. A flow criterion specifically presented for adhesive systems is based on the work of Schlimmer,

$$f_S := J_2 + \frac{1}{3} a_1 Y_0 I_1 + \frac{1}{3} a_2 I_1^2 - \frac{1}{3} Y^2 = 0 \tag{5.6}$$

which in addition to the yield stress $Y := Y_0 + R$ with the initial yield stress Y_0 and the hardening stress R, has two further material constants a_1 and a_2. As in the case of the flow condition (5.4), at least three experiments are required for the identification of the parameters, whereby the yield point $Y_0/\sqrt{3}$ lies on the $\sqrt{J_2}$ axis in Figure 5.3.

The flow conditions (5.4) and (5.6) are equivalent, although they have been developed for different materials. The form (5.6) and the vertex form (5.4) can be compared through the relations

$$Y_F^2 = Y^2 + \frac{a_1^2 Y_0^2}{4 a_2} \;,\; a_F = \sqrt{9 a_2} \;,\; I_1^{FO} = - \frac{a_1 Y_0}{2 a_2} \tag{5.7}$$

between the corresponding coefficients as shown in Figure 5.3.

In addition to the presented flow criteria, plastic potentials are also needed for the description of the plastic flow (4.8) for friction and porous materials. Since, in contrast to the metallic materials, the flow functions for adhesive systems depend on the hydrostatic stress, the use of associated flow rules leads to an overestimation of the plastic dilatation. The plastic flow vector is only normal to the yield surface if there are no pores in the material. Instead, the development of the plastic strain increment is described phenomenologically with the non-associated flow rule if the material is additionally provided with cavities. The experimentally measured volume changes of the material under plastic deformation can be detected with sufficient accuracy by the use of the non-associated flow rule.

5.3. Viscoplasticity model with stress-dependent yield criterion

This model is based on the strain-rate-dependent yield stress $Y = Y(r, \dot{\gamma})$ with the hardening variable r, the strain rate $\dot{\gamma}$ and the isotropic material damage variable D expanded in the pressure range by the Mises or Drucker & Prager Flow.

5.3.1. Flow conditions

The thus developed flow criterion (5.6) is used in the vertex:

$$f_{MS} := \frac{J_2}{(1-D)^2} + \frac{a_2}{3} \left\langle \frac{I_1}{1-D} + \frac{a_1 Y_0}{2 a_2} \right\rangle^2 - \frac{1}{3} \left(Y^2 + \frac{a_1^2 Y_0^2}{4 a_2} \right) = 0 \tag{5.8}$$

The coefficients a_1 and a_2 are constant parameters which must be determined from experimental data, as well as the flow threshold Y_0. The basic procedure regarding the parameter identification has been briefly explained in the context of the introduction of the flow condition (5.6). According to section 4.2.2, the stresses in the flow condition are replaced by the effective stresses (4.31) to account for the isotropic damage D. On the other hand, the hardening behaviour is described by a non-linear yield stress Y, wherein the hardening characteristic of the adhesive takes place as a function of the scalar inner variable r. The detailed description of yield stress Y is given in the course of the definition of the shear-based plastic arc length $\gamma_v = \sqrt{2}\varepsilon_v$ in Eq. (5.18) and the hardening variable r in Eq. (5.19) instead of the tensile-based arc length ε_v in Eq. (4.10).

The flow onset Y_M is a material parameter that can be determined directly from the uniaxial tensile test only in the case of the Mises flow condition (5.1). For the hydrostatic stress-dependent criterion (5.8), the flow starting Y_0 for a tensile load ($J_2 \neq 0$, $I_1 \neq 0$ and $I_2 \neq 0$) is no longer independent of the other parameters a_1 and a_2. For this reason, the flow initiation $\tau_0 := Y_0/\sqrt{3}$ is defined for shear loads ($J_2 \neq 0$, $I_1 \neq 0$) instead of Y_0. The material parameter τ_0 is therefore physically interpretable and can be determined directly from tests with deviatoric stresses. The flow condition (5.8) then takes the following form including the shear yield stress $\tau_Y := Y/\sqrt{3}$:

$$f_{MS} := \frac{J_2}{(1-D)^2} + \frac{a_2}{3}\left\langle \frac{I_1}{1-D} + \frac{\sqrt{3}\,a_1\tau_0}{2a_2} \right\rangle^2 - \frac{1}{3}\left(\tau_Y^2 + \frac{a_1^2\tau_0^2}{4a_2}\right) = 0 \tag{5.9}$$

Enclosing the hydrostatic portion with the Macauley bracket causes the pressure range from the vertex of the quadratic function to transition to the constant von Mises flow function (5.1) as shown in Figure 5.4. The structural adhesive shows a deviatoric material behaviour from a certain pressure load $I_1 < I_1^0$ – pure shape change at constant volume – under which the pores and cavities in the adhesive are closed:

$$I_1^0 = -\,(1-D)\,\frac{\sqrt{3}\,a_1\tau_0}{2a_2} \tag{5.10}$$

In principle, tensile torsion tests are sufficient for the identification of the parameters of the flow condition (5.9). The plasticity model with Eq. (5.9) has a low shear strength in the pressure range due to the von Mises criterion, so that a conservative interpretation of the adhesive bond under pressure takes place with this approach.

In the pressure range, the additional friction between the particles within the adhesive, in addition to the closure of the pores and cavities, leads to an increase in the transmissible shear stress. This effect in the pressure range can be described by the Drucker & Prager flow condition (5.3). For

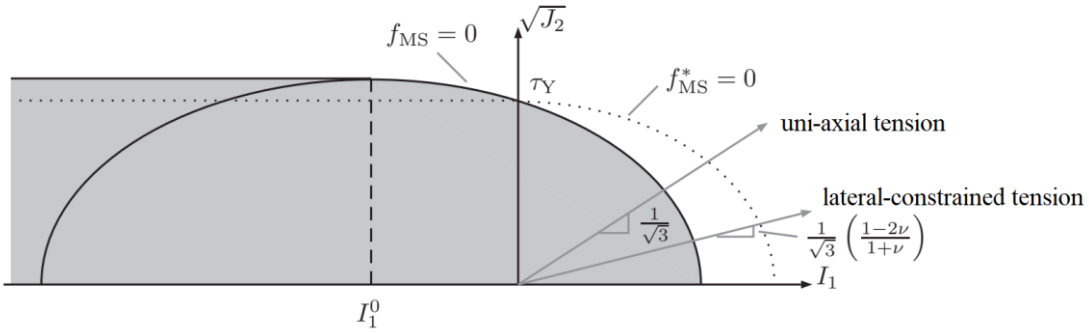

Figure 5.4: Flow function (5.9) according to VON MISES for the pressure range and SCHLIMMER for the tension range. (Burbulla, Matzenmiller, & Kroll, 2015)

this reason, it is useful to formulate the flow condition with the Drucker & Prager approach for the pressure range in addition to the flow condition (5.9) – see Figure 5.5:

$$f_{\mathrm{DPS}} := \frac{J_2}{(1-D)^2} + \frac{1}{\sqrt{3}} a_1 \tau_0 \frac{I_1}{1-D} + \frac{a_2}{3} \left\langle \frac{I_1}{1-D} \right\rangle^2 - \tau_{\mathrm{Y}}^2 = 0 \tag{5.11}$$

Note for $f_{\mathrm{DPS}} = 0$ in Eq. (5.11) the following restriction regarding material parameter identification: when using the flow criterion (5.11), tensile-torsion and compression-torsion tests are indispensable to ensure a clear identification of material consolidation under pressure. Ignorance of the experimental pressure hardening of the adhesive in conjunction with the flow condition (5.11) can otherwise lead to a misinterpretation of the parameter a_1; non-physical high compressive stresses as well as shear stresses are the result.

5.3.2. Plastic potential

For the reasons mentioned in Sections 5.1 and 5.2, the plastic potential becomes

$$f^*_{\mathrm{MS}} := \frac{J_2}{(1-D)^2} + \frac{a_2^*}{3} \left\langle \frac{I_1}{1-D} \right\rangle^2 - \tau_{\mathrm{Y}}^2 \tag{5.12}$$

for determining the non-associated flow rule (4.8) that introduces

$$\dot{\boldsymbol{\varepsilon}}^{\mathrm{pl}} = \lambda \frac{\partial f^*_{\mathrm{MS}}}{\partial \boldsymbol{\sigma}} = \frac{\lambda}{(1-D)^2} \left(\boldsymbol{\sigma}^{\mathrm{D}} + \frac{2}{3} a_2^* \langle I_1 \rangle \mathbf{1} \right) \tag{5.13}$$

as a function of the deviatoric and hydrostatic stresses σ_{D} and $\langle I_1 \rangle \mathbf{1}$. The resulting plastic dilatation can be compensated in the case of a tensile load with the additional material parameter a_2^*. Under pressure, the flow rule is purely shape-changing and thus equivalent to the associated plastic

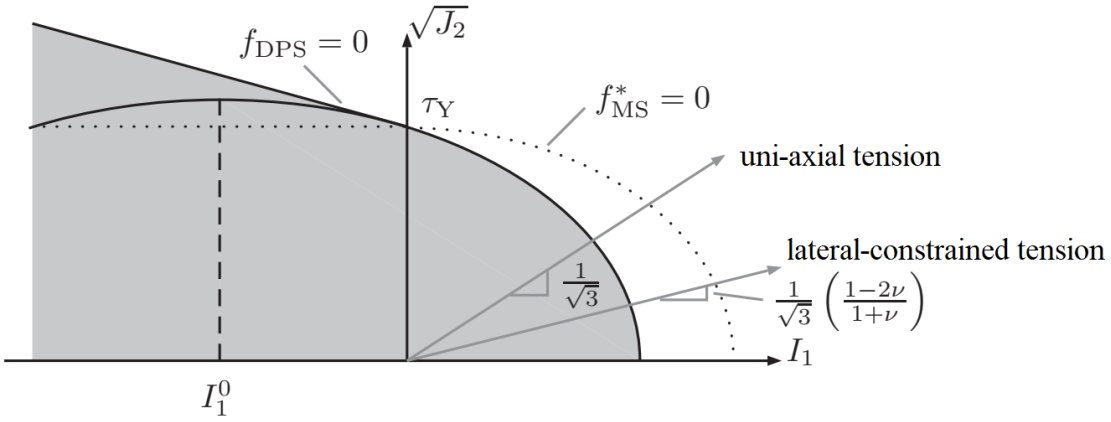

Figure 5.5: Flow function (5.11) according to DRUCKER&PRAGER for the pressure range and SCHLIMMER for the tension range. (Burbulla, Matzenmiller, & Kroll, 2015)

flow of the von Mises criterion (5.1). The plastic volume expansion represents a density change due to cavitation for plastic damaging materials and this can be detected in the plastic potential considering an additional term, which in turn is a function of the hydrostatic stress. The hydrostatic component with the material parameter a_2^* in the plastic potential (5.12) describes all dissipative phenomena in the material, which are caused by the effect of hydrostatic stress. These are, for instance, the volume change due to pure plastic deformation and the formation of cavities by micro-cracking and the plasticization in the environment of the micro-crack.

An estimate of the plastic volume change and thus, the restriction of the value range of a_2^* in Eq. (5.13) can be obtained by evaluating the axial and transverse strain in the stress-strain diagram of the uniaxial tensile test with substance samples in Figure 5.6. The Poisson's ratio υ^* from uniaxial tensile tests is a measure for determining the influence of the plastic volume expansion and is defined by the ratio of the plastic flow in the axial and transverse directions $\varepsilon^{\mathrm{pl}}_{\mathrm{axial}}$ and $\varepsilon^{\mathrm{pl}}_{\mathrm{trans}}$ respectively:

$$\nu^* := -\frac{\dot{\varepsilon}^{\mathrm{pl}}_{\mathrm{trans}}}{\dot{\varepsilon}^{\mathrm{pl}}_{\mathrm{axial}}} \tag{5.14}$$

The introduction of the stress state for the uniaxial tensile test into the components of the plastic flow rule (5.13), using Eq. (5.14) for an explicit expression for the determination of the material parameter a_2^* as a function of the Poisson's ratio υ^* from the experiment:

$$a_2^* = \frac{1-2\nu^*}{2(1+\nu^*)} \tag{5.15}$$

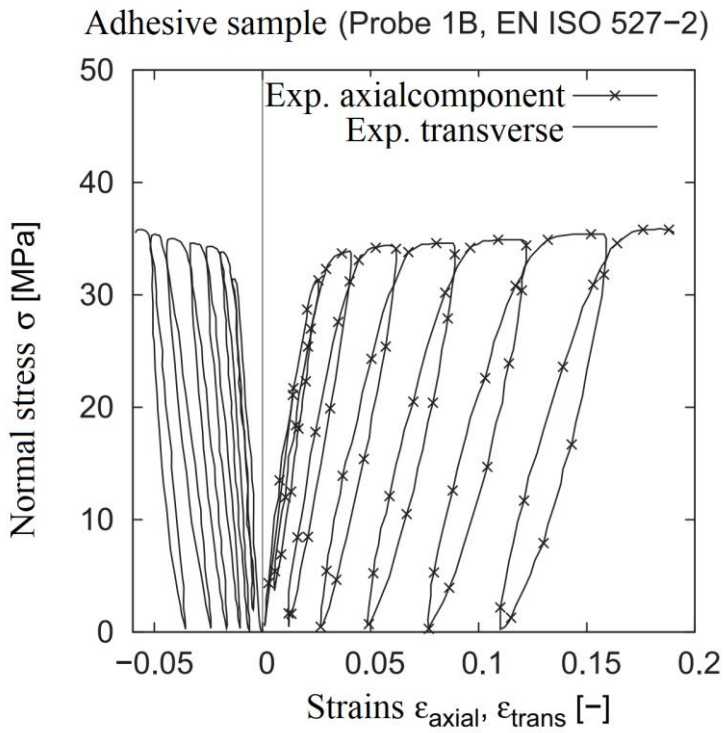

Figure 5.6: Axial and transverse strain measurement on a uniaxially loaded adhesive substance sample (Schlimmer et al., 2002, FOSTA-P593, Figure 6-22)

The Poisson's ratio υ^* in equations (5.14) and (5.15) is evaluated in the stress-strain diagram in Figure 5.6 in the cusp from strain to strain.

5.3.3. Free energy function

The free specific Helmholtz energy function Ψ is used for the purely isothermal mechanical processes considered here to formulate the energetically conjugated quantities (stresses σ, hardening stress R and energy release y) to the corresponding state variables. The energy function Ψ forms the basis for the examination of the dissipation D, so that the developed material model meets the requirements of the second law of thermodynamics for mechanical processes, since irreversible processes such as plastic deformation or damage are always associated with an entropy production. The specific free energy Ψ describes as a state function with the independent state variables (elastic strain tensor, damage variable D and hardening variable r), the elastic material behaviour including damage, as well as the inelastic hardening:

$$\psi = \psi(\boldsymbol{\varepsilon}^{\mathrm{el}}, D, r) = \frac{1}{2\rho}(1-D)\boldsymbol{\varepsilon}^{\mathrm{el}} \cdot \mathbb{C}[\boldsymbol{\varepsilon}^{\mathrm{el}}] + \frac{q}{r}\left[r + \frac{1}{b}\exp(-br)\right] + \frac{H}{2\rho}r^2 \qquad (5.16)$$

The stress σ is the energetic derivative with respect to strain:

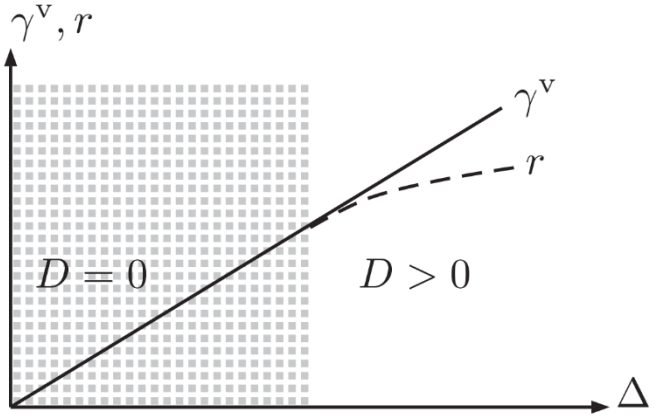

Figure 5.7: Comparison between plastic arc length $\dot{\gamma}_{\mathrm{v}}$ in (5.18) and hardening variable r in (5.19) as a function of the displacement Δ of the bonding components. (Livermore Sofware Technology Corporation (LSTC), 2016)

$$\boldsymbol{\sigma} = \rho \frac{\partial \psi}{\partial \boldsymbol{\varepsilon}^{\mathrm{el}}} = (1 - D)\mathbb{C}[\boldsymbol{\varepsilon}^{\mathrm{el}}] \tag{5.17}$$

The Eq. (5.17) differs by the continuity $\Psi_{\mathrm{d}} = (1 - D)$ from the stress-strain relationship in Eq. (4.3). The evolution of damage D causes a degradation of the constant elastic stiffness tensor $\mathbb{C}$ from the definition according to Eq. (4.3).

5.3.4. Hardening evolution equations

The hardening behaviour due to plastic deformation is expressed by means of the shear-based plastic arc length $\dot{\gamma}_{\mathrm{v}}$:

$$\dot{\gamma}^{\mathrm{v}} := \sqrt{2}\,\varepsilon^{\mathrm{v}} = \lambda \sqrt{2 \frac{\partial f_{\mathrm{MS}}^{*}}{\partial \boldsymbol{\sigma}} \cdot \frac{\partial f_{\mathrm{MS}}^{*}}{\partial \boldsymbol{\sigma}}} = \frac{2\lambda}{(1 - D)^{2}} \sqrt{J_2 + \frac{2}{3}\left(a_2^{*} \langle I_1 \rangle\right)^{2}} \tag{5.18}$$

Only the deviatoric stresses as well as the tensile stresses cause the development of the arc length $\dot{\gamma}_{\mathrm{v}}$. The rate of the hardening variable $\dot{r}$ corresponds to the arc length $\dot{\gamma}_{\mathrm{v}}$ according to Eq. (5.18) extended by $(1 - D)$. Using the effective stresses σ^{eff} according to Eq. (4.32) this can be written as:

$$\dot{r} := (1 - D)\dot{\gamma}^{\mathrm{v}} = 2\lambda \sqrt{J_2^{\mathrm{eff}} + \frac{2}{3}\left(a_2^{*} \langle I_1^{\mathrm{eff}} \rangle\right)^{2}} \tag{5.19}$$

This definition introduces the concept of *damaged plastic arc length* for the accumulated hardening variable r. The development of r through the continuity $(1 - D)$ until complete failure $D = 1$ decreases continuously which is qualitatively shown in Figure 5.7 over any differential

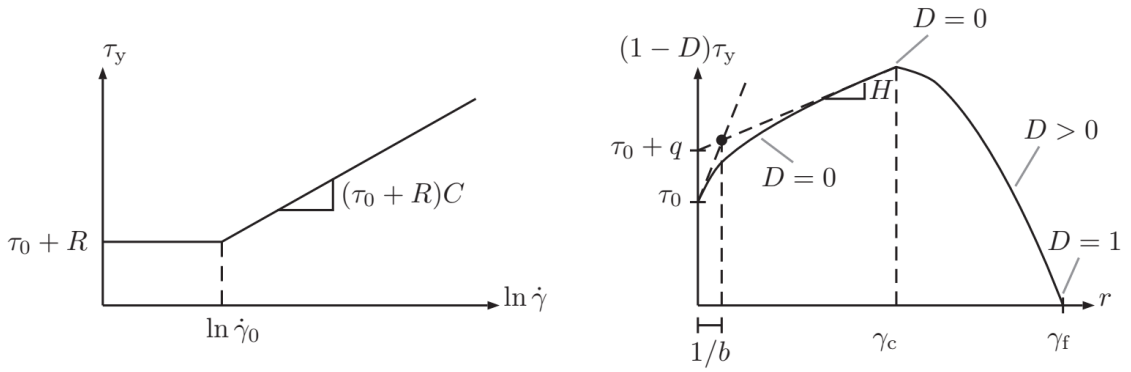

Figure 5.8: Left: Shear yield stress τ_Y as a function of the strain rate $\dot{\gamma}_v$; Right: Damaged shear yield stress $(1-D)\tau_Y$ with non-linear hardening and damage development for rate-independent material behaviour. (Burbulla, Matzenmiller, & Kroll, 2015)

displacement Δ in the adhesive between the steel components. In the case of an undamaged material for $D = 0$, both comparative quantities are identical.

5.3.5. Yield shear stress

The shear yield stress τ_Y is formed additively from the flow start τ_0 and the nonlinear hardening stress R according to the rate-dependent Johnson & Cook approach:

$$\tau_Y = (\tau_0 + R)\left(1 + C\left\langle \ln \frac{\dot{\gamma}}{\dot{\gamma}_0} \right\rangle\right) \tag{5.20}$$

with the norm of the strain rate $\dot{\varepsilon}$ with respect to the shear strain rate:

$$\dot{\gamma} := \sqrt{2\dot{\boldsymbol{\varepsilon}} \cdot \dot{\boldsymbol{\varepsilon}}} \tag{5.21}$$

In the left Figure 5.8 the shear strength τ_Y from Eq. (5.20) is shown as a function of the strain rate $\dot{\gamma}$; starting from the static strength $(\tau_0 + R)$, it increases logarithmically starting from the reference value $\dot{\gamma}_0$ with the strain rate $\dot{\gamma}$. Due to Macauley bracket, strain rates below the value $\dot{\gamma}_0$ do not increase the shear strength (5.20), so the influence of the hardening rate for a quasistatic load can be neglected. The hardening R is derived from the derivative of the energy function φ in Eq. (5.16) over the hardening variable r in Eq. (5.19) and in turn consists of a declining exponential function with q and b as material constants, and the linear approach Hr according to the hardening modulus H:

$$R = \rho \frac{\partial \psi}{\partial r} = q[1 - \exp(-br)] + Hr \tag{5.22}$$

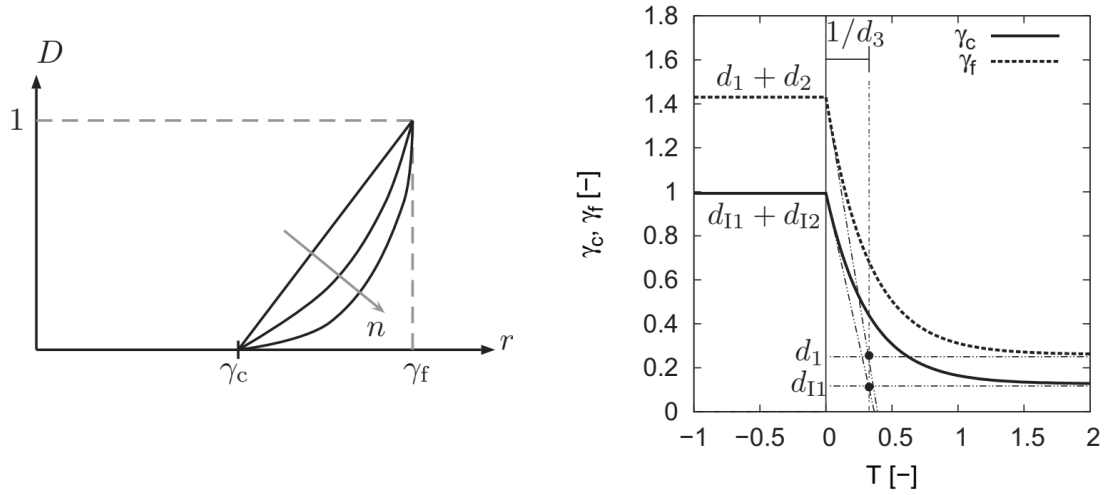

Figure 5.9: Left: Development of the damage variable D with respect to n exponent; Right: Critical strain γ_c at damage initiation and breaking point γ_f according to Eqs. (5.26) and (5.27) for rate-independent material as a function of triaxiality T. (Burbulla, Matzenmiller, & Kroll, 2015)

A representation of the shear yield stress τ_Y including the hardening R and the softening due to damage development D can be plotted in the right Figure 5.8 over the accumulated, shear-based hardening variable r according to the rate equation (5.19). The initial non-linear hardening R in Eq. (5.22) turns asymptotically into the linear hardening range for damage $D = 0$. The rate at which the exponential function declines can be influenced by means of the constant b.

5.3.6. Damage model

The degradation of the material strength is described by the continuity of $\Psi_d = (1 - D)$ according to Section 4.2.2. For this purpose, a suitable model for the development of damage D is needed. A simple empirical damage approach is used, for one-dimensional stresses as a function of the hardening variable r at the rate of Eq. (5.19), extended by the exponent n, so that the softening behaviour can be adapted to the experimental data with sufficient accuracy:

$$D = \left\langle \frac{r - \gamma_c}{\gamma_f - \gamma_c} \right\rangle^n , \ \gamma_c \leqslant r \leqslant \gamma_f \tag{5.23}$$

The qualitative trend of damage variable D in Eq. (5.23) is plotted for varying n in the $r - D$ diagram in Figure 5.9 on the left. The difference between the hardening variable r and the critical strain γ_c at stress maximum – see also Figure 5.9 right – in the numerator of Eq. (5.23) determines the beginning of the damage $D = 0$. The difference in the denominator between critical strain γ_c and the strain limit γ_f determines the release speed for $D > 0$. The damage model is written for three-dimensional arbitrary loads and reads:

$$\dot{D} = n\left\langle \frac{r-\gamma_{\mathrm{c}}}{\gamma_{\mathrm{f}}-\gamma_{\mathrm{c}}} \right\rangle^{n-1} \frac{\dot{r}}{\gamma_{\mathrm{f}}-\gamma_{\mathrm{c}}} \tag{5.24}$$

where the critical strain γ_{c} and the strain limit γ_{f} are not constant here but are formulated below as a function of the stress state.

The measure of the stress state is the triaxiality T, which represents the ratio of the hydrostatic stress σ_{m} to the Mises reference stress σ_{eq}:

$$T := \frac{\sigma_{\mathrm{m}}}{\sigma_{\mathrm{eq}}} \tag{5.25}$$

The critical strain at the beginning of the damage,

$$\gamma_{\mathrm{c}} = \left[d_{\mathrm{I}1} + d_{\mathrm{I}2}\exp\left(-d_3\langle T\rangle\right)\right]\left(1 + d_4\left\langle \ln\frac{\dot{\gamma}}{\dot{\gamma}_0}\right\rangle\right) \tag{5.26}$$

and at the breaking point,

$$\gamma_{\mathrm{f}} = \left[d_1 + d_2\exp\left(-d_3\langle T\rangle\right)\right]\left(1 + d_4\left\langle \ln\frac{\dot{\gamma}}{\dot{\gamma}_0}\right\rangle\right) \tag{5.27}$$

are each described using the approach of Johnson & Cook. The damage initiation γ_{c} and the breaking point γ_{f} are affine to each other. This can be influenced by choosing the parameters d_{Ii} or d_i with $i = 1, 2$ – shown in Figure 5.9 right. The slopes with $1/d_3$ of the curves γ_{c} and γ_{f} are identical for $T = 0$ in order to avoid intersections of the curves for $d_{I1} \approx d_1$ and $d_{I2} \approx d_2$. The failure point γ_{f} can thus not occur before the damage initiation γ_{c}. The triaxiality (5.25) in the two approaches (5.26) and (5.27) is used to evaluate the brittleness by axial tensile components. In the case of large triaxiality values, the damage sets in earlier, and in the pressure range the initiation and breakage lines remain constant according to equations (5.26) and (5.27). The hydrostatic compressive stress state does not result in plastification – see also the flow condition (5.9) and Figure 5.9. Thus, there is no damage evolution $\dot{T}$ according to Eq. (5.24) as a result of plastic deformation, since $r = 0$ holds for this stress case. The rate-dependent term in equations (5.26) and (5.27) has an additional parameter d_4 that is different from C in Eq. (5.20). The parameter d_4 determines the influence of the loading rate $\dot{\gamma}$ according to Eq. (5.21) on the initiation or damage. In the case of $d_4 = 0$, the initiation or damage remains rate-independent and the development of the plastic arc length (5.18) is determined exclusively by plastic deformation.

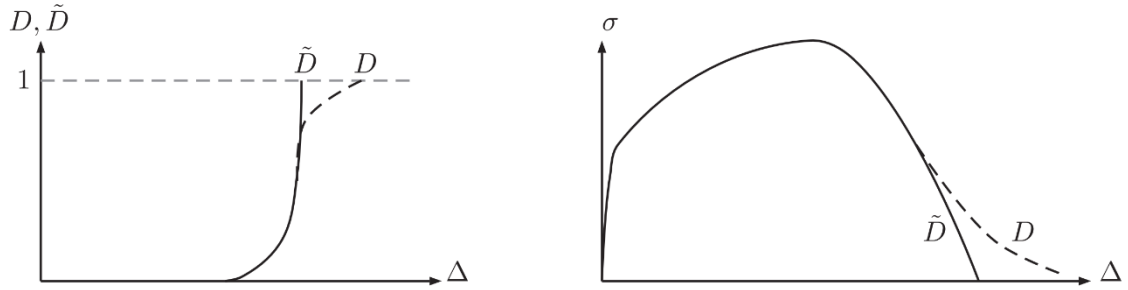

Figure 5.10: Left: Development of the damage models D and $\tilde{D}$ according to (5.23) and (5.29); Right: Qualitative stress-displacement curves for both damage models. (Burbulla, Matzenmiller, & Kroll, 2015)

The volume-specific elastic energy release y for linear elastic material behaviour, which is released in the elastic stiffness decrease in the case of damage – see also Section 4.2.2 – is a negative energetic conjugate quantity for damage D according to [Coleman and Gurtin, 1967] defines:

$$y := -\rho \frac{\partial \psi}{\partial D} = \frac{1}{2} \boldsymbol{\varepsilon}^{\mathrm{el}} \cdot \mathbb{C}[\boldsymbol{\varepsilon}^{\mathrm{el}}] = \frac{\sigma_{\mathrm{eq}}^2}{2E(1-D)^2} \left[\frac{2}{3}(1+\nu) + 3(1-2\nu)T^2 \right] \tag{5.28}$$

The onset of the stress-strain relationship (5.17) leads to the energy release y as a function of the Mises comparison stress σ_{eq} according to Eq. (5.2) and the triaxiality T (5.25) as well as the material constants elastic modulus E and Poisson's ratio υ. The volume-specific elastic energy release y in Eq. (5.28) is comparable to the fracture-mechanical energy release $\mathcal{G}$ according to Eq. (4.27) for an elastic-brittle material behaviour.

The effect of using the plastic arc length γ^{v} instead of the accumulated plastic strain r for the phenomenological description of the softening in Eq. (5.18) gives:

$$\tilde{D} = \left\langle \frac{\gamma^{\mathrm{v}} - \gamma_{\mathrm{c}}}{\gamma_{\mathrm{f}} - \gamma_{\mathrm{c}}} \right\rangle^{n} , \; \dot{\tilde{D}} = n \left\langle \frac{\gamma^{\mathrm{v}} - \gamma_{\mathrm{c}}}{\gamma_{\mathrm{f}} - \gamma_{\mathrm{c}}} \right\rangle^{n-1} \frac{\dot{\gamma}^{\mathrm{v}}}{\gamma_{\mathrm{f}} - \gamma_{\mathrm{c}}} \tag{5.29}$$

Compared to γ^{v}, r develops more slowly as the damage D increases. This has the consequence that the damage D according to Eq. (5.23) also takes place more slowly than the damage $\tilde{D}$ according to Eq. (5.29) for the case of plastic arc length, exemplified in Figure 5.10 for $n = 2$. The development of D after the initiation of damage, in contrast to the damage course of $\tilde{D}$, is characterized by a turning point – see Figure 5.10 on the left. This inflection point is reflected in the stress-displacement diagram in the right Figure 5.10; the softening curve asymptotically approaches the displacement axis. However, the fracture point γ_{f} for the damage model D in Eq. (5.23) is defined

by the shear-based hardening variable r and is clearly determinable in the right-hand diagram in Figure 5.10.

5.4. Compilation of the material model

A independent formulation of the presented material model according to Table 2 is implemented in LS-Dyna® since version R7.1.1. In the following, the presented material model is generally described to as *MAT252 or Toughened Adhesive POlymer model (TAPO). The first model with the addition YIELD1 = MS contains the flow condition f_{MS} according to Eq. (5.9) and the second with YIELD2 = DPS the flow criterion f_{DPS} according to Eq. (5.11). All variants use the accumulated, shear-based hardening variable r at the rate of Eq. (5.19) for the description of the hardening behaviour in the material.

Flow conditions (YIELD)	
Eq. (5.9)	$f_{\mathrm{MS}} := \frac{J_2}{(1-D)^2} + \frac{a_2}{3}\left\langle \frac{I_1}{1-D} + \frac{\sqrt{3}\,a_1\tau_0}{2a_2}\right\rangle^2 - \frac{1}{3}\left(\tau_{\mathrm{Y}}^2 + \frac{a_1^2\tau_0^2}{4a_2}\right) = 0$
Eq. (5.11)	$f_{\mathrm{DPS}} := \frac{J_2}{(1-D)^2} + \frac{1}{\sqrt{3}}a_1\tau_0\frac{I_1}{1-D} + \frac{a_2}{3}\left\langle \frac{I_1}{1-D}\right\rangle^2 - \tau_{\mathrm{Y}}^2 = 0$
Plastic potential	
Eq. (5.12)	$f_{\mathrm{MS}}^* := \frac{J_2}{(1-D)^2} + \frac{a_2^*}{3}\left\langle \frac{I_1}{1-D}\right\rangle^2 - \tau_{\mathrm{Y}}^2$
Plastic potential	
Eq. (5.13)	$\dot{\boldsymbol{\varepsilon}}^{\mathrm{pl}} = \lambda\frac{\partial f_{\mathrm{MS}}^*}{\partial\boldsymbol{\sigma}} = \frac{\lambda}{(1-D)^2}\left(\boldsymbol{\sigma}^{\mathrm{D}} + \frac{2}{3}a_2^*\langle I_1\rangle\mathbf{1}\right)$
Shear-based hardening variables	
Eq. (5.18)	$\dot{\gamma}^{\mathrm{v}} := \sqrt{2}\,\varepsilon^{\mathrm{v}} = \lambda\sqrt{2\frac{\partial f_{\mathrm{MS}}^*}{\partial\boldsymbol{\sigma}}\cdot\frac{\partial f_{\mathrm{MS}}^*}{\partial\boldsymbol{\sigma}}} = \frac{2\lambda}{(1-D)^2}\sqrt{J_2 + \frac{2}{3}\left(a_2^*\langle I_1\rangle\right)^2}$
Eq. (5.19)	$\dot{r} := (1-D)\dot{\gamma}^{\mathrm{v}} = 2\lambda\sqrt{J_2^{\mathrm{eff}} + \frac{2}{3}\left(a_2^*\langle I_1^{\mathrm{eff}}\rangle\right)^2}$
Isotropic hardening	
Eq. (5.20)	$\tau_{\mathrm{Y}} = (\tau_0 + R)\left(1 + C\left\langle \ln\frac{\dot{\gamma}}{\dot{\gamma}_0}\right\rangle\right)$
Eq. (5.22)	$R = \rho\frac{\partial\psi}{\partial r} = q[1-\exp(-br)] + Hr$
Triaxiality	
Eq. (5.25)	$T := \frac{\sigma_{\mathrm{m}}}{\sigma_{\mathrm{eq}}}$

Shear strain on damage initiation and breakage	
Eq. (5.26)	$\gamma_c = [d_{I1} + d_{I2}\exp(-d_3\langle T\rangle)]\left(1 + d_4\left\langle \ln\frac{\dot{\gamma}}{\dot{\gamma}_0}\right\rangle\right)$
Eq. (5.27)	$\gamma_f = [d_1 + d_2\exp(-d_3\langle T\rangle)]\left(1 + d_4\left\langle \ln\frac{\dot{\gamma}}{\dot{\gamma}_0}\right\rangle\right)$
Damage evolution	
Eq. (5.24)	$\dot{D} = n\left\langle\frac{r-\gamma_c}{\gamma_f-\gamma_c}\right\rangle^{n-1}\frac{\dot{r}}{\gamma_f-\gamma_c}$
Eq. (5.29)	$\dot{D} = n\left\langle\frac{\gamma^v-\gamma_c}{\gamma_f-\gamma_c}\right\rangle^{n-1}\frac{\dot{\gamma}^v}{\gamma_f-\gamma_c}$

Table 2: Constitutive Equations of the LS-Dyna® *MAT252 Toughened-Adhesive-Polymer material model

5.5. Material card parameter description

An overview of the LS-Dyna® Toughened Adhesive Polymer model (TAPO) material card can be found in Figure 5.11. Since parameters that control the elasto-plastic and damage behaviour of the adhesive joint are referred to a pure shear stress state, any identification process should begin from the correlation of experimental data arising from tests of such nature. Once the simulation curve is adequately correlated with the experimental one, parameters that govern the shape of the damage envelope must be set. To that end, data from pure tensile stress tests must be used. Finally, combined shear and tensile stress tests should be used as validation models, so some parameters from the material card can be adjusted so the material can offer an accurate and realistic behaviour.

As can be seen in Figure 5.11, first row of the card contains some parameters common to any material such as ρ, E and υ, which are respectively the mass density, Young's modulus and Poisson's ratio of the structural adhesive it is intended to be characterized. E and υ parameters together with the THICKNESS parameter of the adhesive layer defined in the *MAT_ADD_COHESIVE card (explained in chapter 6) allow the user to characterize the elastic regime of the material in both pure shear and pure tensile scenarios.

On the same row three flags can be found, that allow the user to choose among different formulations of the adhesive behaviour, which were explained along section 5.3. These flags and their relationships with the previously shown are the following:

FLG — Flag to choose between yield functions f and $\hat{f}$
FLG = 0. Schlimmer in tension, Drucker & Prager in compression (see Eq. (5.9) and Figure 5.5).

FLG = 2. Schlimmer in tension, Von Mises in compression (see Eq. (5.11) and Figure 5.4).

JCFL — Johnson & Cook constitutive failure criterion (see Eq. (5.25)).
JCFL = 0. Use triaxiality factor only in tension.
JCFL = 1. Use triaxiality factor in tension and compression.

DOPT — Damage criterion flag D or $\breve{D}$
DOPT = 0. Damage model uses damage plastic strain r (see Eq. (5.24)).
DOPT = 1. Damage model uses plastic arc length γ_v (see Eq. (5.29)).

The option JCFL controls the influence of triaxiality (5.25) in the pressure range for the thresholds γ_c and γ_f. In this way, the choice of JCFL = 0 makes use of the Macauley bracket $\langle T \rangle$ for the triaxiality and JCFL = 1 omits it. Besides, it must be noted that the previous choice of the DOPT parameter influences the shape of the softening curve, as shown qualitatively in Figure 5.9 left.

Card 1	1	2	3	4	5	6	7	8
Variable	MID	RO	E	PR	FLG	JCFL	DOPT	
Type		F	F	F	I	I	I	

Card 2	1	2	3	4	5	6	7	8
Variable	LCSS	TAU0	Q	B	H	C	GAM0	GAMM
Type	I	F	F	F	F	F	F	F

Card 3	1	2	3	4	5	6	7	8
Variable	A10	A20	A1H	A2H	A2S	POW		
Type	F	F	F	F	F	F		

Card 4	1	2	3	4	5	6	7	8
Variable			D1	D2	D3	D4	D1C	D2C
Type			F	F	F	F	F	F

Figure 5.11: LS-Dyna® Toughened Adhesive Polymer model (TAPO) material card. Input types are divided into F, that stands for real numbers and I, which stands for integers, used for flags, curves or table identification.

In the second row of the material card the necessary parameters for the characterization of the plastic regime of the adhesive can be found. It must be taken into account that these are referred to a pure shear behaviour, so their characterization must be properly performed using a test that provides this response on the adhesive layer. The data input can be performed whether by direct parameter specification or by the input of a curve ID. If the second option is chosen, it must be taken into account that the input curve must specify yield stress τ_Y as a function of plastic strain r. Material card parameters are explained next. Besides, a graphical explanation of them can be found in right-hand Figure 5.8.

TAU0 Initial shear yield stress τ_Y.

Q Isotropic nonlinear hardening modulus q.

B Isotropic exponential decay parameter b.

H Isotropic linear hardening modulus H.

The rest of the parameters of the row (C, GAM0 and GAMM) control the dynamic behaviour of the structural adhesive. Strain rate effects are not inside the scope of the present work, so they will not be taken into account in the present analysis.

In the third row, yield function parameters A10, A20 and plastic potential parameter A2S can be found, according to Eqs. (5.9), (5.11) and (5.12) respectively. These parameters define the shape of the load envelope and thus they change the shape of the stress-strain curves belonging to the pure shear and combined stress modes. They should be adjusted once the elasto-plastic characterization of the pure shear loading case has been completed. Apart from them, POW parameter is the n exponent that must be set in order to adjust the shape of the damaged part of the curve according to Figure 5.9 (left).

Finally, Johnson & Cook threshold parameters form the fourth and last row of the material card, according to Eqs. (5.26) and (5.27). D1C and D2C calibrate the damage onset while D1 and D2 set the failure point of the material. D3 is a damage parameter that potentiates the triaxilality effects so its influence must be taken into account when modelling combined stress states.

Chapter 6

FEM Modelling of Adhesive Bonds

After presenting the theoretical background of the material model *MAT252 in chapter number five, this chapter shows a detailed explanation on how adhesive bonds are modelled using LS-Dyna®. A suitable technique in this case for the modelling of adhesive bonds must be able to recreate with enough accuracy, according to the used material model, its physical behaviour with a reasonable computational cost. For this, the final purpose of this work must be kept in mind, which is the modelling of adhesive joints in full vehicle crash simulations. In them, the size of the model and the complexity of its design – in terms of geometry, contacts... – makes necessary to develop a straigthforward methodology that does not disrupt the work of the analyst. In addition, the new adhesive modelling methodologies must maintain simulation times in the range of interest for design in the industrial framework.

The next pages describe the proposed methodology, emphasizing topics such as the cohesive element formulation, the modelling of the connections between the adhesive and the substrate or the optimum mesh size to be used.

This methodology will be later applied to the construction of the FEM models of the test specimens used for the parameter identification of the *MAT252 material model, which are described in chapter seven. Futhermore, it will be used in the construction of the component-level validation models discussed in chapter eight.

6.1. Cohesive element formulation

The cohesive fomulation connects via nonlinear springs the relative displacements between upper and lower surfaces of an element to a force per unit area. A three-dimensional element has then a two-dimensional constitutive behaviour. The deformation is computed in terms of the relative displacements between the upper and lower surfaces interpolated at the Gauss points instead of the strains. Unlike these, the incoming deformations have units of length. Figure 6.1 shows a schematic representation of a cohesive element, in which the midsurface must be aligned on the same plane of the adhesive joint, and each group of nodes – 1-2-3-4 and 5-6-7-8 – must be joined to the corresponding elements belonging to the adherend surface.

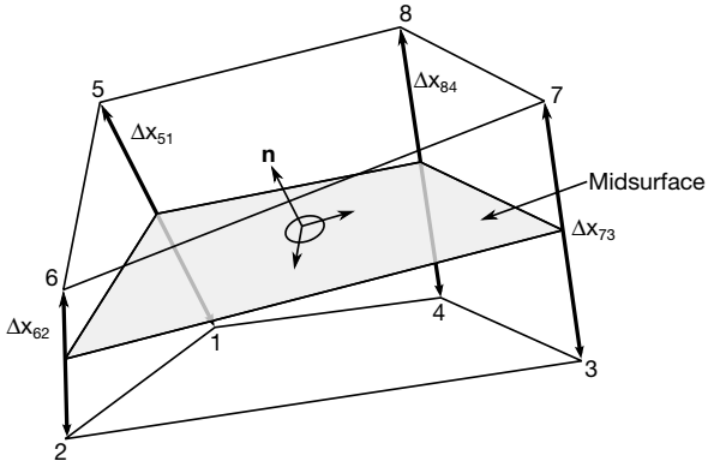

Figure 6.1: Schematic representation of an 8-node cohesive element

Cohesive elements possess 3 kinematic variables, namely, two relative displacements δ_1, δ_2 in tangential directions and one relative displacement δ_3 in normal direction. In a corresponding constitutive model, they are used to compute three associated traction stresses t_1, t_2 and t_3. For example, in the elastic case:

$$\begin{bmatrix} t_1 \\ t_2 \\ t_3 \end{bmatrix} = \begin{bmatrix} E_T & 0 & 0 \\ 0 & E_T & 0 \\ 0 & 0 & E_N \end{bmatrix} \begin{bmatrix} \delta_1 \\ \delta_2 \\ \delta_3 \end{bmatrix} \tag{6.1}$$

On the other hand, hypoelastic 3D material models for standard solid elements are formulated with respect to six independent strain rates and six associated stress rates, e.g. for isotropic elasticity:

$$\begin{bmatrix} \dot{\sigma}_{xx} \\ \dot{\sigma}_{yy} \\ \dot{\sigma}_{zz} \\ \dot{\sigma}_{xy} \\ \dot{\sigma}_{yz} \\ \dot{\sigma}_{zx} \end{bmatrix} = \frac{E}{(1+\nu)(1-2\nu)} \begin{bmatrix} 1-\nu & \nu & \nu & 0 & 0 & 0 \\ \nu & 1-\nu & \nu & 0 & 0 & 0 \\ \nu & \nu & 1-\nu & 0 & 0 & 0 \\ 0 & 0 & 0 & 1-2\nu & 0 & 0 \\ 0 & 0 & 0 & 0 & 1-2\nu & 0 \\ 0 & 0 & 0 & 0 & 0 & 1-2\nu \end{bmatrix} \begin{bmatrix} \dot{\varepsilon}_{xx} \\ \dot{\varepsilon}_{yy} \\ \dot{\varepsilon}_{zz} \\ \dot{\varepsilon}_{xy} \\ \dot{\varepsilon}_{yz} \\ \dot{\varepsilon}_{zx} \end{bmatrix} \tag{6.2}$$

To be able to use such three-dimensional material models in a cohesive element environment, an assumption is necessary to transform three relative displacements to six strain rates. Since cohesive elements are intended to simulate the crack growth and not the material surrounding it, this kind of elements shows no stiffness for lateral expansion or in-plane shear loading:

$$\begin{bmatrix}\delta_1\\ \delta_2\\ \delta_3\end{bmatrix} \rightarrow \begin{bmatrix}\dot{\varepsilon}_{xx}\\ \dot{\varepsilon}_{yy}\\ \dot{\varepsilon}_{zz}\\ \dot{\varepsilon}_{xy}\\ \dot{\varepsilon}_{yz}\\ \dot{\varepsilon}_{zx}\end{bmatrix} = \begin{bmatrix}0\\ 0\\ \dot{\delta}_3/(t+\delta_3)\\ 0\\ \dot{\delta}_2/(t+\delta_3)\\ \dot{\delta}_1/(t+\delta_3)\end{bmatrix} \tag{6.3}$$

where t is the initial thickness of the adhesive layer. These strain rates are then used in a 3D constitutive model to obtain new Cauchy stresses, where 3 components can finally be used for the cohesive element:

$$\begin{bmatrix}\sigma_{xx}\\ \sigma_{yy}\\ \sigma_{zz}\\ \sigma_{xy}\\ \sigma_{yz}\\ \sigma_{zx}\end{bmatrix} \rightarrow \begin{bmatrix}t_1\\ t_2\\ t_3\end{bmatrix} = \begin{bmatrix}\sigma_{zx}\\ \sigma_{yz}\\ \sigma_{zz}\end{bmatrix} \tag{6.4}$$

There are two cohesive element formulations in LS-Dyna®: ELFORM 19 and 20. Element type 19 is an 8-node cohesive element. The tractions on the mid-surface defined as the mid-points between the nodal pairs 1-5, 2-6, 3-7, and 4-8 (see Figure 6.1) are functions of the differences of the displacements between nodal pairs interpolated to the four integration points. These are calculated in the local coordinate system defined at the centroid of the element. ELFORM 19 must be used when bonding solid elements together, while ELFORM 20 is identical but with offsets for use with shells. The element is assumed to be centered between two layers of shells on the cohesive element's lower (1-2-3-4) and upper (5-6-7-8) surfaces. The offset distances for both shells are one half the initial thicknesses of the nodal pairs (1-5, 2-6, 3-7, and 4-8) separating the two shells. These offsets are used with the nodal forces to calculate moments that are applied to the shells. A schematic comparison of the two types of formulations can be seen in Figure 6.2.

The use of any cohesive element formulation (ELFORM 19 or 20) in the modelling of adhesive layers involves a series of differences with respect to the use of their equivalent solid elements (ELFORM 1 or 2). The reduction in the number of variables to three (one in the direction normal to the joint plane and two contained in it) translates into an increase in the computational efficiency and a greater simplicity when analyzing physical behaviour of the adhesive. However, the simplification carried out often results in a loss of precision in the results obtained. Nevertheless, we must not lose sight of the practical approach of this work, aimed at its application in component and complete vehicle crash simulations, in which the effects produced by the lack of precission introduced for the use of cohesive elements does not represent an important deviation in the results.

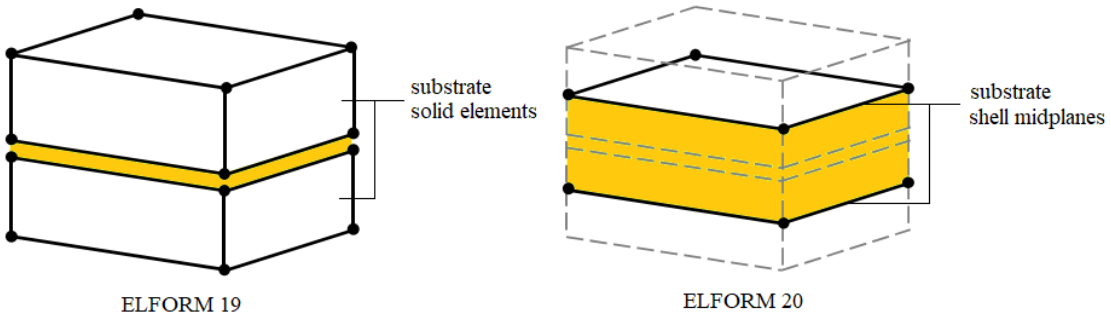

Figure 6.2: Schematic comparison of two cohesive element formulations available in LS-Dyna®

Due to its ease of use in order to model interfaces and considering its reduction of computational costs, a cohesive element formulation has been applied in this work for modelling adhesive layers with *MAT252 in LS-Dyna®. Depending on the type of element that the substrate is made of (solids or shells), a different formulation must be used (ELFORM 19 or 20 respectively). Originally developed to be used with solid elements only, material model *MAT252 can be used with cohesive elements in combination with the option *MAT_ADD_COHESIVE.

*MAT_ADD_COHESIVE offers the possibility to use a selection of 3-dimensional cohesive models in LS-Dyna® in conjuction with cohesive elements. Figure 6.3 shows its empty card where the variables used to characterize its behaviour can be seen. PID identifies the Part ID for which the cohesive property applies. ROFLG is a flag that indicates for whether adhesive density is specified per unit area or volume. In the case the geometric definition of the adhesive layer has important design defects, such as important variations of thickness or zones where this tends to zero, this flag can be activated in order to avoid numerical instability. However in this case, ROFLG will be set as equal to zero in the further presented models.

Card 1	1	2	3	4	5	6	7	8
Variable	PID	ROFLG	INTFAIL	THICK				
Type	I	F	F	F				

Figure 6.3: Overview of LS-Dyna® *MAT_ADD_COHESIVE option card

INTFAIL parameter ranges from 0 to 4 and sets the number of integration points required for the cohesive element to be deleted. If it is zero, the element will not be deleted even if it satisfies the failure criterion. A variation in the parameter from 1 to 4 does not influence substantially the obtained simulation curves.

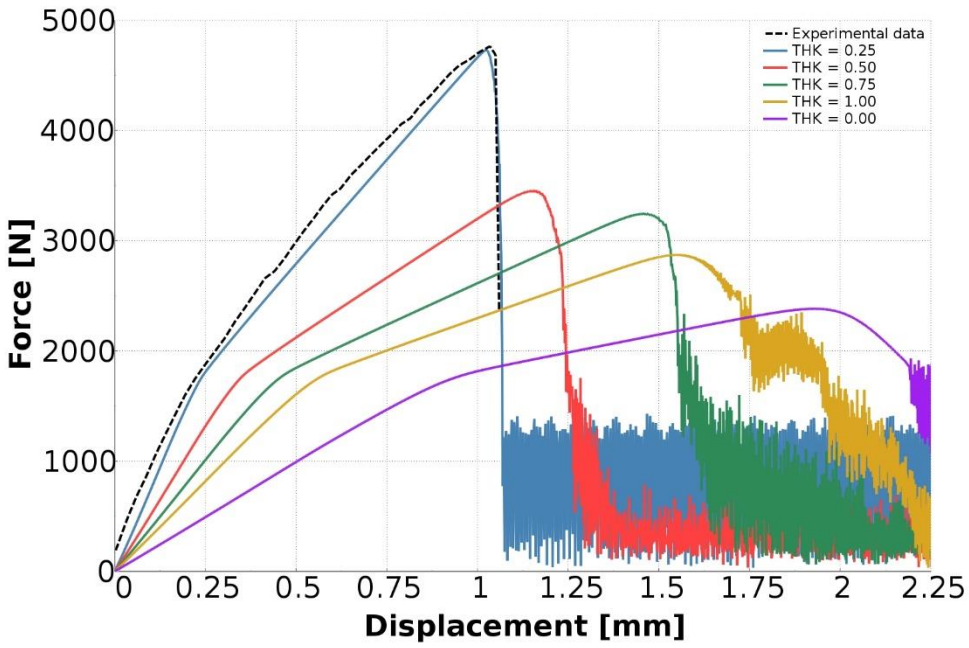

Figure 6.4: Influence of THK parameter with constant geometrical thickness = 0.25 in simulations of a lap shear strength test

In last place, THICK parameter is used to impose a thickness in the adhesive model for the computation of strains in the constitutive model (Eq 6.5). If it is equal to zero, the actual thickness of the cohesive element is used, defined in the model geometry. Otherwise a user specified thickness can be input. A FEM model for the normalized lap shear strength test (ASTM D1002) has been used in order to study the influence of this parameter in the results of simulations involving adhesive bonds. The followed process starts from the study of the influence of the variation of the THICK parameter in a model with a constant geometrical thickness, equal to 0.25mm as defined by the standard. Figure 6.4 shows the obtained results. Disregarding the correlation with the experimental data, it can be observed that a variation of THICK parameter causes important deviations in the simulation results, both in the slope of the elastoplastic regime, and thus in the reached strength and the damage mode of the adhesive. This fact is exposed in Eqs. (6.5) and (6.6), where pure tensile E_n and shear E_s moduli are calculated in terms of Young's modulus E and Poisson's ratio υ which are material-dependent properties, and the thickness of the layer t which can vary:

$$E_n = \frac{E(1-\nu)}{(1+\nu)(1-2\nu)}\frac{1}{t} \tag{6.5}$$

$$E_s = \frac{E}{2(1+\nu)}\frac{1}{t} \tag{6.6}$$

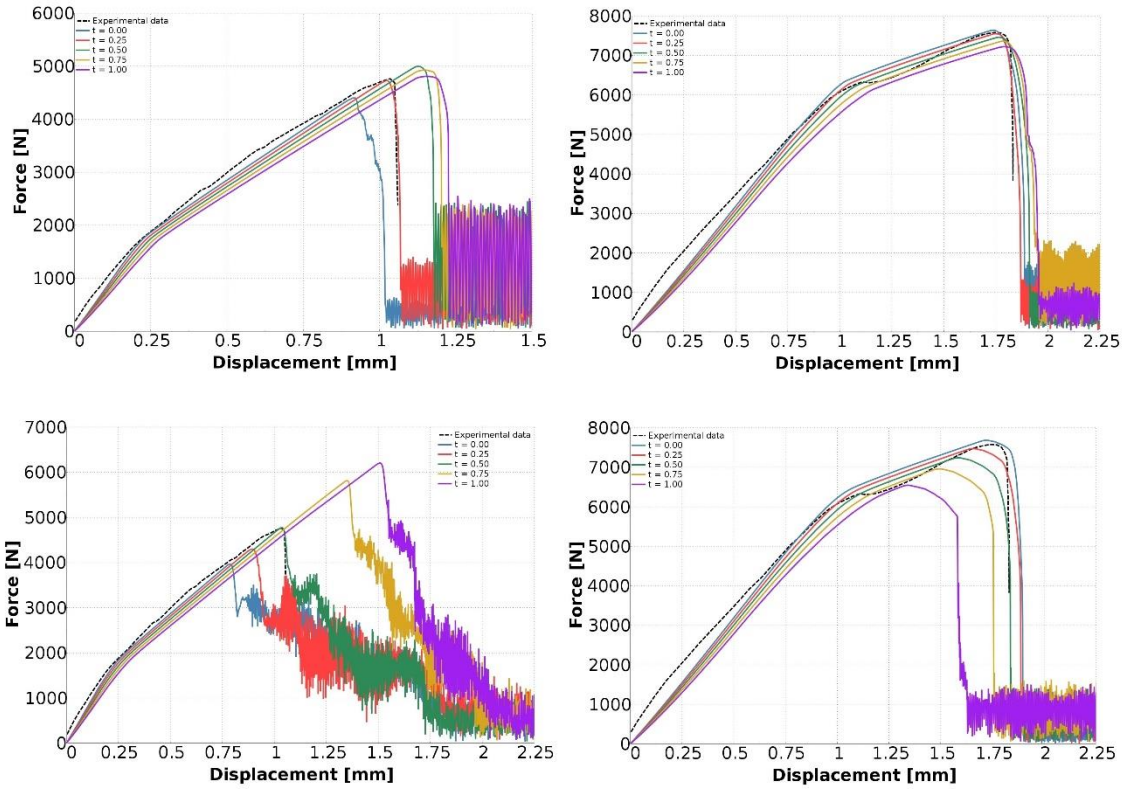

Figure 6.5: Influence of geometrical thickness with constant THK = 0.25 (up) and THK = 1.00 (down) using two adhesive samples - Versilok® 273LGB/331 (left) and E1009827/25GB (right) – in the simulation of a lap shear strength test

Three possibilities arise from these results, which are setting THICK parameter equal to 0.0 – the thickness of the layer as defined in the model geometry – 0.25mm – which is the theoretical thickness of the layer – and 1.00mm, that would not modify the resulting stiffness according to Eqs. (6.5) and (6.6) and would ease the parameter identification process.

The possibility of setting THICK = 0.0 is dismissed since it means that the stiffness of the adhesive layer would depend of the accuracy in the definition of the geometry of the layer, which can not be guaranteed. Thickness can be easily controlled when simple models are used like test specimen or in certain components but it can be unreliable when bigger and more complex models are used.

Two structural adhesives from LORD Corporation - Versilok® 273LGB/331 and E1009827/25GB – have been tested in a FEM model of the lap shear strength test using constant THICK parameter and a varying layer thickness. This is used in order to check the influence that possible variations in the definition of the geometry would have in the simulation results. A comparison of the obtained curves for THICK = 0.25 and THICK = 1.00 are exposed respectively in Figure 6.5. There it can be observed that influence of imprecisions in the model geometry is greater

when THICK parameter is equal to 1.00. With this in mind, hereafter THICK parameter will be set equal to the actual thickness of the adhesive layer and the parameter identification of the material model will be performed on this basis.

6.2. Contact definition

The practical aim of the methodology described in the present chapter is also important when defining the interfaces between adhesive and substrate. Merging the nodes belonging to the substrate or to the adhesive into a single one would be the most efficient way of working from a computational point of view.

The models exposed in the following chapters have simple geometries that would allow to create coincident and equally distributed meshes. However, in service conditions with complicated geometries and very often non-matching substrate meshes, the construction of a layer composed of cohesive elements with pasted nodes on both sides can be considered as difficult when not directly impossible. Thus, interfaces in this work are always defined by means of the creation of a contact. Figure 6.6 shows schematically the exposed problem and helps to understand the adopted solution.

In LS-Dyna®, a contact is defined by identifying (via parts, part sets, segment sets, and/or node sets) what locations are to be checked for potential penetration of a slave node through a master segment. A search for penetrations, using any of a number of different algorithms, is made every time

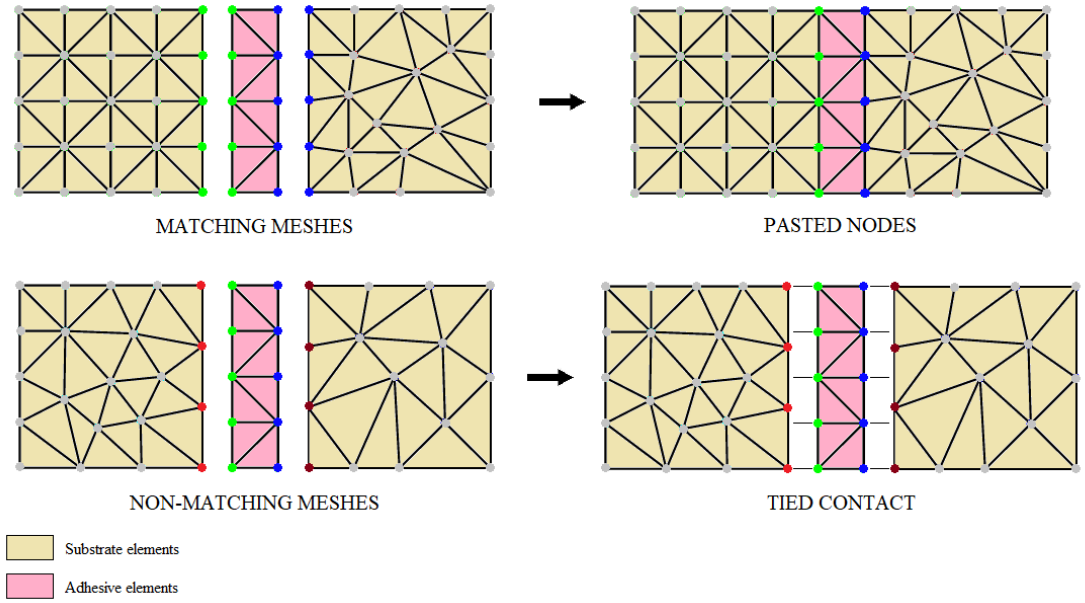

Figure 6.6: Schematic description of tied contact definition in the case of non-matching between adhesive and substrate meshes

step. Contact types fall into 2 major categories: constraint-based and penalty-based. In the case of a penalty-based contact, when a penetration is found a force proportional to the penetration depth is applied to resist, and ultimately eliminate, the penetration. A large number of contact types are offered in LS-Dyna®. Some types are for specific applications, and others are suitable for more general use. Among them, a tied contact bonds two surfaces forming a contact pair together for the duration of a simulation. It constrains each of the nodes on the slave surface to have the same value of displacement (or any other physical quantity) as the point of the master surface that it contacts. Thus, definition of a tied contact is the chosen option in this methodology to model the link between substrate and adhesive.

As mentioned before, in tied contact types, the slave nodes are constrained to move with the master surface. At the beginning of the simulation, the nearest master segment for each slave node is located based on an orthogonal projection of the slave node to the master segment. If the slave node is deemed close to the master segment based on established criteria, the slave node is moved to the master surface. In this way, the initial geometry may be slightly altered without invoking any stresses. As the simulation progresses, the isoparametric position of the slave node with respect to its master segment is held fixed using kinematic constraint equations.

Alternately, the OFFSET option can be used for tied contacts. These contacts use a penalty-based formulation, and works the same as above but an offset distance between the master segment and the slave node is permitted. In this way, moments that are developed due to the offset are not taken into account.

The choice of one contact or another depends on the formulation of the substrate and the geometrical definition of the adhesive joint. Regardless the coincidence of the meshes at both sides of the interface, coincidence of planes defined by the substrate and the adhesive must be taken into account. If these planes are not coincident are there are gaps between the surfaces of the substrate

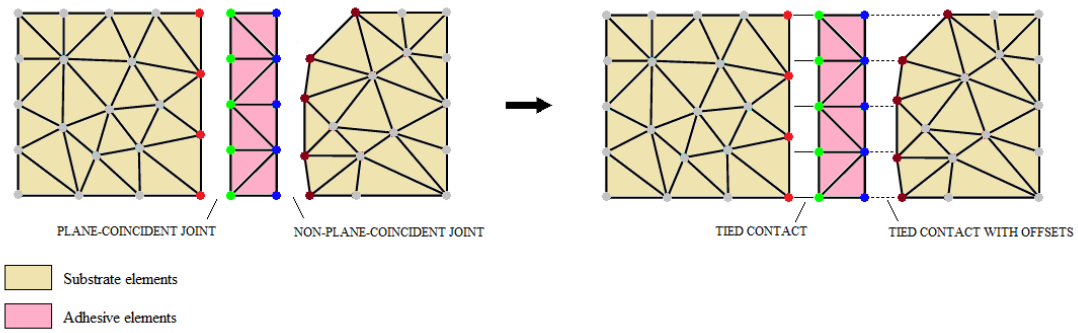

Figure 6.7: Schematic description of tied contact definition in terms of plane-coincidence between adhesive and substrate

and the adhesive, then the OFFSET option must be applied to the tied contact. Figure 6.7 illustrates this issue and Table 3 summarizes the type of contact to be used depending on the formulation of the adhesive and the geometry of the substrates to be bonded.

	ELFORM 19	ELFORM 20
Plane-coincident geometry	*CONTACT_TIED_NODES_TO_SURFACE	*CONTACT_TIED_SHELL_EDGE_TO_SURFACE
Non plane-coincident geometry	*CONTACT_TIED_NODES_TO_SURFACE_OFFSET	*CONTACT_TIED_SHELL_EDGE_TO_SURFACE_OFFSET

Table 3: Contact type definition in terms of the element formulation of the adhesive and the interface geometry

Attention must be paid to the definition of the contact tolerance due to the relatively small thickness of the adhesive layers. It is advisable to define a contact tolerance so every substrate segment captures only the nodes of the adhesive corresponding to its closest face and not the opposite one as well. On the other hand, when an offset tied contact is used, this offset of the slave node from the master segment in the normal direction cannot exceed the defined tolerance.

Also it is strongly recommended to define an automatic contact between the substrates excluding the adhesive elements. In case cohesive elements fail and are deleted, substrates are then susceptible to make contact with each other.

6.3. Finite Element mesh refinement

The obtained accuracy and the spent computational effort from any FEM simulation is inversely proportional to the finite element size that is used to construct the model. With this

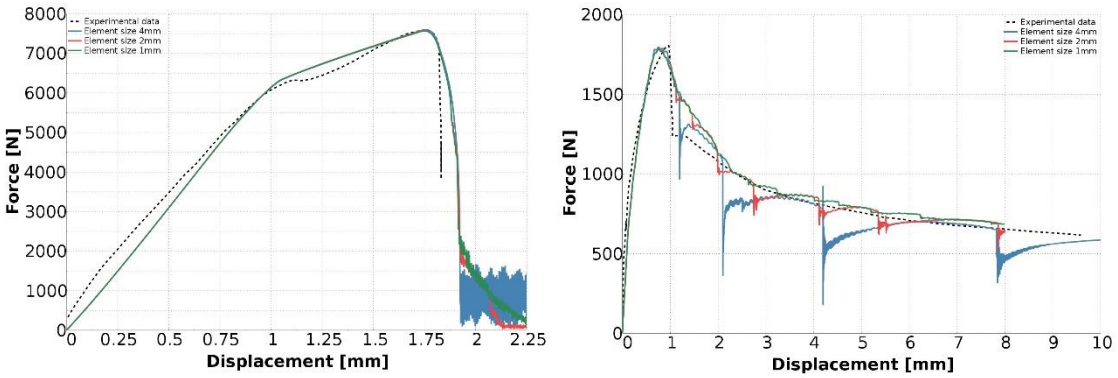

Figure 6.8: Influence of mesh refinement on results of simulations of lap shear strength and t-peel resistance tests

assumption an optimal mesh size for the structural adhesive modelling in automotive components must be defined.

To that end, FEM simulations of two standarized tests involving adhesive bonds – lap shear strength and t-peel resistance – have been used in order to study the effects that mesh refinement has on the obtained force versus displacement curves. These curves are exposed in Figure 6.8 and a time versus mesh size diagram for both tests is shown in Figure 6.9.

With respect to the lap shear strength test, the simplicity of its geometry and the uniformity of the stress state of its adhesive layer makes the elastoplastic regime not to vary regardless the mesh refinement. Yield and ultimate strengths are equally captured by the three meshes. Same behaviour can be observed in the case of the t-peel tests since the stress state only affects to the separating front of the adhesive layer, and thus the obtained peel load is similar in all the simulations.

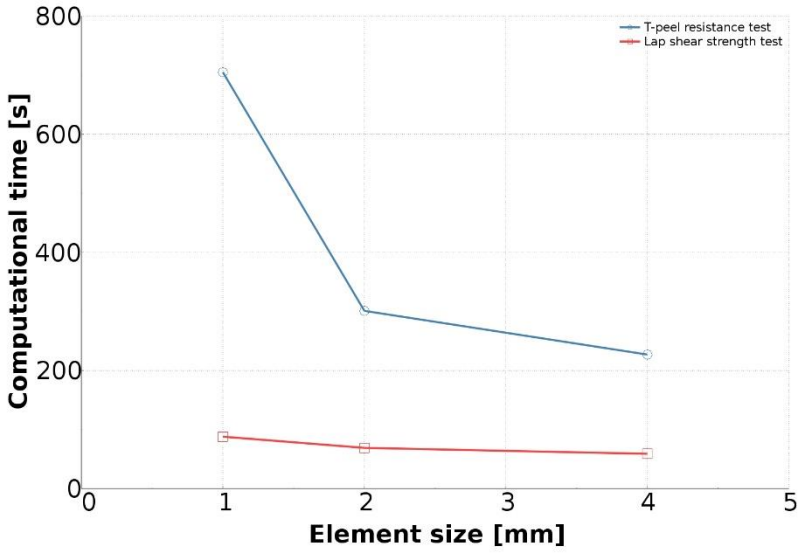

Figure 6.9: Computational time versus mesh refinement in simulations of lap shear strength and t-peel resistance tests

However, once the damage threshold has been crossed the breakage mode is different for every mesh size. A finer discretization makes the released energy be reduced when each adhesive element eliminates, thus the general breakage process takes place more progressively. As a result, the damage curve is smoother, the presence of oscillations gets reduced, and the simulation behaviour is closer to the experimental data. This is clearly reflected in the case of the t-peel test, where the dampened breakage of the specimen is more and more accurately captured by the simulation as the mesh gets refined.

Complexity of the breaking mechanisms of the t-peel test compared to the ones from the lap shear test is reflected in the computational times from Figure 6.9. A mesh refinement does not affect substantially in terms of computational effort when the stress state is uniform, but increases exponentially when non-homogeneous stress states come into play.

Therefore, taking into account the wide variety of stress states and the general complexity of a complete vehicle crash simulation, and observing the influence that simulation of adhesives would have on the overall computational cost, it is decided to set as an appropriate element size a value in the range of 4-6mm.

Chapter 7

Test Specimens for Material Characterization

This chapter describes four standarized tests that have been chosen to be used in order to characterize the LS-Dyna® material model *MAT252, whose theoretical background has been already exposed in chapter 5, making use of the FEM modelling guidelines exposed in chapter 6. These test specimens are the following:

- Butt-bonded hollow cylinders test
- KS2 test
- Lap shear strength test
- T-peel resistance test.

In the first two specimens uniform stress states are created, in a greater or lesser extent, over the complete adhesive layer to be examined, avoiding undesired local effects that might distort the results and induce to perform an unrealistic material characterization. Besides, both specimens are particularly significant for their versatility, being able to be used under different configurations in order to capture the behaviour of the adhesive layer not only under pure tensile or pure shear modes, but also under any combination of them. As mentioned before, this is important since adhesives present different behaviours depending on their loading conditions, so the effective usage of any of these two proposed methods would allow an accurate characterization of the material.

On the other hand, the second group of specimens (lap shear strength and t-peel resistance tests) are of a more complex nature and they are characterized by inducing non-homogeneous stress states in the adhesive layer. These tests are defined by the ASTM international standard and provide results that can be compared to the information usually specified in the technical datasheet of most commercial structural adhesives. An accurate characterization of the structural adhesive can be performed as well using these two specimens together.

In the following, the four proposed tests for characterization are studied in detail. In the subsequent sections the experimental setup, a description of the FEM model and a discussion of the simulation results obtained for each test specimen are presented.

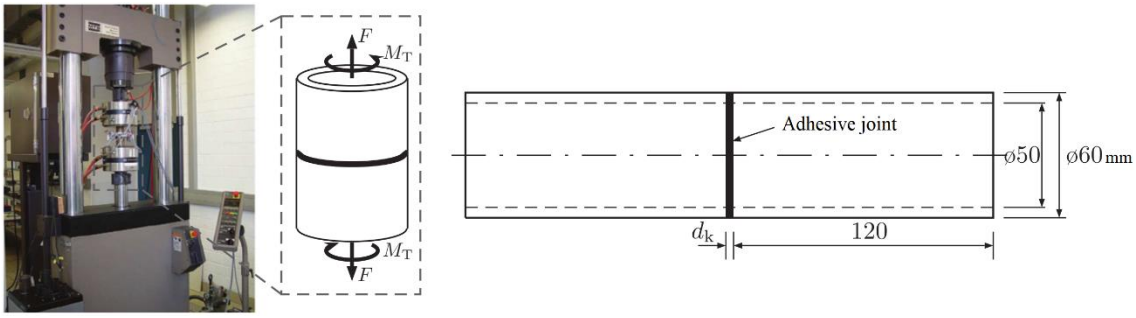

Figure 7.1: Left: testing device and experimental setup; right: geometry of the specimen of the butt-bonded hollow cylinders test. (Burbulla, Matzenmiller, & Kroll, 2015)

7.1. Butt-bonded hollow cylinders test

7.1.1. Experimental setup

Tests on the butt bonded double tube sample are based on the torsion tests according to ISO 11003-1:2001, modified (German version EN 14869-1:2011). The experimental results shown in this section have been carried out at the Institute of Materials Science (IfW) of the University of Kassel and can be found at (Burbulla, Matzenmiller, & Kroll, 2015).

By means of the experimental device shown in Figure 7.1 left, pure and combined tensile and shear stresses can be applied to thin adhesive layers with a nominal thickness of d_k = 0.2 mm. In this case, the specimen consists of two halves of steel tube, which are connected to each other by means of the adhesive to be examined - see Figure 7.1 on the right. In this case, the thermosetting structural adhesive Betamate® 1496V based on epoxy resin from DOW Automotive AG is the material to be tested in the present section.

The testing machine allows a controlled quasi-static load application, so that a resultant combination of torsional and axial stresses in the adhesive layer can be created. The longitudinal force F and the torsional moment M_T are measured with a load cell and by means of the unloaded sample cross-sectional area A and the section modulus Wp the normal and tangential to the joint plane stresses can be computed:

$$\sigma = \frac{F}{A} \quad , \quad \tau = \frac{M_T}{W_P} \tag{8.1}$$

The torsional load generates an approximately homogeneous state of shear stress in the adhesive layer. The load in the axial direction of the tube causes a uniaxial deformation state in the adhesive layer due to the rigid tube halves. This results in a triaxial stress state, which can be considered as approximately homogeneous.

In the measurement of the normal and tangential displacements between upper and lower halves - shown in the right-hand of Figure 7.1 - influence of the deformation of the specimen must be taken into account. Thus, the elastically assumed deformations of the steel-joining components along the measuring length $L_{measure}$ are determined with the known moduli of elasticity E^{Steel} and G^{Steel} as follows:

$$\Delta_{N_{exp}}^{Steel} = \sigma \frac{L_{measure} - d_k}{E^{Steel}} \quad , \quad \Delta_{T_{exp}}^{Steel} = \tau \frac{L_{measure} - d_k}{G^{Steel}} \tag{8.2}$$

The difference of the measured total deformation $\Delta_{N_{exp}}^{tot}$, $\Delta_{T_{exp}}^{tot}$ and the correction in Eq. (7.2) results in the deformation along the longitudinal and tangential direction of the adhesive layer itself:

$$\Delta_{N_{exp}} = \Delta_{N_{exp}}^{tot} - \Delta_{N_{exp}}^{Steel} \quad , \quad \Delta_{T_{exp}} = \Delta_{T_{exp}}^{tot} - \Delta_{T_{exp}}^{Steel} \tag{8.3}$$

The normal strain ε_{exp} and the tangential strain γ_{exp} are introduced via the deformations (7.3) of the adhesive layer:

$$\varepsilon_{exp} := \ln\left(\frac{\Delta_{N_{exp}}}{d_k} + 1\right) \quad , \quad \gamma_{exp} := \arctan\left(\frac{\Delta_{T_{exp}}}{d_k + \Delta_{N_{exp}}}\right) \tag{8.4}$$

ε_{exp} and γ_{exp} are not natural components of a continuum mechanic distortion tensor. They are limited exclusively to the description of the hollow cylinder test and they are used only to define the deformation ratio, which will be useful to quantitatively describe the pure or combined loading modes of the test. This deformation ratio is defined in Eq. (7.5) as follows:

$$\alpha_{exp} = \frac{\gamma_{exp}}{2\varepsilon_{exp}} \tag{8.5}$$

The deformation ratio α_{exp} is kept approximately constant during the experiment by means of a control device on the testing machine. As can be deduced from Eq. (7.5), ratio $\alpha_{exp} = 0.0$ represents the pure tension and $\alpha_{exp} = \infty$ represents the pure torsion test. In addition, any combination between tension and torsion is possible in order to perform a complete characterization of the adhesive. In this case $\alpha_{exp} = 0.5$ and $\alpha_{exp} = 2.0$ are used.

The experimental results for the butt-bonded hollow cylinder sample are shown in Figure 7.2 using the mentioned Betamate® 1496V adhesive. In the left diagram in Figure 7.2 the normal stresses are plotted versus the normal displacements and in the right diagram the corresponding results on the tangential direction are plotted in this case.

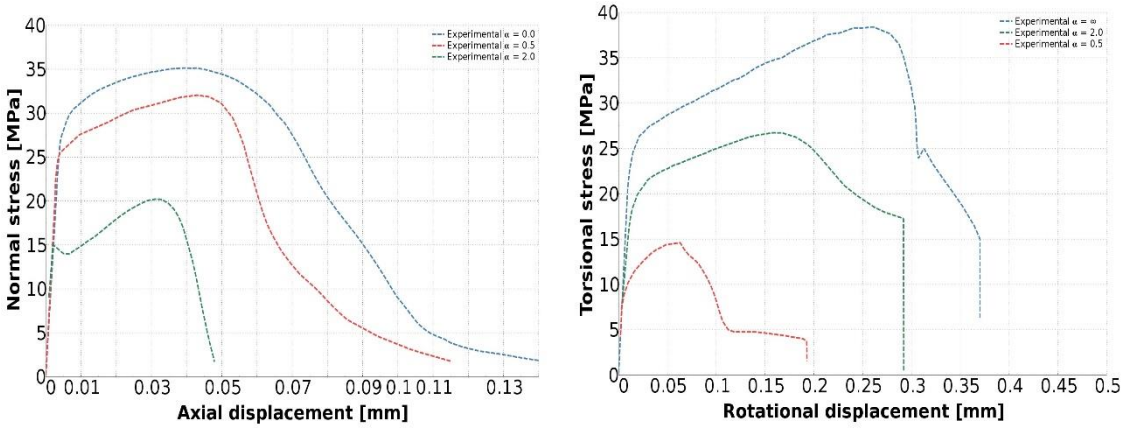

Figure 7.2: Stress versus displacement curves of the butt-bonded hollow cylinders test for pure axial, pure torsion and combined loading cases as found in [Schlimmer et al., 2002, FOSTA-P593, S.68-96]

7.1.2. Numerical model definition

A FEM model has been created in LS-Dyna® in order to simulate the experimental tests performed with the glued double tube sample explained in the previous section. For computational cost reasons and to avoid the introduction of numerical distortions arising from the substrate, the model does not represent the whole geometry of the sample, allowing a simplified and faster characterization. Instead of representing each of the tubes in its whole length (120mm), elastic deformation of steel is considered as negligible in this task due to the high stiffness of the steel compared to that of the adhesive layer. Thus, two rigid bodies are considered here to simulate the behaviour of the two steel halves. Figure 7.3 shows a perspective view of the FEM model used in the characterization.

Geometry of the steel tubes is discretized using two rings of 8-node solid elements, resulting 36 elements in each ring. As mentioned above, deformation of the steel parts is assumed to be negligible, so *MAT20 MAT_RIGID is used to describe its behaviour. Each part made from this material are considered to belong to a rigid body. Hence the fixed part is constrained in all its displacements and rotations, and the upper part is released depending on the test option that is going to be performed. For $\alpha_{\text{sim}} = 0.0$ (pure tensile mode) displacement along z-axis is allowed. On the contrary, for $\alpha_{\text{sim}} = \infty$ (pure torsion mode) rotation around z-axis is allowed only. For the different combined tests, both constraints must be released. Constant velocity curves are created as boundary conditions in order to define the simulation displacement according to the following table:

Deformation ratio α_{sim}	Axial displacement $\Delta_{N_{sim}}$[mm]	Torsional displacement $\Delta_{T_{sim}}$[mm]
0.00	0.02	0.00
0.50	0.02	0.02
2.00	0.08	1.25
∞	0.00	2.00

Table 4: Axial and torsional displacement for boundary condition definition for different deformation ratios of the butt-bonded hollow cylinders test.

Relation between axial and rotational velocities arise from the Eq. (7.5), and rotational velocity applied to the upper rigid body in this case is derived from basic kinematics by means of the following expression:

$$v_{T_{sim}} = v_{\theta_{sim}} R_{ext} \tag{8.6}$$

Where v_θ is the angular velocity of the rigid body, R_{ext} is the outer radius of the sample (equal to 30mm in this case) and v_T is the tangential velocity of the pipe half.

With respect to the adhesive layer, this is discretized using regular cohesive elements (ELFORM 19) with a thickness of 0.2mm, which in this case coincides with the real thickness of the sample since no shells elements are used to model the substrates. Same element size than the substrate

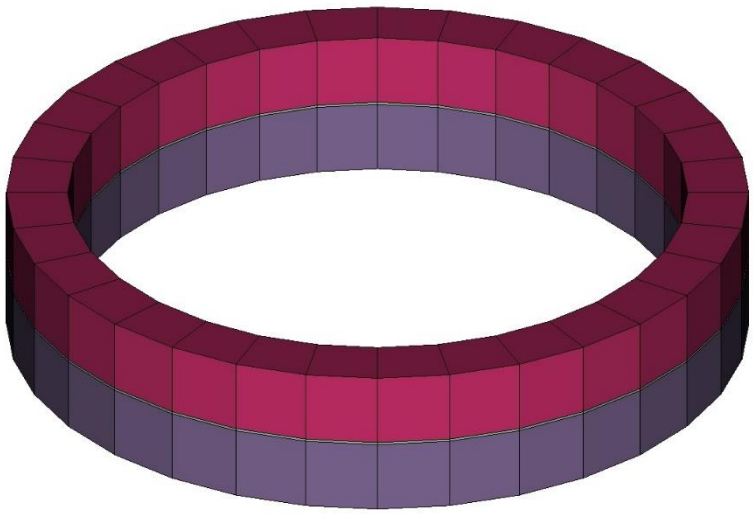

Figure 7.3: FEM model of the butt-bonded hollow cylinder test specimen used for *MAT252 parameter identification in LS-Dyna®

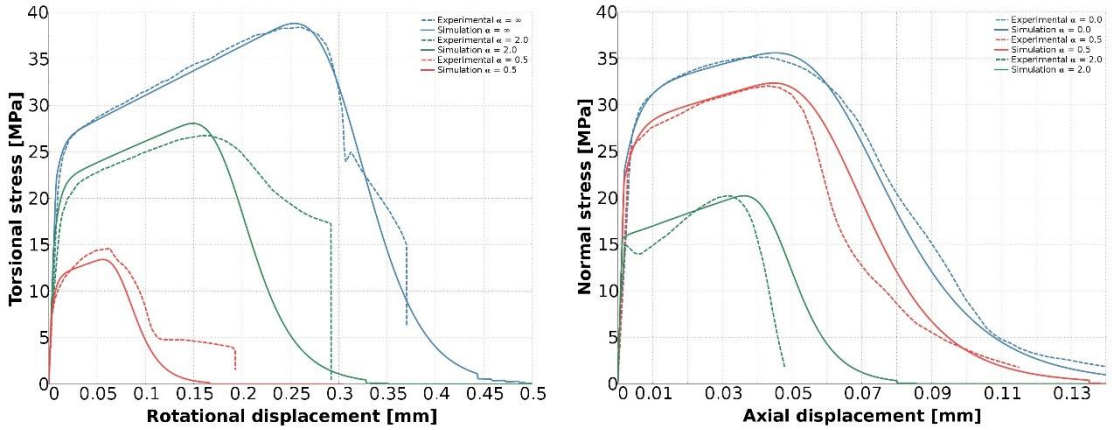

Figure 7.4: Comparison of simulation results with experimental data of the butt-bonded hollow cylinders test for different values of deformation ratio α

elements in the other two directions of the space is used, resulting 36 cohesive elements in the adhesive layer ring as well. *MAT_ADD_COHESIVE option is mandatory if *MAT252 material model is used with a cohesive element formulation. Although the simple definition of the model would allow the nodes of the two interfaces to be shared, two tied contacts (*CONTACT_TIED_NODES_TO_SURFACE) are defined between the parts following the guidelines exposed in chapter 6.

Finally, a database cross section is created on the adhesive layer in order to evaluate the resultant axial force F and torsional moment M_T over the sample. The use of these results in combination with the sample area A and the section modulus W_P in the Eq. (7.1) provide the stresses over the adhesive sample that must be correlated with the available experimental data.

7.1.3. Simulation results

An identification process of the material card parameters has been carried out as explained in section 5.5. The obtained results compared to the experimental data for each experiment using different values for deformation ratio α are shown in Figure 7.4. It can be observed that a precise correlation has been accomplished for both pure tests, particularly in the capture of the yield and ultimate strengths of the structural adhesive. There is a certain loss of accuracy in the case of combined loading cases, although the material model is able to capture the characteristic behaviour of the sample. Besides, the representation of the three different regimes of the curve (elastic, hardening and softening) is clearly obtained. Regarding the differences between the combined tests, results for $\alpha_{sim} = 0.5$ show a better correlation than in the case of $\alpha_{sim} = 2.0$. A parameter identification by means of an optimization software like LS-OPT® is advisable in this case although it lies outside the scope of this work.

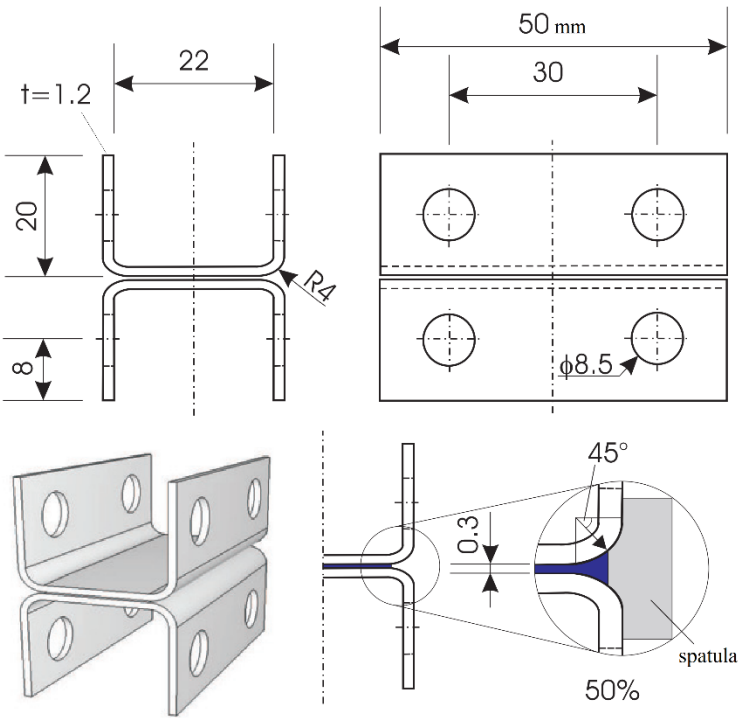

Figure 7.5: KS2 specimen geometry and adhesive layer definition. (Burbulla, Matzenmiller, & Kroll, 2015)

7.2. KS2 test

7.2.1. Experimental setup

The KS2 (Kopfzug-Scherzugprobe) test was originally developed for bonding research at the Laboratory for Materials and Joining (LWF) of the University of Paderborn and has been traditionally used for testing behaviour and performance of spotwelded components.

The specimen geometry is shown in Figure 7.5. It consists of two U-shaped high-strength steel (DP-K 30/50+Z140) plates of 50x22mm^2, bonded to each other by means of an adhesive joint. This adhesive layer has a thickness dk = 0.3mm and covers a surface of 16 × 22mm^2. The joint filling is defined with respect to the sides of the KS2 sample by means of a spatula, as can be observed as well in Figure 7.5. This is important since percentage of joint filling has a strong influence on the joint strength.

As in the previous case of the butt-bonded hollow cylinders test, the use of four different setups depending on the load application angle for the KS2 test allows an accurate examination of the adhesive joint under quasi-static load - see Figure 7.6. The test under a load angle of 90º

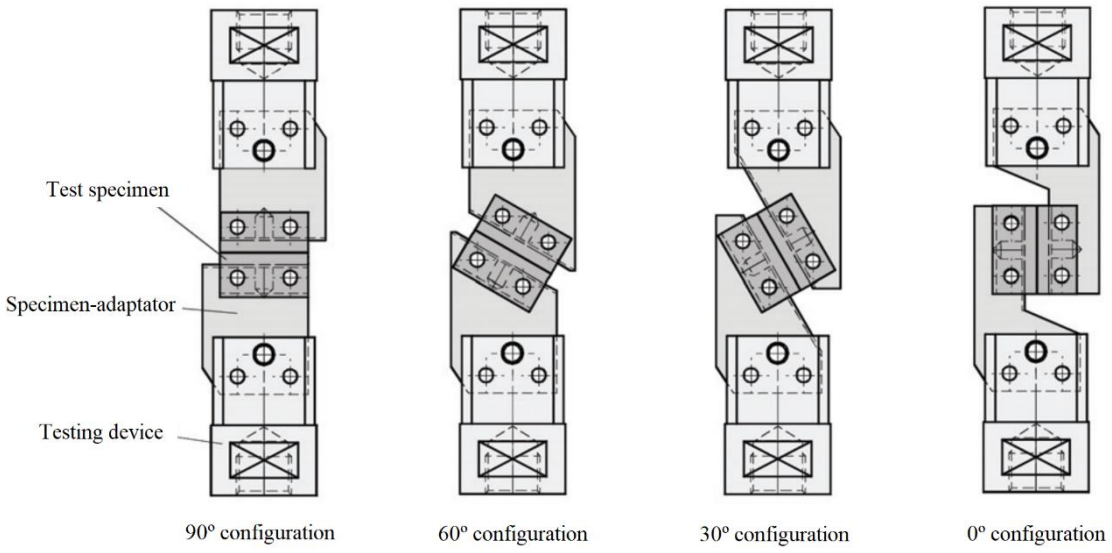

Figure 7.6: Experimental set-up for the KS2 test specimen under four different loading configurations. (Burbulla, Matzenmiller, & Kroll, 2015)

corresponds to the experimental setup of a pure tensile test. In contrast, the stress state under a load angle of 0º is comparable to that from a pure shear test. Furthermore the intermediate stress angle, as commonly occurs in real bonded components, allows a complete characterization of the material. 30º and 60º are the most common values. Obviously they can be changed or even extended in order to get a more detailed characterization of the structural adhesive.

The resulting force versus displacement curves of the experimental tests performed on the structural adhesive Betamate® 1496V from DOW Automotive AG – also tested using the butt-bonded hollow cylinders test – under four different load angles are shown in Figure 7.7. Results show again a characteristic behaviour in this kind of material, where strength strongly depends on the stress state of the adhesive layer. Note that an increase in the loading angle produces a decrease in the reached ultimate strength, from an optimal value of approximately 13MPa for 0º (pure shear mode) to 4MPa in the case of 90º (pure tensile mode).

7.2.2. Numerical model definition

The present work is focused on a material characterization with the aim of representing structural adhesives behaviour in component-level and full vehicle crash simulations. Thus, the possibility of performing a simplification of the KS2 specimen geometry is studied by the construction of two FEM models. The first one, the so-called model A, represents the geometry in detail as can be observed in upper Figure 7.8. On the contrary, as shown in lower Figure 7.8, in model B the geometry of the sample has been simplified by deleting the through holes and considering each

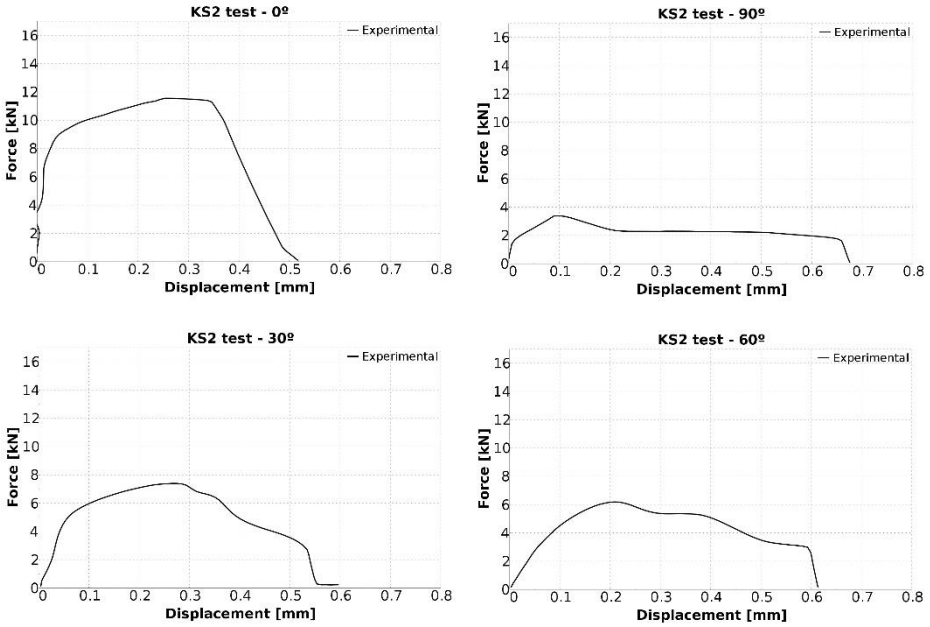

Figure 7.7: Force versus displacement curves obtained from quasi-static experimental tests using different configurations of the KS2 specimen, under pure shear and pure tensile loading modes (above) and combined loading modes (below).

U-shaped plate as a continuous surface. Since the substrate steel plates are be subjected to significant solicitations under this kind of test, exceeding its yield strength, they are considered to deform plastically, being characterized by means of the LS-Dyna® material model *MAT24 MAT_PIECEWISE_LINEAR_PLASTICITY.

The chucks that exert the pulling force of the testing machine over the specimen are represented in two different manners depending on the chosen model. In model A, the whole plate surface become plastically deformable. The effect of the testing device is achieved by filling the four through holes with shells and modelling them as rigid bodies by means of the *MAT20 MAT_RIGID material model. Upper holes are then released in the direction of the pulling force and lower holes are fully costrained. In the case of model B, each U-plate has been divided into two parts. The outer parts - the ones that are in contact with the chucks – are defined by means of the *MAT20 MAT_RIGID material model so they behave like rigid bodies. The fixed plate is constrained in all its degrees of freedom, while the moving plate is allowed to move only in the corresponding direction of the experiment, depending on the imposed deviation angle.

Since a coarse discretization of the substrate is done and cohesive elements for the modelling of the adhesive layer are used, in both cases the specimen is entirely represented. Computational efficiency is not considered to increase significantly if only one half of the geometry was modelled, taking advantage of the symmetry of the specimen. Discretization of the KS2 steel plates is performed

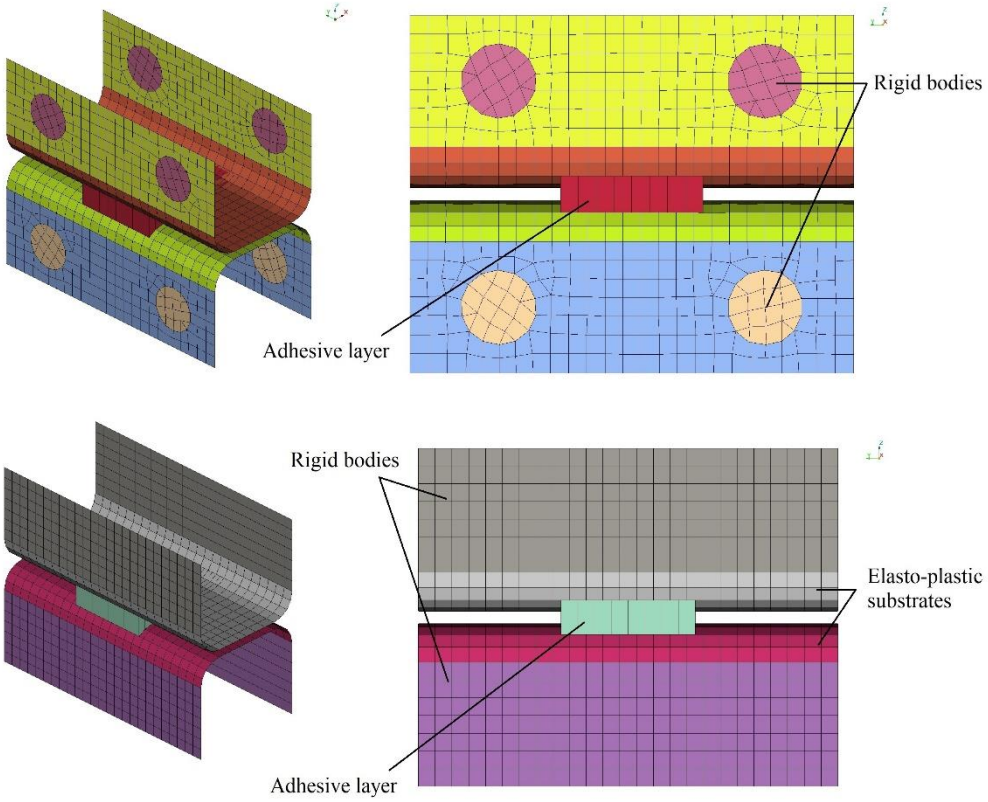

Figure 7.8: Perspective and side views of the two FEM models (up, model A; down, model B) of the KS2 test specimen used for *MAT252 parameter identification in LS-Dyna®

by means of 4-noded shell elements using ELFORM 10, Belytschko-Wong-Chiang formulation and a mesh size of approximately 2mm. Following the geometrical description of the specimen exposed in Figure 7.5, shell thickness is set to 1.2mm. Boundary conditions are set on the moving rigid bodies through the definition of a local coordinate system, that will have different angles depending on the experiment to be performed.

The adhesive layer is discretized using cohesive elements (ELFORM 20) with offsets that allow them to be used with shells, using a 2mm mesh size as well. The *MAT_ADD_COHESIVE option is added to the part that contains the cohesive elements so they can be characterized by *MAT252 material model. Both adhesive surfaces are linked to the corresponding substrate by means of the definition of tied contacts.

A database cross section is defined on the plastic part of one of the plates in order to evaluate the obtained forces and to compare them with the experimental data.

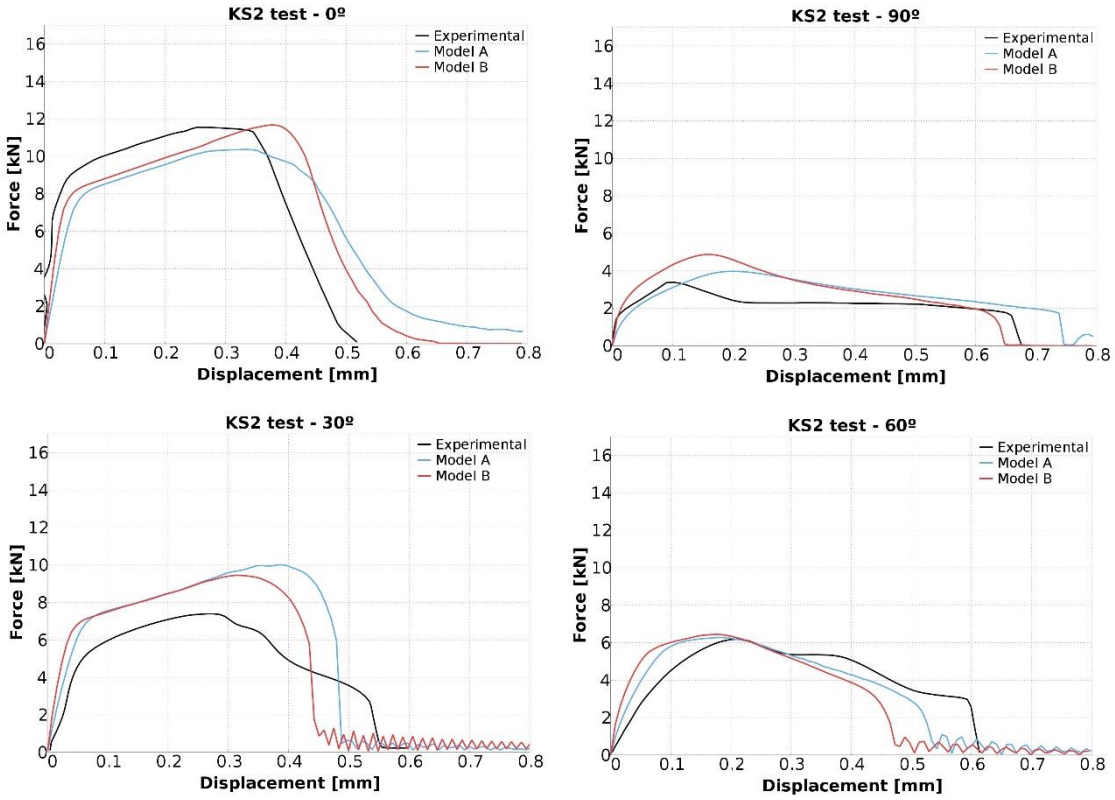

Figure 7.9: Comparison of simulation results with experimental data of the KS2 test, under pure shear and pure tensile loading modes (above) and combined loading modes (below).

7.2.3. Simulation results

A material characterization has been conducted using the two previously described FEM models in LS-Dyna®. Figure 7.9 shows the correlation between the experimental data and the simulation results for the four different configurations of the KS2 tests performed on a sample of structural adhesive Betamate® 1496V. As happened in the case of the butt-bonded hollow cylinders tests, a significant level of correlation is reached for the experiments involving pure stress modes. Values of yield and ultimate strength are accurately captured, and so does the hardening and softening behaviour of the adhesive. However, although the characteristic parts of the curve have been captured by the simulation, correlation of the combined loading modes is not so precise as in the pure loading modes, and thus the use of an optimization tool such as LS-OPT® should be mandatory in this case.

Despite the apparent simplicity of the specimen, damage behaviour of the adhesive layer can present a great deal of complexity, causing the exposed lack of accuracy between simulation and experimental data. Various mechanical and geometrical aspects influence the behaviour of this adhesive bond. The joining components, consisting of thin sheets, experience strong plastic deformations in the loading direction. In addition, the strength of the adhesive layer varies due to the

gap filling at the radii of the U-shaped plates. These phenomena cause that the stress state within the adhesive layer becomes non-homogeneous. The damage and subsequent failure of the adhesive begins at the edges of the layer, gradually spreading to the whole surface, as can be seen in Figure 7.10.

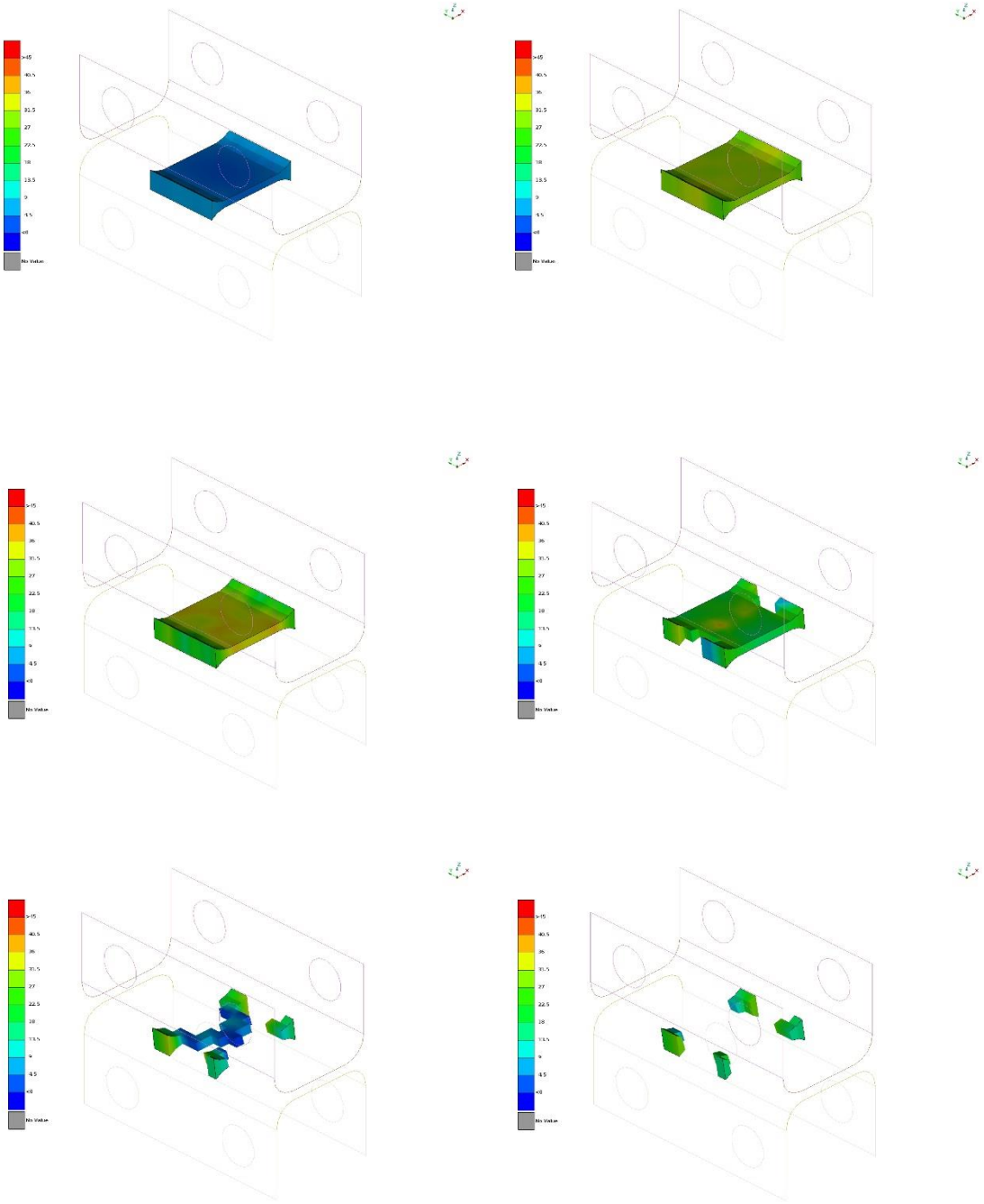

Figure 7.10: Contour plot of stresses on the adhesive layer under different configurations and stages of a pure shear KS2 test

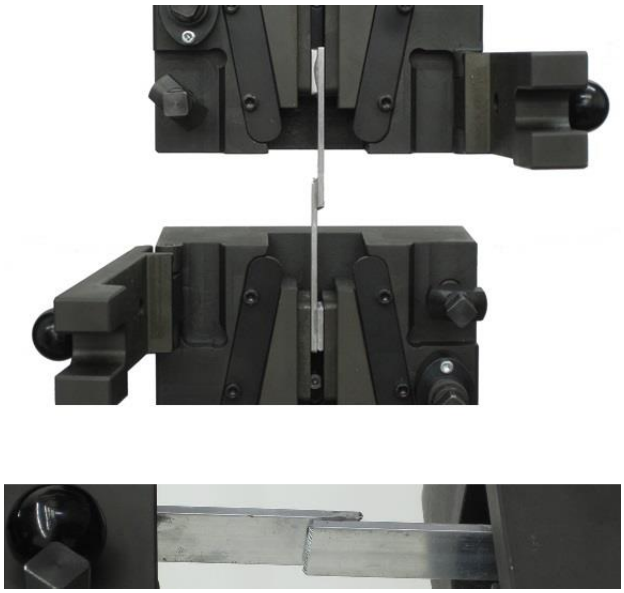

Figure 7.11: Side and detail view of the adhesive lap shear strength testing device. (admet.com)

7.3. Lap shear strength test

7.3.1. Experimental setup

As mentioned before, shear joints impose uniform stresses across the bond area which results in the highest possible joint strength. Lap shear strength test – as defined by the standard ASTM D1002 – is commonly used as a guideline for testing the strength of adhesives to bond metals. This testing standard can be used on single-lap-joint specimens to determine adhesive strength, surface preparation parameters and adhesive environmental durability.

In order to perform the test, two metal plates are bonded together with adhesive and cured as specified. The assembly is then cut into uniform width lap shear specimens. The test specimens are placed in the grips of a universal testing machine and pulled at 1.3 mm/min until rupture occurs. The grips used to secure the ends of the assembly must align so that the applied force is applied through the centerline of the specimen. The type of failure can be either adhesive (the adhesive separates from one of the substrates) or cohesive (the adhesive ruptures within itself).

As can be seen in Figure 7.12, the recommended lap shear specimen is 25.4 mm (1”) wide, with an overlap of 12.7 mm (0.5”). The recommended metal thickness is 1.62 mm (0.064”) and the overall length of the bonded specimen should be 177.8 mm (7”). The specimen failure should occur in the adhesive, and not in the substrate – thus the metal thickness and the length of the overlap may be adjusted as necessary.

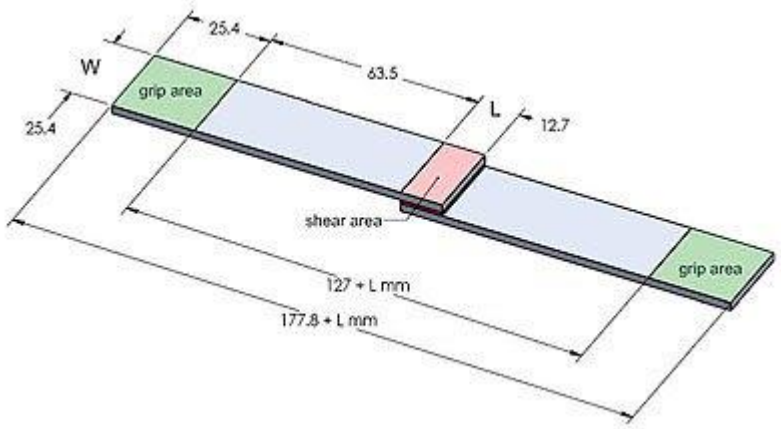

Figure 7.12: Geometry of the adhesive lap shear strength test specimen. (admet.com)

An ASTM D1002 test provides the following measurements:

- Maximum load at failure (N)
- Shear strength at failure (MPa)
- Type of failure (adhesive or cohesive) and percentage

7.3.2. Numerical model definition

A FEM model has been created by means of LS-Dyna® software to simulate the behaviour of the lap joint shear strength test. As can be seen in Figure 7.13, the three dimensional model represents the whole geometry of the sample. Substrate geometry is discretized by means of 4-noded shell elements (ELFORM 10, Belytschko-Wong-Chiang formulation) using an approximate mesh size of 4mm, which creates five elements in the thickness direction. Shells thickness is set to 1.62mm.

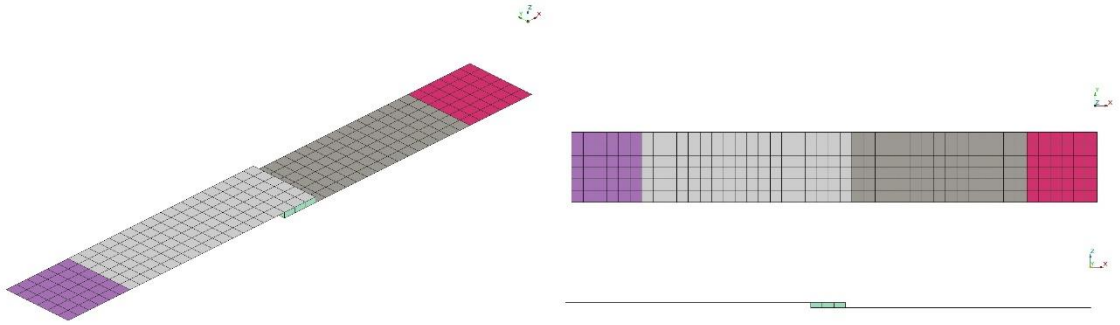

Figure 7.13: FEM model of lap shear strength test specimen used for *MAT252 parameter identification in LS-Dyna®

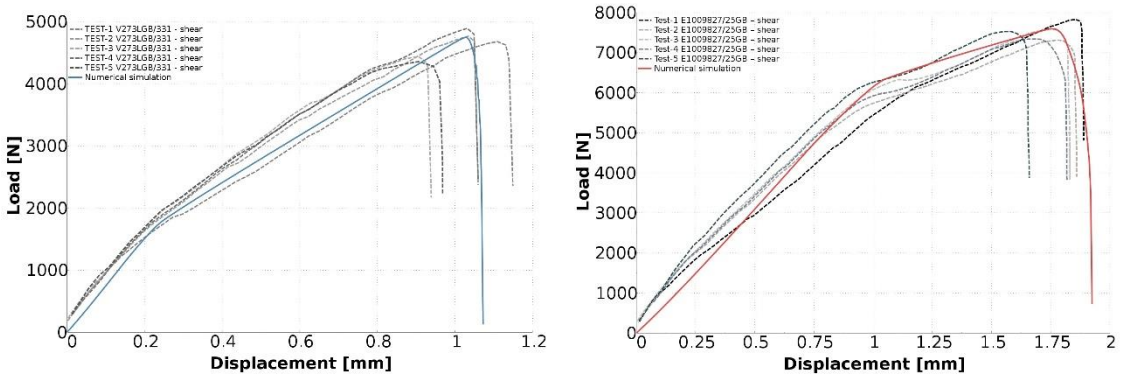

Figure 7.14: Comparison of simulation results with experimental data of the lap shear strength test for two structural adhesives from LORD Corporation, Versilok® V273LGB/331 (left) and E1009827/25GB (right).

In order to represent the two ends of the substrates that are clamped by the testing machine, these surfaces are modelled by means of *MAT20 MAT_RIGID material so they behave as rigid bodies, neglecting any elastic effects that might appear in them. All the degrees of freedom in the nodes of the fixed end are constrained, while only displacement along x-axis is released in the opposite end to simulate the movement imposed by the testing machine. Such constant, quasi-static displacement is set in one of the nodes of the ridig body. Regarding the substrate that deforms elastically, it is characterized with the material model *MAT24 MAT_PIECEWISE_LINEAR_PLASTICITY, setting its corresponding elastic modulus and Poisson's ratio, and making use of the yield strength of the material so the substrate behaves in a perfectly elastic way during the whole simulation.

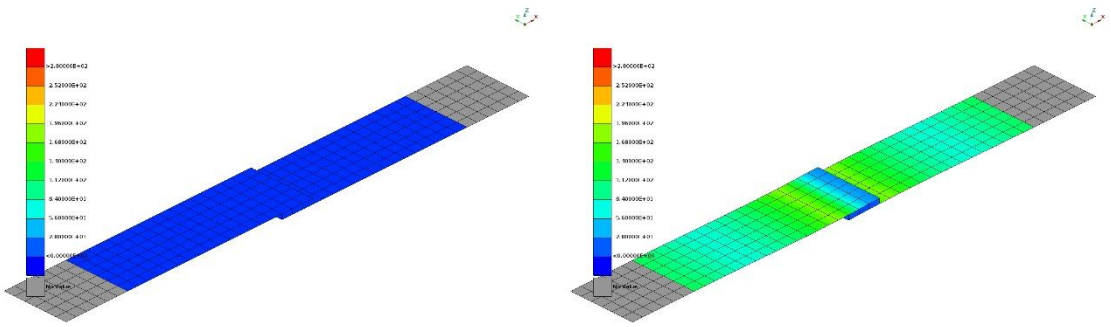

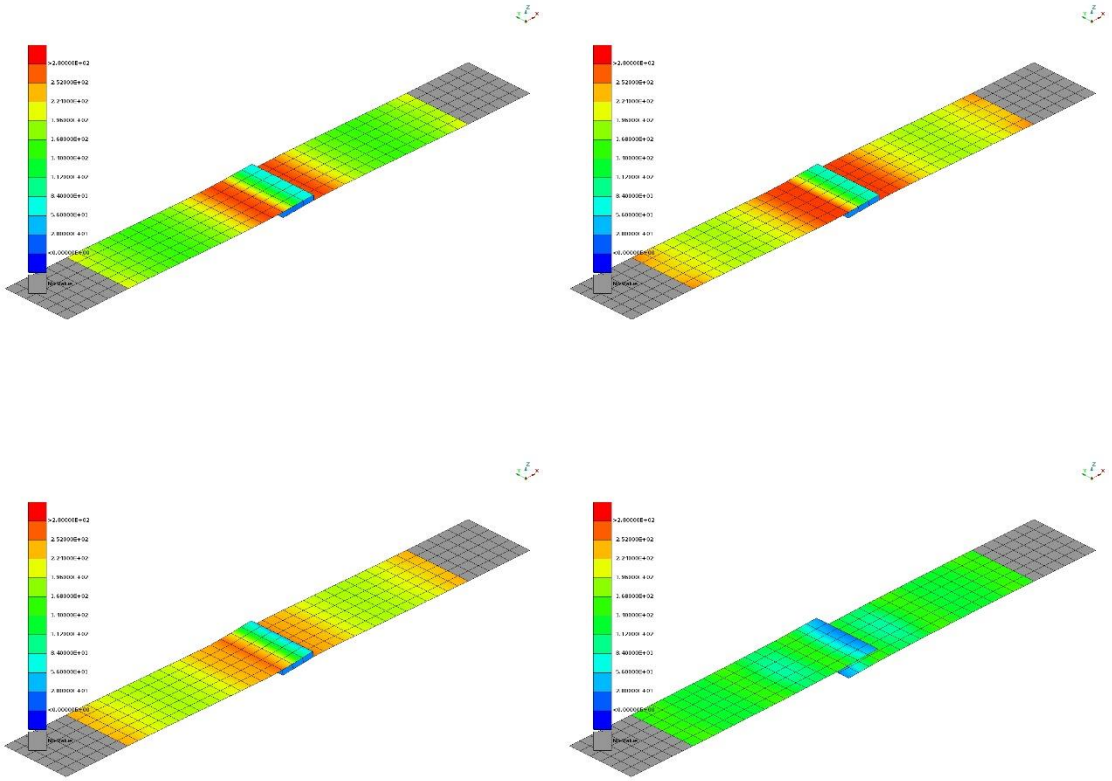

Figure 7.15: Contour plot of Von Mises stresses on the substrate during different stages of the simulation of a lap shear strength test.

As it is usual in this work, adhesive layer is discretized using cohesive elements (ELFORM 20) with offsets to be used with shells, with a 4mm mesh size. As it was explained in section 6, this element formulation requires the *MAT_ADD_COHESIVE option to be added in order to use the *MAT252 TOUGHENED_ADHESIVE_POLYMERE_MODEL with it. Each surface of the cohesive layer is in contact with the opposite substrate surface by means of a TIED contact, in which the adherend behaves as the master part and the adhesive behaves as the slave part. Attention must be paid to the search distance of the contact in order to capture only the right nodes of the slave part. Even though the two elastic substrates are characterized by the same material, they are divided into two parts since this facilitates the contact definition.

A database cross section is created in a transverse line on the elastic part next to the moving rigid body in order to evaluate the applied load.

7.3.3. Simulation results

The experimental data available in this case corresponds to two different structural adhesives from LORD Corporation – Versilok® V273LGB/331 and E1009827/25GB – using two plates of aluminum 6061-T6 as substrates. Figure 7.14 shows a comparison between the experimental data and the simulation results arised from the parameter identification performed using the lap shear and the t-peel – analysed in the next subsection – tests together in order to characterize these two structural adhesives. In both cases it can be observed that, despite the deviation in the experimental curves, specially in the hardening phase, *MAT252 is able to capture accurately the elasto-plastic behaviour of the adhesives, as well as the sudden failure mechanism present under this kind of tests, due to the elevated and homogeneous stress state that the adhesive layer withstands. Behaviour of both structural adhesives is similar, with different values of strength in each case. The characteristic shape of the force versus displacement curve in both cases could be adapted by a bi-linear formulation since no evident change in the slope appears between elastic and plastic regimes. Both yield strength and damage thresholds are accurately captured by the model.

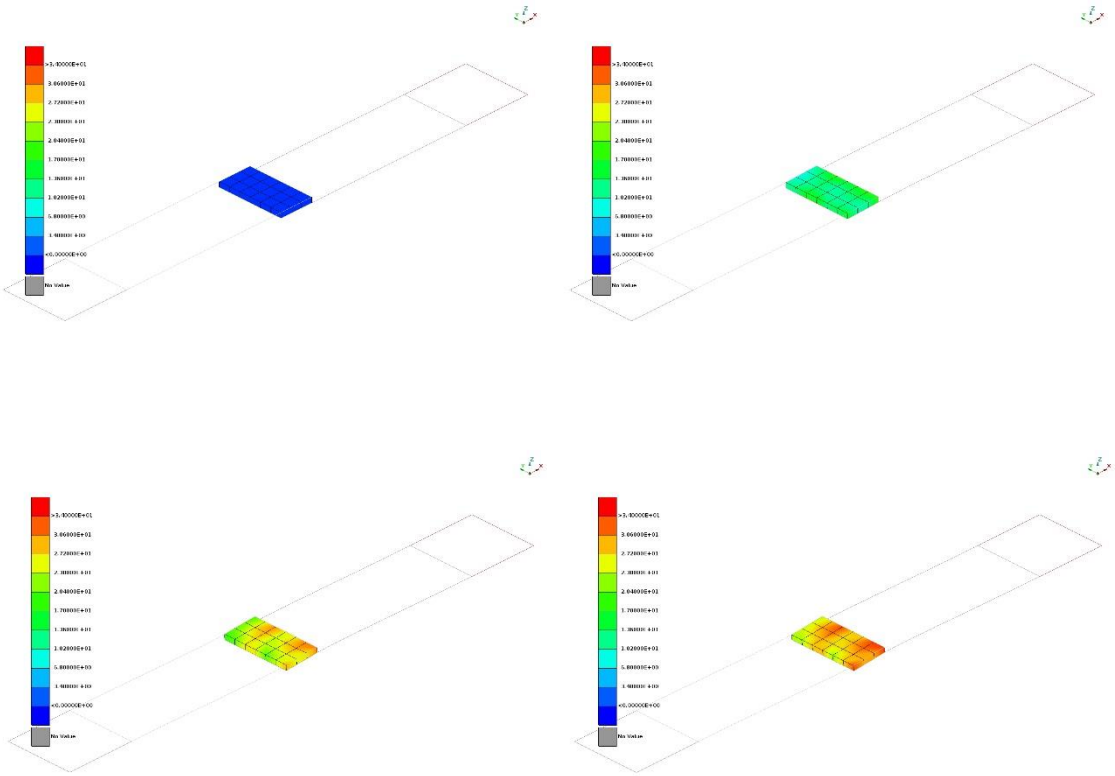

Figure 7.16: Contour plot of Von Mises stresses on the adhesive during different stages of the simulation of a lap shear strength test.

In addition, images of the evolution of the deformed geometry during test execution are shown in Figure 7.15 and Figure 7.16. In them, the homogeneous stress state that the adhesive layer withstands and the sudden and complete failure of the joint can be observed. Stress values of 280MPa appear in the aluminum substrate, which lies directly in its plastic deformation range.

7.4. T-peel resistance test

7.4.1. Experimental setup

The T-peel test (standarized as ASTM D1876) evaluates the force required to progressively separate two bonded, flexible adherends. This test method is primarily intended for determining the relative peel resistance of adhesive bonds between flexible adherends by means of a T-type specimen using a tension testing machine. The bent, unbonded ends of the test specimen shall be clamped in the test grips of the tension testing machine and a load of a constant head speed shall be applied. Variations in test specimen preparation such adhesive curing, adhesive thickness, adherends and conditioning provides insight for optimization in processes and application.

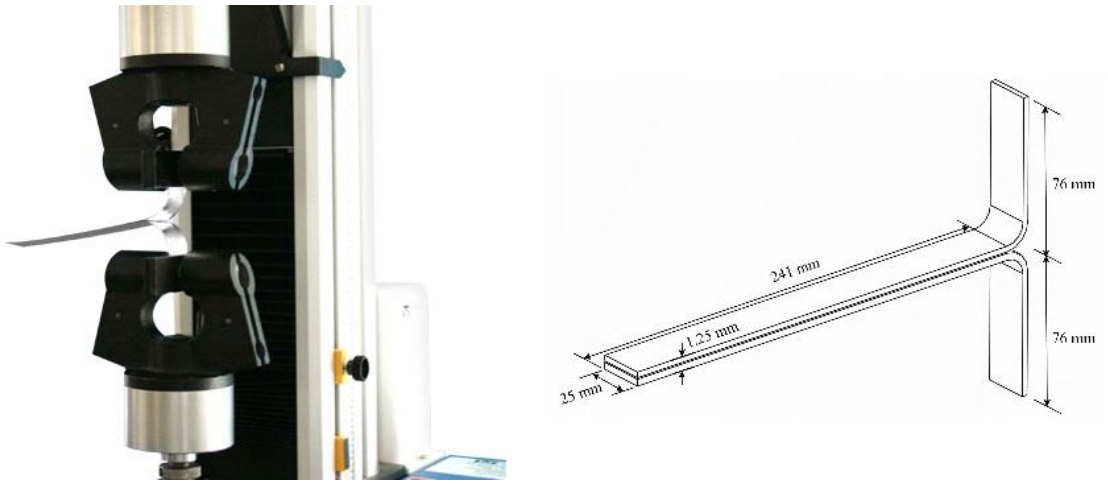

Figure 7.17: Side view of the adhesive t-peel resistance testing device and geometrical details of the test specimen. (admet.com)

Specimens are cut from a T-peel panel to 25.4 mm (1'') long x 300 mm (12'') wide. Figure 7.17 shows the experimental setup of a testing sample and the geometrical detail of the strandarized specimen, in which the constructed FEM models has been based.

The following data shall be determined from the t-peel resistance experiment:

- Peel load (N)
- Peel strength (N/mm)

- Type of failure (adhesive or cohesive) and percentage

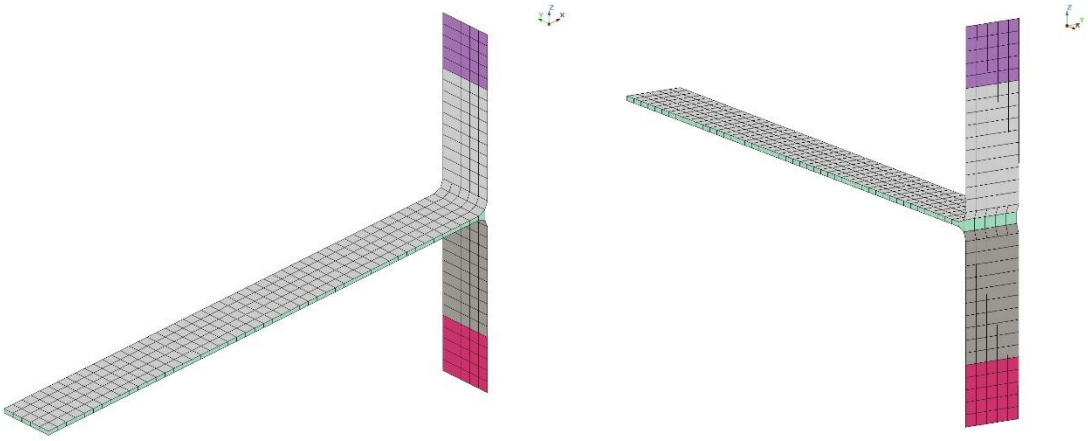

Figure 7.18: FEM model of t-peel test specimen used for *MAT252 parameter identification in LS-Dyna®

7.4.2. Numerical model definition

As it was done in the case of the lap shear strength test, a FEM model has been created in LS-Dyna® to simulate the physical behaviour of a peeling resistance test in order to perform a complete material characterization together with the lap shear strength test specimen. A view of the undeformed geometry can be found in Figure 7.18. Substrate geometry has been again discretized using 4-noded shell elements (ELFORM 10, Belytschko-Wong-Chiang formulation) with an approximate mesh size of 4mm. This allows to represent the curvature of the specimen with enough accuracy so the substrate deformation existent in the experiment can be adequately represented. Again, the areas clamped by the testing machine are represented by using *MAT20 MAT_RIGID that characterize them as rigid bodies. The fixed part has all its displacements and rotations constrained as the moving part only has its displacement along z-axis released. A single point constraint is set on one of the nodes in the latter part in order to set the quasi-static boundary condition of displacement that induces the peeling of the specimen. The elastic parts of the specimen – the parts of the substrate that deform elastically – are characterized by means of the *MAT24 MAT_PIECEWISE_LINEAR_PLASTICITY, setting the corresponding elastic modulus, Poisson's ratio and yield strength of the substrate material.

Again, adhesive layer is discretized using cohesive elements with offsets (ELFORM 20) so these can be used with shells. Mesh size is equivalent to the one of the substrate, and *MAT_ADD_COHESIVE option is added so that *MAT252 material model can be used. A tied contact is defined in order to integrate the adhesive with the substrate, setting the latter as the master part and the adhesive layer as the slave part. Attention must be paid so only the nodes in the adhesived

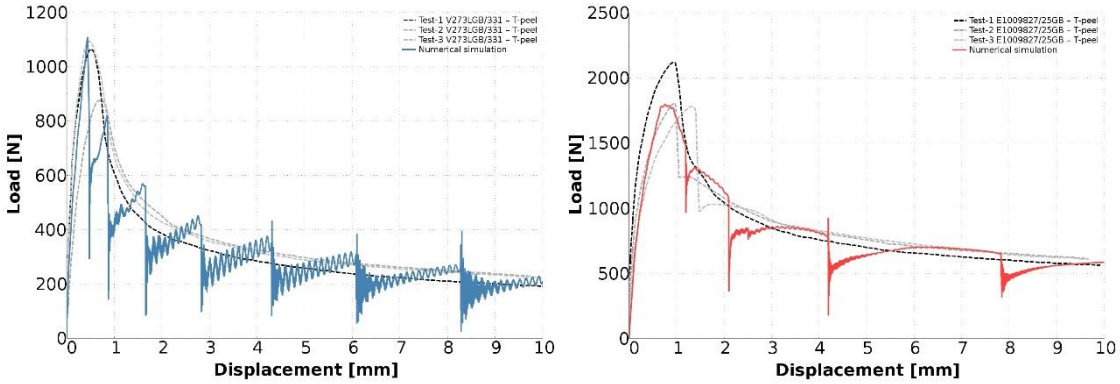

Figure 7.19: Comparison of simulation results with experimental data of the t-peel resistance test for two structural adhesives from LORD Corporation, Versilok® V273LGB/331 (left) and E1009827/25GB (right).

zone are captured by the master part. An adequate search distance is set for the contact and each substrate has its own part to ensure a correct definition of the tie. The filling of the joint at the curved part of the specimen is of vital importance when modelling the adhesive geometry. It is worth mentioning that the adhesive joint must be filled in a 50% of its area so the computed results can be compared to the experimental data. The influence of this fact is later studied by performing simulations using specimens with different filling percentages and comparing them against experimental results.

Finally, force is evaluated by means of a cross section database, defined over a slice of the deformable substrate next to the moving clamped area.

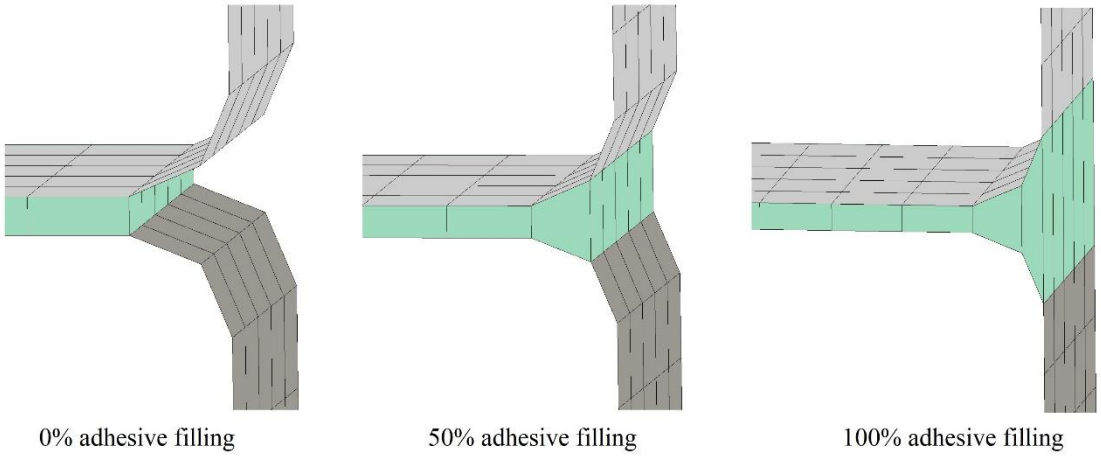

Figure 7.20: Detail view of the FEM model of the t-peel test specimen with three different adhesive fillings

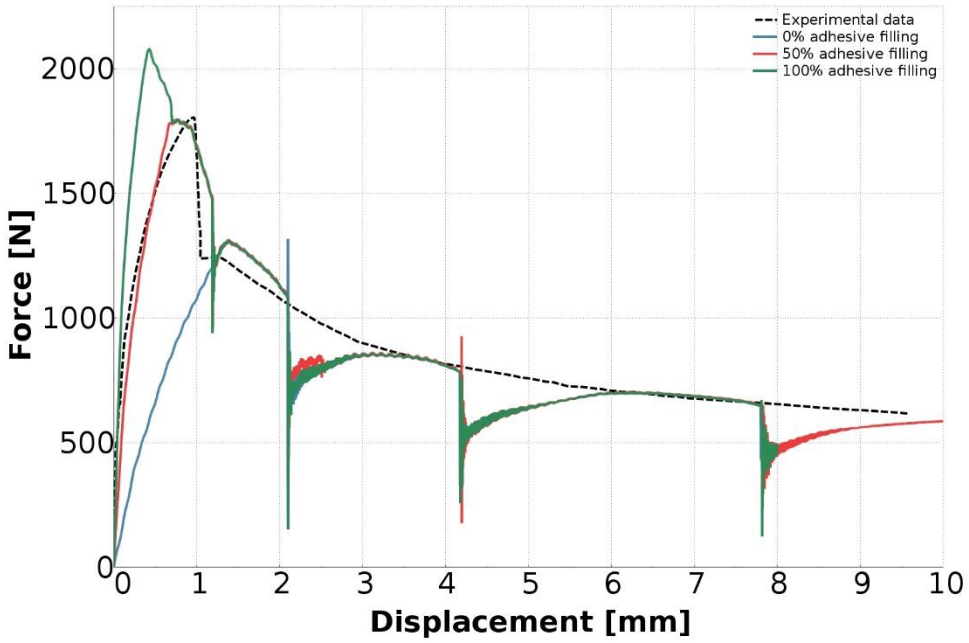

Figure 7.21: Comparison of experimental data with simulation results obtained after performing t-peel resistance tests using three different adhesive fillings.

7.4.3. Simulation results

From a physical point of view, t-peel test presents a complex stress state, adding more information to the previously obtained by means of lap shear strength test and complementing it. Thus, the two tests are used together in order to perform an accurate material characterization. The experimental data corresponds again to two structural adhesives from LORD Corporation – Versilok® V273LGB/331 and E1009827/25GB – using two plates of aluminum 6061-T6 as substrates. As done before, Figure 7.19 shows force-displacement diagrams comparing experimental data and the results of the numerical simulation of the t-peel resistance test peformed over samples of the two structural adhesives. It can be observed that the first peak of strength has been adequately captured by the model, and the damping effect on the load is adequately represented. It can be considered as well that a 4mm discretization of the adhesive layer is able to describe with enough accuracy the peeling process of the sample. There is a notable difference between the strengths reached with this tests compared with the ones obtained under the lap shear strength test. Again, the material model is able to represent this characteristic behaviour of adhesives.

Besides this, there is an important dependency on the filling of the adhesive joint with respect to the reached strength. In this case and as the norm specifies, material characterization has been performed with a 50% filling of the adhesive layer. The strong dependency of the simulation results

with respect to the adhesive filling can be observed in Figure 7.21. There the force versus displacement curves obtained after performing simulations on three t-peel samples with three different adhesive fillings (0%, 50% and 100%) are exposed. There is an evident deviation in the reached adhesive strength, although the effect of the percentage of filling disappears after the curve peak.

The evolution of the deformed geometry of the t-peel sample during the test is shown in Figure 7.22 and Figure 7.23. It can be observed that the characteristic state of stresses of the peel test has been adequately captured by the simulation. There is a progressive and assymptotic loss of strength of the adhesive joint due to the concentrated application of stresses over the load front. The substrate, due to its relatively high stiffness, deforms plastically as the fracture progresses.

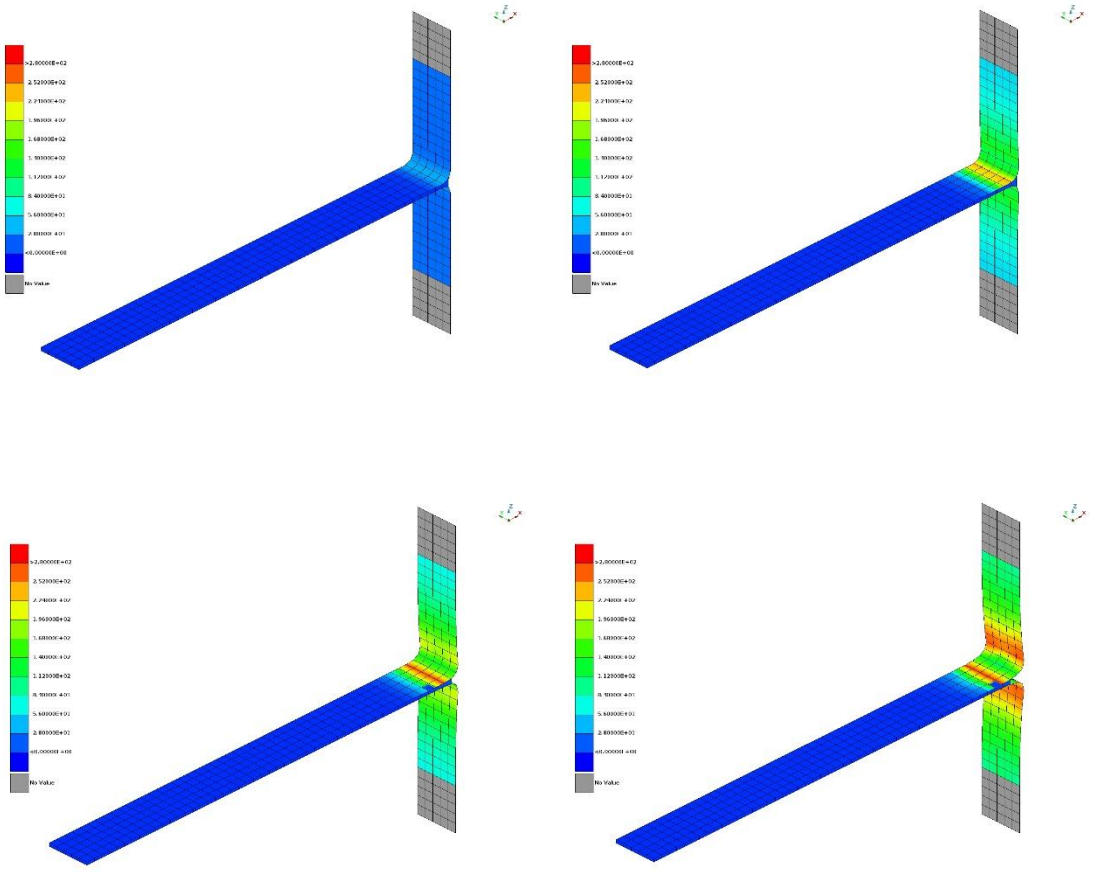

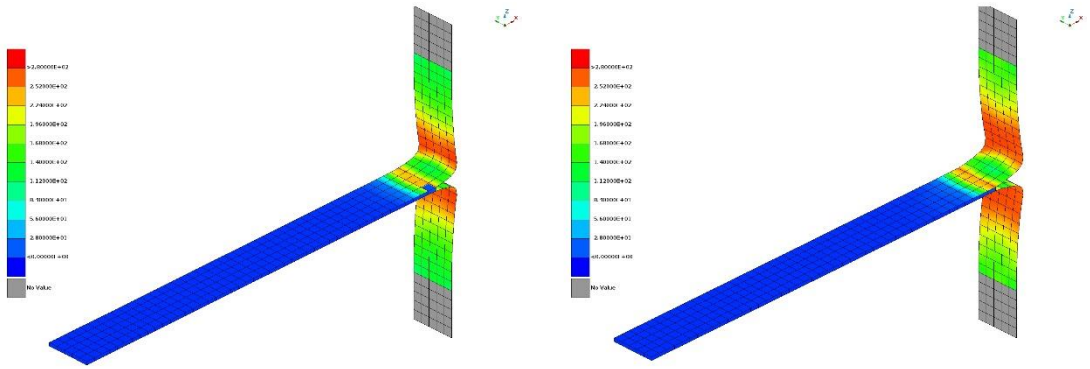

Figure 7.22: Contour plot of Von Mises stresses on the substrate during different stages of the simulation of a t-peel resistance test.

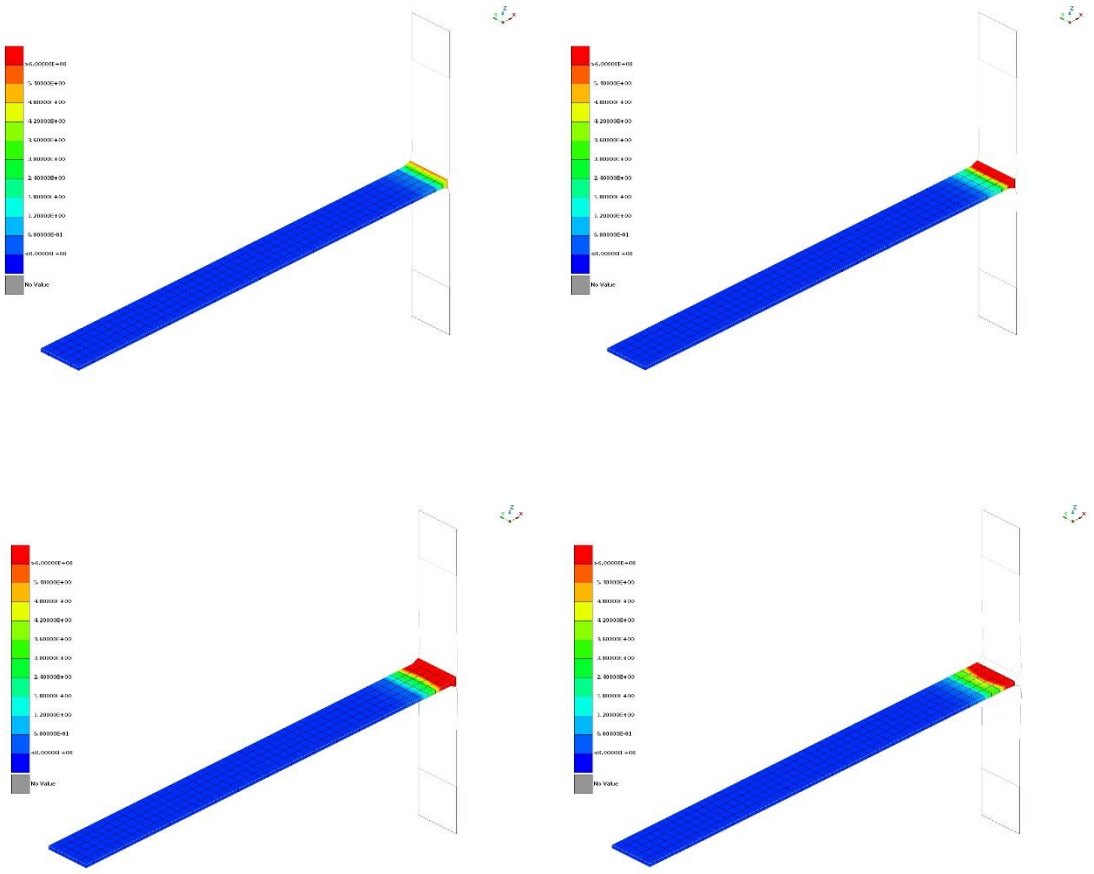

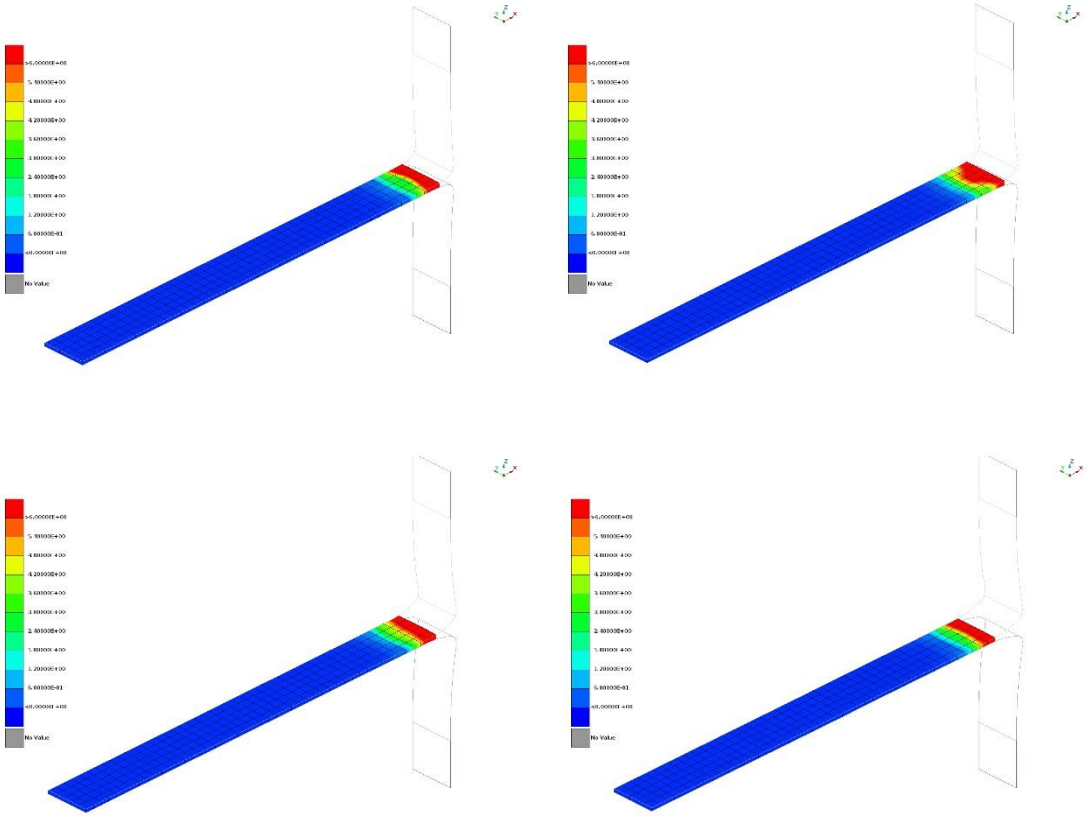

Figure 7.23: Contour plot of Von Mises stresses on the adhesive during different stages of the simulation of a t-peel resistance test.

Chapter 8

Component-Level Models for Validation

This chapter introduces a series of component-level models created in LS- DYNA®, used in order to validate the performance of the proposed methodologies. By means of this, the FEM modelling methodology presented in chapter 6, and the characterization methodologies presented in chapter 7 are evaluated. In the first case, such material model is used to bond the different parts of a beam tested under three-point bending conditions. In the second case, the performance of the material model is studied in a component-level real scenario, as it is used to model the adhesive that attaches a bus roof panel to its structure. In this case, the adhesive joint is subjected to an opening test.

For confidenciality reasons, some details concerning structural design or numerical results present in this chapter have been omitted.

8.1. Three point bending test

In engineering mechanics, flexure or bending characterizes the behaviour of a slender structural element subjected to an external load applied perpendicularly to the longitudinal axis of the element. In automotive framework, this behaviour becomes critical for certain load cases in homologation, as in a bus roll-over or a lateral pole impact in a passenger car. Thus, 3-point bending test is an extended methodology to evaluate new materials for vehicle structures. A flexure test produces tensile stress in the convex side of the specimen and compression stress in the concave side. This creates an area of shear stress along the midline. There are two normalized test types: 3-point and 4-point flexural tests. In a 3-point flexural test a specimen with a constant cross-section is placed on two parallel supporting pins. The loading force is applied in the middle by means of a loading pin. These pins are mounted in a way, allowing their free rotation about an axis parallel to the pin axis, and about an axis parallel to the specimen axis. In this test the area of uniform stress is quite small and concentrated under the center loading point. A schematic view of the test can be seen in Figure 8.1.

The 3-point bending test is a classical experiment in mechanics, used to provide values for the modulus of elasticity in bending, flexural stress, flexural strain and the flexural stress-strain response of the material. Its main advantage is the ease of the specimen preparation and testing. On

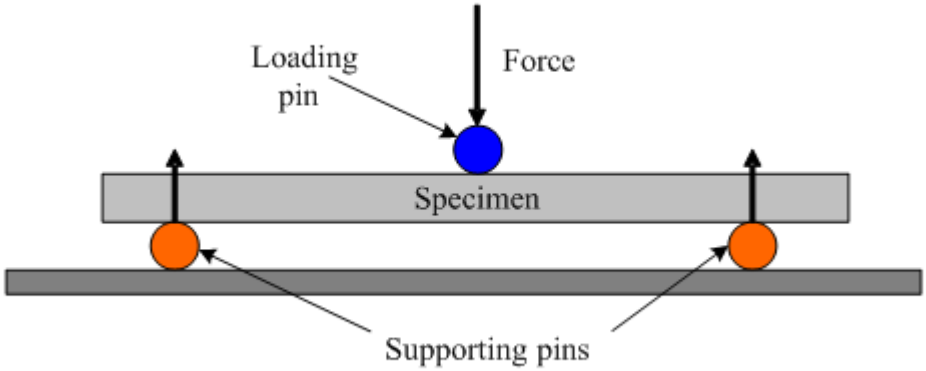

Figure 8.1: Schematic view of the configuration of a 3-point bending test

the other hand, the results of this testing method are sensitive to specimen and loading geometry and strain rate.

In this work, a 3-point bending test is performed on a model representing a composite beam used in an automotive component. As can be seen in Figure 8.2 the body of the beam is divided into two parts, bonded together by means of a structural adhesive layer. These elements, characterized by means of *MAT252 material model, reproduce the physical behaviour of the joint in the FEM model of the studied beam.

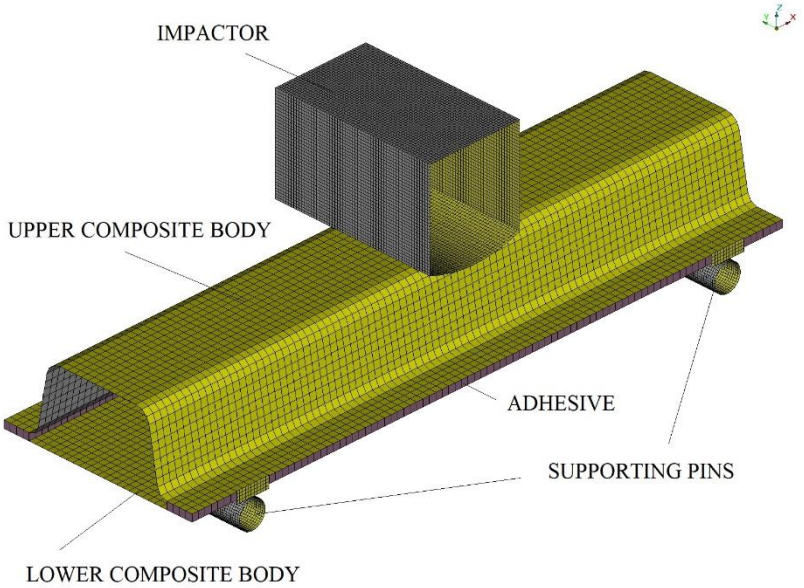

Figure 8.2: FEM geometry of the beam models (model A on the left, model B on the right) to be subjected to 3-point bending tests

This experiment is then used to validate the modelling methodology in an intermediate vehicle component subjected to complex loading and damage mechanisms. As done with substrates before, composite panels have been discretized using 4-noded shell elements, while the adhesive layer has been modelled using 8-noded cohesive elements, connected to each other by means of tied contacts without offsets since both substrate planes are parallel.

The deformed geometry along different steps of the simulation have been captured and represented in Figure 8.3 for the studied beam. They show a progressive deterioration of the composite plies, followed by the subsequent failure of the fibers that transmit an important amount of load to the adhesive layer, that remains damaged but not broken. A remanent strength can be appreciated, caused for the interaction between the crushed parts of the component.

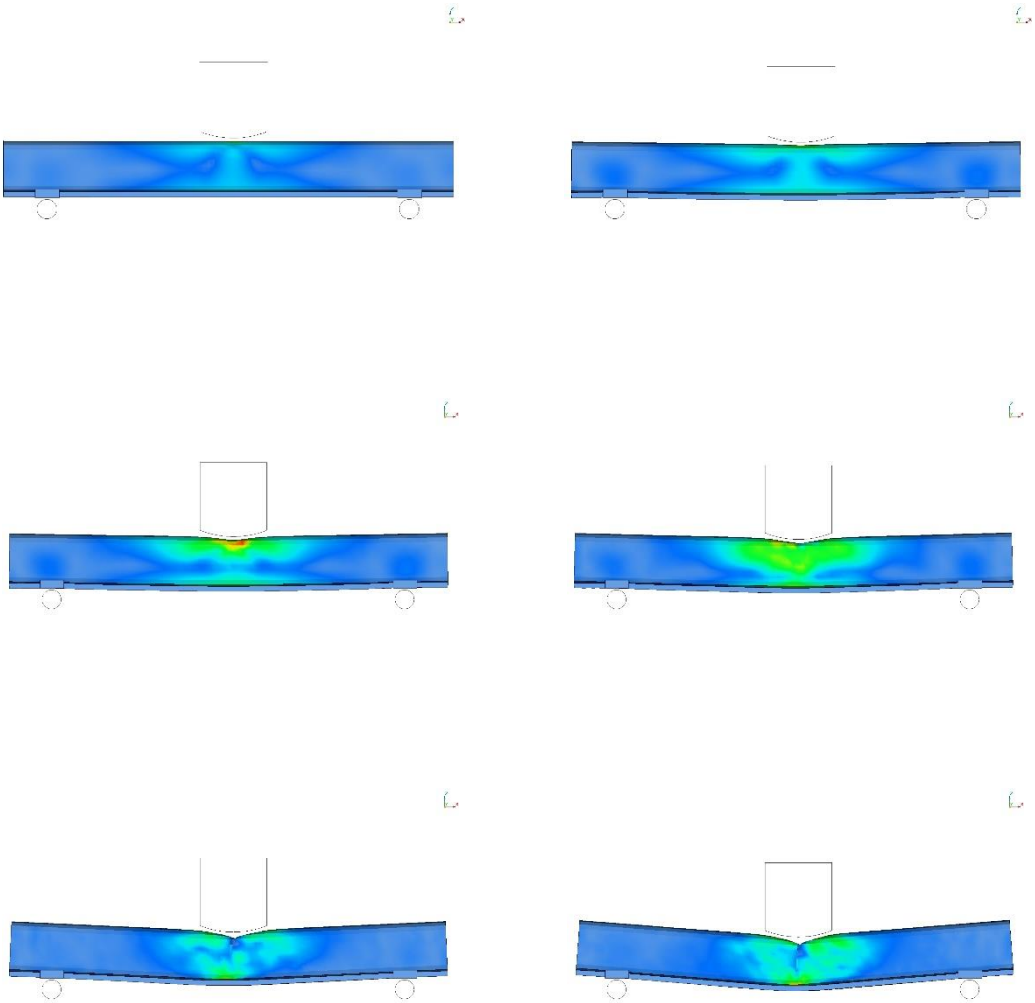

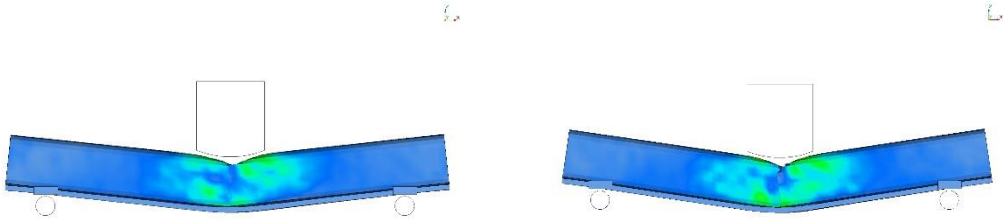

Figure 8.3: Contour plot of Von Mises stresses on a composite beam during different stages of the simulation of a 3-point bending test

Finally, in Figure 8.4 the force versus displacement curve obtained from the simulations performed on the beam model is compared with the available experimental data. The loading part of the curve is adequately captured. A lack of correlation can be observed on the reached strength and on the remanent force after the peak of the curve, which takes place because of the collapse of the composite body. This collapse usually leads to a complicated scenario in terms of interactions between the broken elements, which is not inside the scope of the present work. The *MAT252 together with the proposed modelling guidelines form a numerically stable, computationally efficient way of simulating the physical behaviour of structural adhesives under complex stress states as the one introduced above.

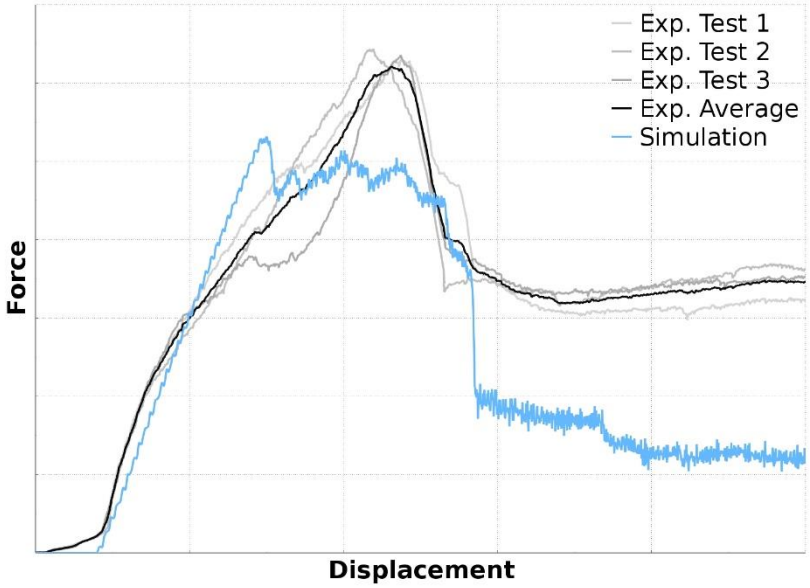

Figure 8.4: Comparison of simulation results with experimental data for a 3-point bending test performed on an adhesively bonded composite beam sample

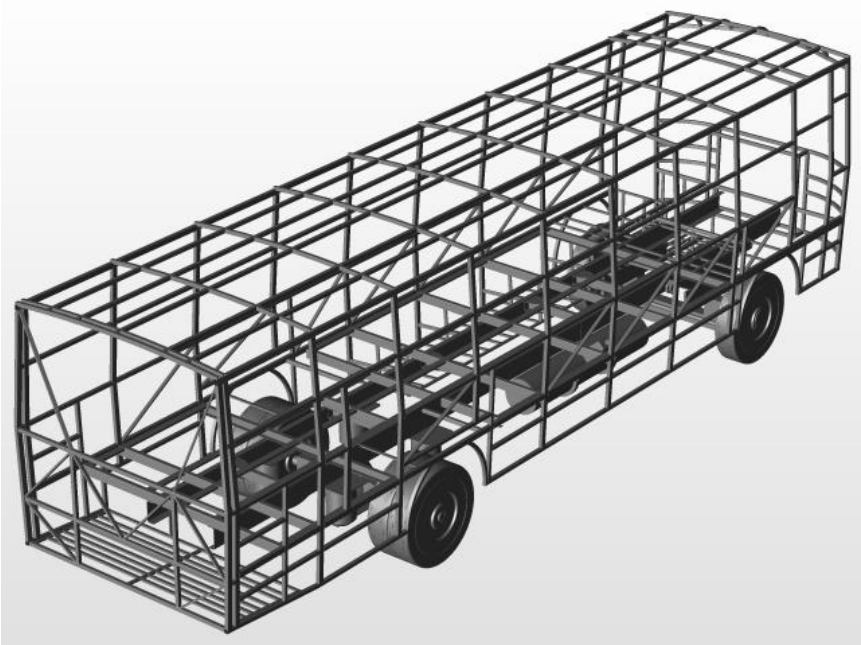

Figure 8.5: Generic CAD design of a bus body structure (grabcad.com)

8.2. Practical case: bus rooftop opening test

8.2.1. Motivation

In the following section a real, practical case involving the use of adhesive bonds is presented. In this study, the physical behaviour of a joint – combination of structural adhesive and rivets – that forms part of a bus rooftop is analysed. This analysis has been part of the homologation process of a bus structure, similar to the one exposed in Figure 8.5. One of the key aspects of these processes is to check the response of the bus structure under a roll-over situation. The body structure is validated if is capable to resist the imposed stresses in such a way that the resultant deformations do not invade a predefined survival space, inside which the passengers would not result seriously injuried. Figure 8.6 combines real images and schematic details of bus roll-over tests in order to contribute to the understanding of the presented study.

It is worth to mention that roll-over homologation in buses is a discipline that can be surpassed by means of simulation only. Experimental tests are not required if verified simulation methodologies are used. In the case of study in this section, but, composite roof and adhesived joints were introduced. These materials are not included in the current verified simulation methodologies. Thus, the critical points of the bus structure (as the bonding between roof and structure) were tested in subsystem tests. Finally, when the critical zones were evaluated and improved to reduce risk of injuries in case of accident, the bus was able to be homologated.

The traditional manner of modelling structural adhesives is to consider them as purely elastic materials. This simplification may induce numerical instabilities and lead to inaccurate results under certain complicated stress states, as is the case here. Thus, it became necessary to apply the acquired knowledge in adhesive modelling in order to obtain a stable, precise simulation of the bus rooftop deformation. Throughout the next sections the followed modelling procedure and the obtained results are presented.

8.2.2. Procedure

The LS-Dyna® *MAT252 material model, together with the modelling methodologies proposed in this work, have been applied to bus rooftop opening tests in order to characterize the behaviour of two joints made of structural adhesive and rivets. After the stabilization and an adequate correlation of the numerical simulations with the experimental data, the obtained model is ready to be applied in the further development process of the bus structure.

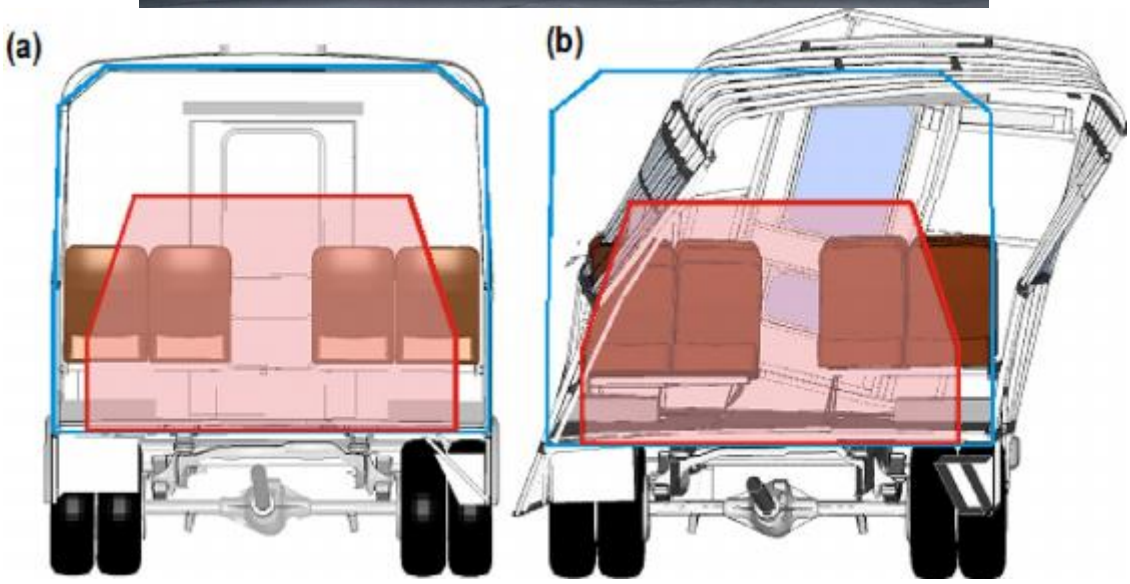

Figure 8.6: From top to bottom, a complete bus body subjected to a roll-over test (toyota.com); undeformed and deformed geometries of a bus body roll-over simulation where survival space is marked in red (Bojanowski & Kwasniewski, 2013); deformed structure after a experimental roll-over test (Dell, Amies & Williams, 2008)

An opening test is intended to recreate the behaviour of the joint between the components of a bus rooftop – essentially composed of a sandwich panel and a longitudinal cantrail – subjected to a roll-over scenario. This in essence provokes a torsional effect on the joint that would try to detach the two mentioned components from each other. A perspective view of the FEM geometry of the rooftop component can be observed in Figure 8.7 and a schematic view of the functioning of an opening test is exposed in Figure 8.8.

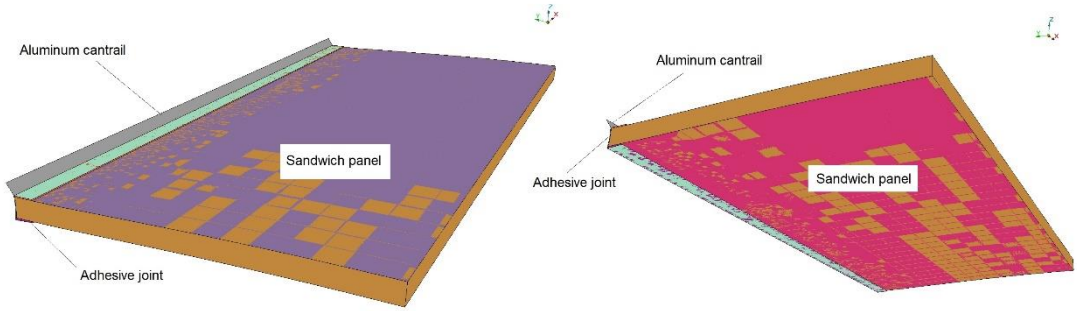

Figure 8.7: Upper and lower simplified perspective views of the FEM geometry of the studied bus rooftop

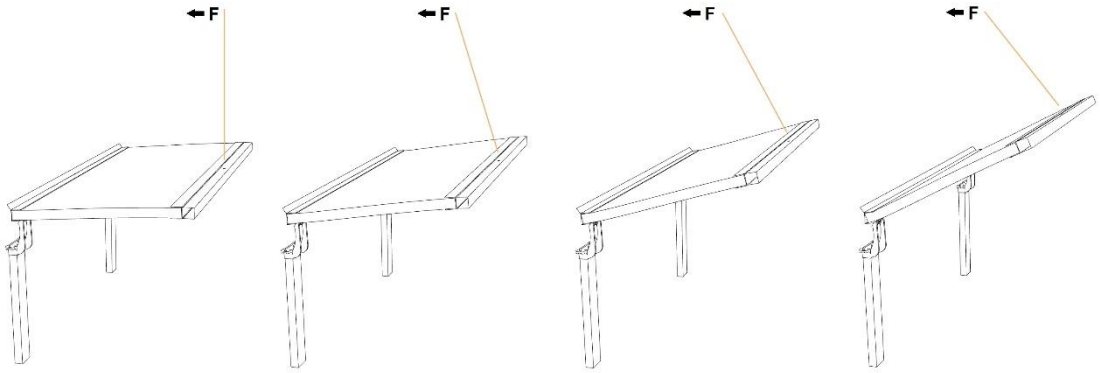

Figure 8.8: Schematic view of the evolution of a rooftop opening test under a pulling force F

As can be seen, the component object of the present study presents a great complexity regarding its geometry and stress state. The joint characterization process has been performed in two stages using two different rooftop configurations.

In first place, the physical behavior of an adhesively bonded joint that connects a fiber glass sandwich panel with an aluminum cantrail has been characterized. This has been done by correlating the simulation results with the data arising from a experimental test – so-called test A from here on – performed on an equivalent rooftop sample.

Secondly, the riveted joints are characterized using the results obtained in an experimental test performed on a rooftop sample with a different configuration – test B in this case – which includes, among other modifications with respect to test A, a series of rivets that joins the sandwich panel and the cantrail together. These element work in combination with the previously studied structural adhesive. Rivets are modelled in LS-Dyna® by means of the *CONSTRAINED_SPR2 constraint, which defines a self-piercing rivet with failure. The algorithm does a normal projection from each of the nodes from a set representing the location of the rivets, to two previously defined master and slave surfaces, that represent the sheets to be fastened.

8.2.3. Results

Figure 8.9 shows the evolution of the FEM geometry that can be compared to an image of the experimental test performed on model A rooftop sample, shown in Figure 8.11. In them, it can be observed that the simulation accomplishes a great degree of similitude with respect to the reality, accurately capturing the progressive failure of the adhesive layers. This is caused by the rotation of the sandwich panel around a theoretical axis located at its upper-left corner that makes the roof try to slip from the cavity of the cantrail. These relative displacements translate into the onset of different stress modes on the adhesive layers that hold the structure together.

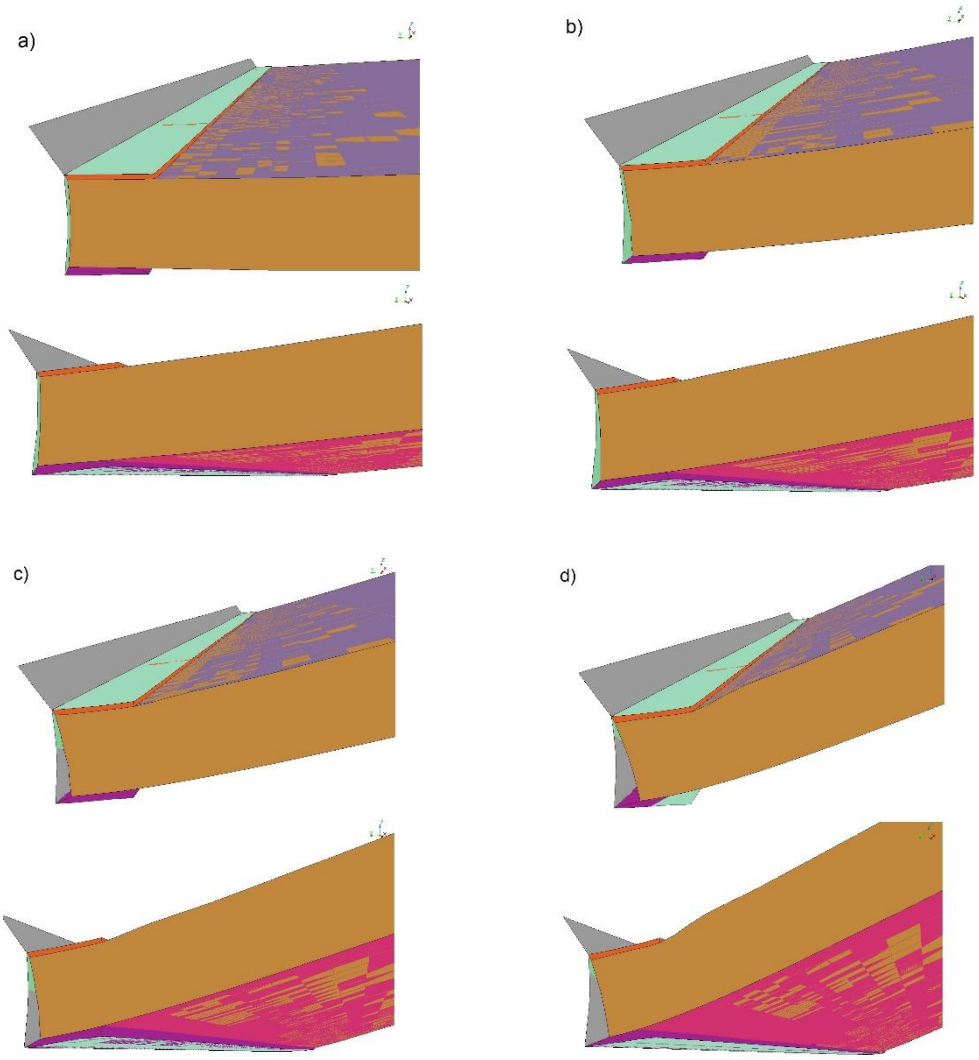

Figure 8.9: Upper and lower perspective views of different moments during the FEM simulation of the model A rooftop opening test

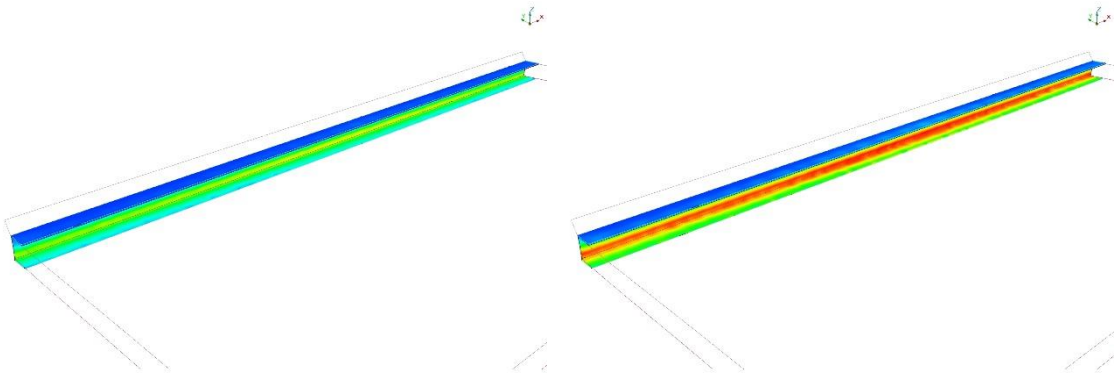

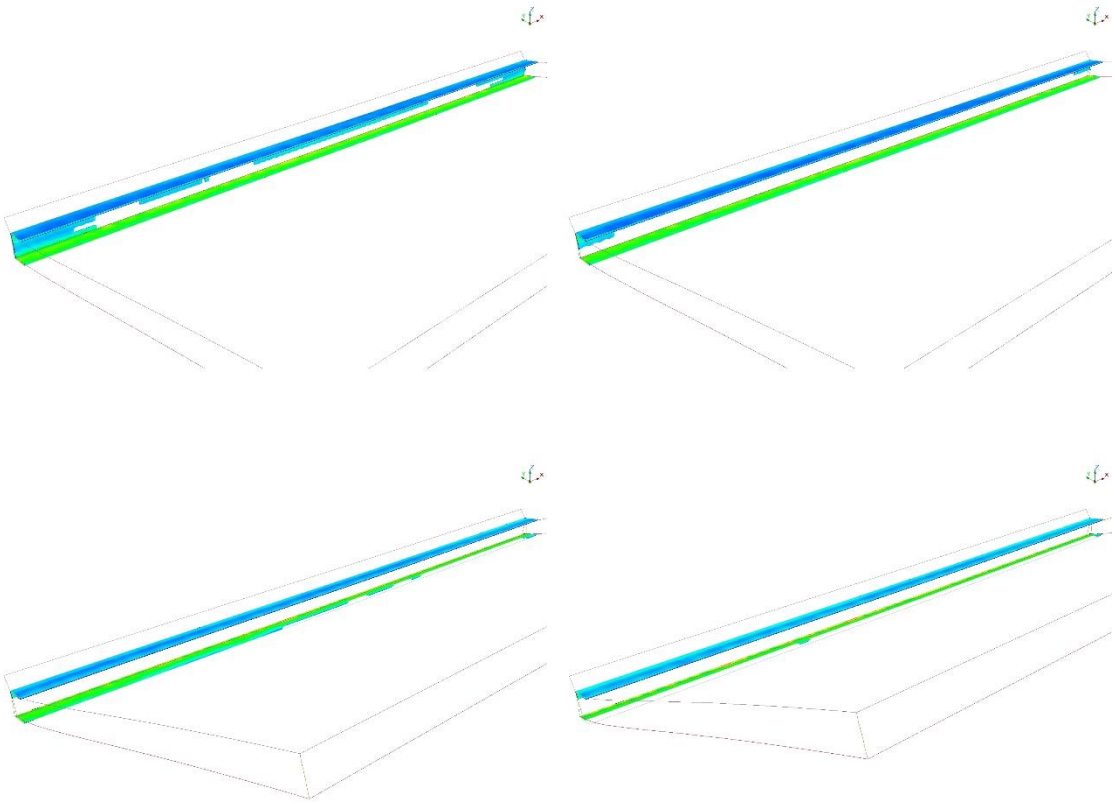

Figure 8.10: Contour plot of stresses during the evolution of the simulation of a rooftop opening test performed on model A

The vertical adhesive layer is the one that fails first, due to a peel stress state that provokes the rapid emergence of higher solicitations compared to the ones that appear on the lower layer, that

Figure 8.11: State of the adhesive layer after failure during experimental tests performed on model A (left) and model B (right)

are of a pure shear nature. As can been seen in this work, the adhesive strength under peel stress is lower than under shear stress, so the sandwich panel is released from this attachment. After that, the lower adhesive layer is the one that holds the panel inside the cantrail. On the contrary, the upper layer barely works during the test. The evolution of stresses and the failure process of the adhesive during the simulation can be seen in Figure 8.10.

The second tested configuration – model B – consists of a combination of rivets and structural adhesive that, apart from certain changes in other design details, are introduced in order to increase the strength of the component under an opening test. As done in the case of the model A, different stages of the deformed structure are shown in Figure 8.12, and the evolution of stresses of the adhesive layers are exposed in Figure 8.13. In them, the effect of the rivets can be observed, as they absorb a significant part of the stresses provoked by the relative displacement of the sandwich panel.

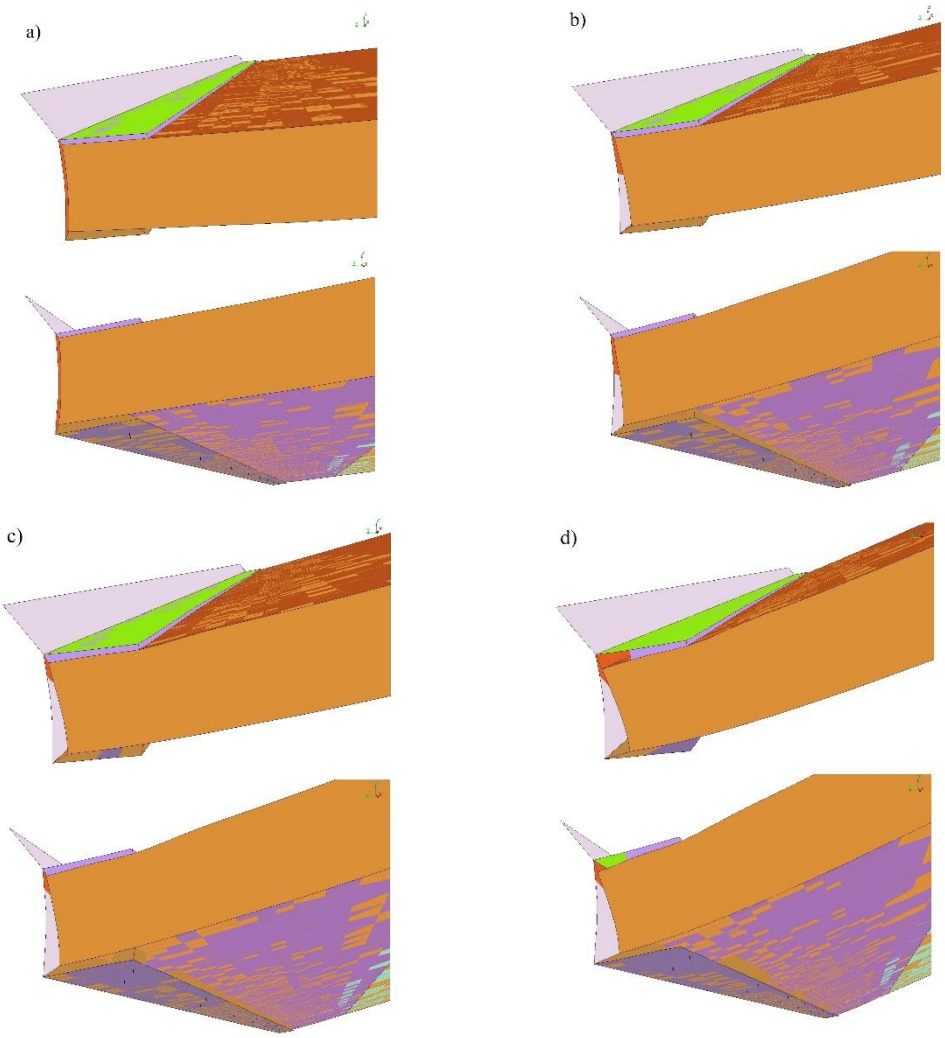

Figure 8.12: Upper and lower perspective views of different moments during the FEM simulation of the model B rooftop opening test

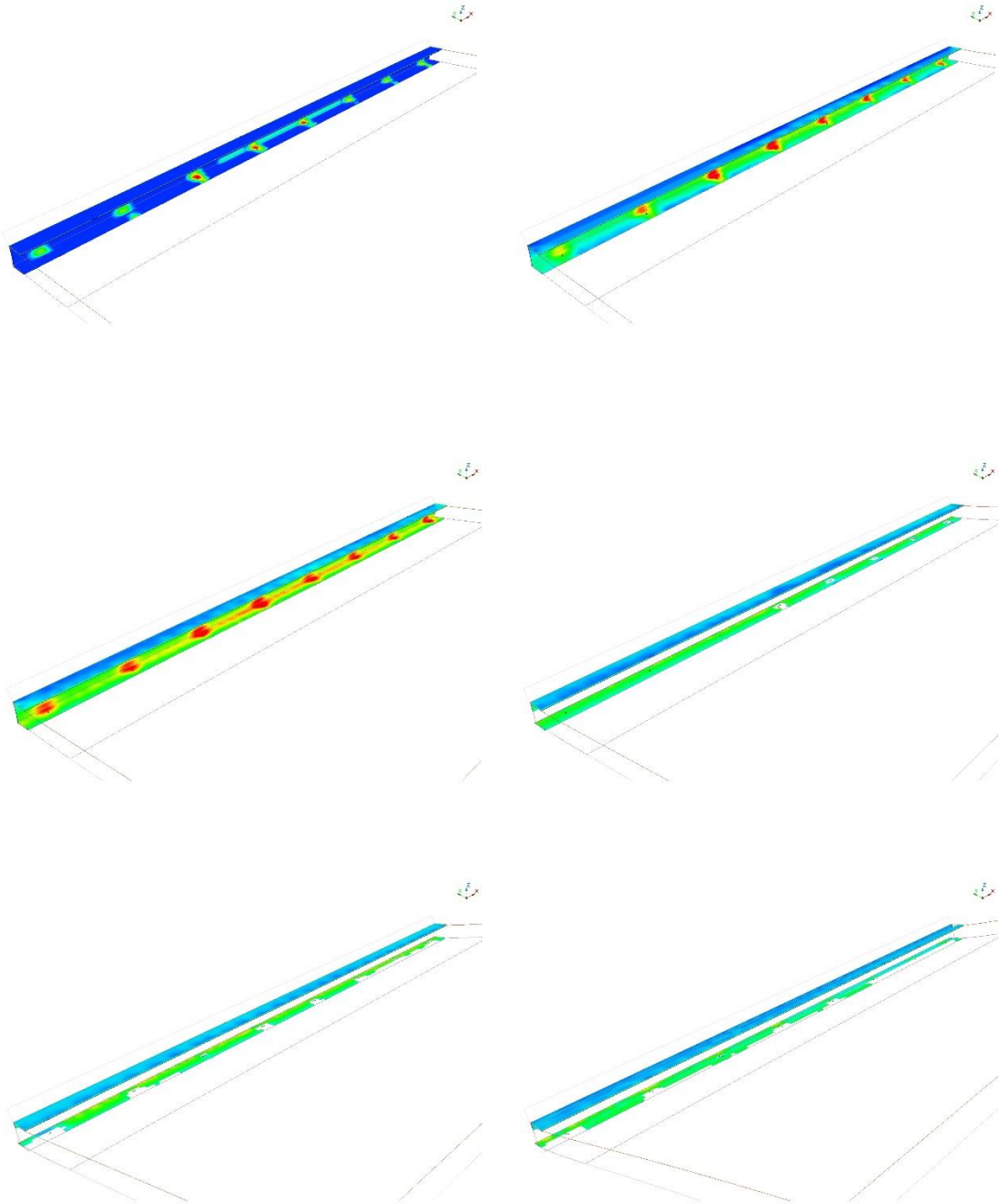

Figure 8.13: Contour plot of stresses during the evolution of the simulation of a rooftop opening test performed on model B

Finally, the load versus displacement curves exposed in Figure 8.14 show the correlation of the simulation results with the experimental data for the two tested configurations. Both the loading parts and the reached strength during the test are accurately captured. The mechanical fastening in model B increase the strength of the component with respect to the model A, where the joint is performed only by means of a structural adhesive. After failure as it is obvious, a large and diverse number of parts of the component come into contact, which makes the correlation to be extremely difficult. Besides, the failure of the rooftop is not considered in a roll-over situation so this situation would lie out of the scope of the present study.

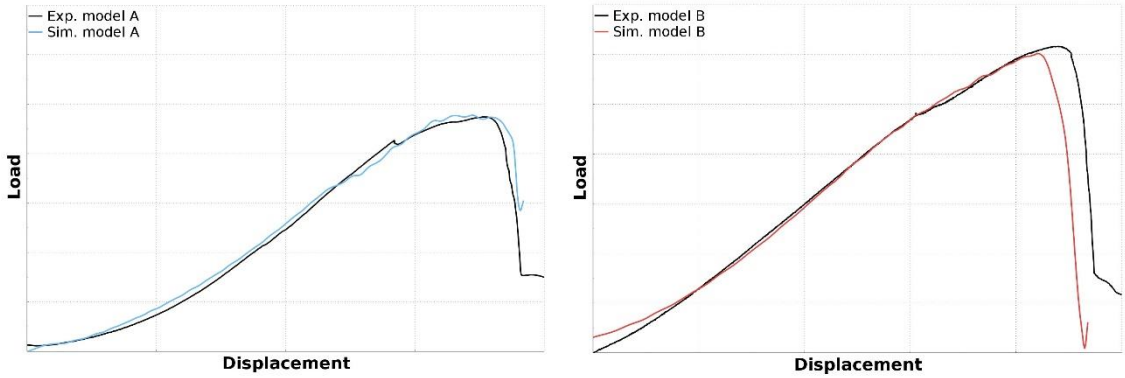

Figure 8.14: Comparison of results obtained from roof opening tests performed on models A and B

Chapter 9

Conclusions and Further Lines of Work

9.1. Conclusions

Multi-material designs and the growing use of lightweight materials are a constant in the development process of new components in the automotive industry. On the other hand, the use of numerical methods in the research and engineering of these innovative components makes possible to constantly evolve safety, performance and durability standards. In this sense, the use of structural adhesives at the expense of traditional methods as a bonding mechanism between components makes the correct definition and characterization of these materials to be fundamental.

The objective of this work was the development of a technique to characterize the physical behaviour of structural adhesives in order to obtain stable and reliable numerical simulations involving adhesive joints. To that end, LS-Dyna® material model TOUGHENED-ADHESIVE-POLYMERE-MODEL (*MAT252) has been used, specifically developed to represent the mechanical behaviour of crash optimized high-strength adhesives under combined shear and tensile loading.

After a brief review about structural adhesives technology and an overview of the Finite Element Method, the *MAT252 material model was introduced by means of a description of its constitutive equations together with a series of modelling guidelines, such as the use of cohesive elements for the modelling of adhesive layers and tied contacts for their connection with the substrates. Then, a series of tests in order to accomplish a proper characterization were described: the butt-bonded hollow cylinder (according to DIN EN 14869-1), the KS2 specimen, the lap joint shear strength test (ASTM D1002) and the t-peel resistance test (ASTM D1876). These specimen tests have the ability of creating homogeneous stress states on the adhesive layer that allows to numerically represent its physical behaviour.

Finally, the numerical performance of the *MAT252 material model and the proposed modelling technique was validated by means of its implementation in component-level models. Simulation of 3-point bending tests of two adhesively bonded beams were conducted and a practical case involving a real bus component was presented, where the detachment of an adhesively bonded roof panel was studied.

Adhesive bonds have been traditionally a source of numerical instability in vehicle crash simulations, due to their complex physical behaviour and their different failure modes depending on the loading conditions. In pursuit of numerical stability, purely elastic representation of adhesive bonds leads to usually imprecise and sometimes wrong results. After an adequate experimental data collection, the use of any of the test specimens presented in chapter 7 is a simple, straightforward procedure for the numerical characterization of any structural adhesive.

Besides, as shown through the validation process presented in chapter 8, the numerical representation of structural adhesive bonds by means of the FEM modelling guidelines presented in this work provides stable and accurate calculations, eliminating possible sources of error from component or full vehicle crash simulations. Models are not needed to be corrected and relaunched anymore due to error terminations coming from adhesive unstabilization, speeding up the preprocessing phase, facilitating and optimizing in general terms the tasks of the CAE engineer.

9.2. Further lines of work

Although the current methodology allows to perform a stable and accurate numerical simulation of the behaviour of adhesive bonding, there is still much room for improvement. There exist a series of lines of work to be followed in the future in order to enhance and enrich the knowledge about adhesive bonding behaviour in automotive components:

- The construction of more validation models that generate additional complex stress states would allow a deeper understanding of the material behaviour and a more precise characterization. In particular, whole vehicle crash simulations would be specially useful in order to determine the performance of the proposed methodology in terms of accuracy and also of computational cost.

- The presented methodology allows the characterization of structural adhesives under quasi-static loading, where inertial effect are negligible. However, TOUGHENED-ADHESIVE-POLYMERE-MODEL (*MAT252) permits the consideration of strain rate effects. Efforts in that regard would enable the simulation of the physical behaviour of adhesive bonds under dynamic loading.

- Parameter identification process from test specimens introduced in chapter 7 was entirely performed by an analyst on the basis of collected experimental data and its own expertise. The utilization of LS-OPT® software allows an automatic material parameter calibration that returns accurate results in a shorter period of time.

- The use of structural adhesives in the automotive industry is fully linked to the increase in the use of composite materials (fibreglass, CFRP...) as a fundamental part of future vehicle designs. The stabilization and improvement of adhesive simulation therefore means an increase in the possibilities in the modelling of this type of innovative, groundbreaking materials.

- In line with the above, performance of an adhesive bond strongly depends on the interconnected substrates. Research on adhesives characterization when different substrates are tied together – specially carbon fibre composites – is a pending and challenging work line in the automotive industry.

References

Bihamta, R. (2017). Modeling Adhesive Joints in the Automotive Industry. Developments, Challenges and Future. *New Methodologies for Modeling, Simulation and Testing Automotive Lightweight Materials*.

Burbulla, F. (2015). *Kontinuumsmechanische und bruchmechanische Modelle für Werkstoffverbunde.* Kassel University Press.

Burbulla, F., & Matzenmiller, A. (2011). Constitutive modelling of adhesively bonded joints. *PAMM, Proceedings in Applied Mathematics and Mechanics*.

Burbulla, F., Matzenmiller, A., & Kroll, U. (2015). Modelling of Adhesively Bonded Joints with *MAT252 and *MAT_ADD_COHESIVE for Practical Applications. *10th European LS-DYNA Conference*.

Camanho, P., Dávila, C., & de Moura, M. (2003). Numerical Simulation of Mixed-mode Progressive Delamination in Composite Materials. *Journal of Composite Materials*.

Clarke, M., Buckley, M., Broughton, J., & Hutchinson, A. (2009). Characterisation and Simulation of Structural Adhesives. *7th European LS-DYNA Conference*.

da Silva, L., & Campilho, R. (2012). *Advances in Numerical Modelling of Adhesive Joints.* Springer.

Dillard, D. (2009). Design of Adhesive Bonds: An Introduction. *The Adhesive and Sealant Council, Inc.*

Droste, A., Mirdamadi, M., Wang, D., & Vogel, G. (2014). CAE from a material suppliers point of view. *DYNAmore Forum*.

Feucht, M., Haufe, A., & Pietsch, G. (2007). Modelling of Adhesive Bonding in Crash Simulation. *LS-DYNA Anwenderforum*.

Gao, X., Zhang, T., Zhou, J., Graham, S., Hayden, M., & Roe, C. (2010). On stress-state dependent plasticity modeling: Significance of the hydrostatic stress, the third invariant of stress deviator and the non-associated flow rule. *International Journal of Plasticity*.

Gerlach, S., Fiolka, M., & Matzenmiller, A. (2005). Modelling and analysis of adhesively bonded joints with interace elements for crash analysis. *LS-DYNA Forum*.

Ghassemi-Armaki, H., Khan, Q., Singh Gill, A., & Zilincik, S. (2017). Characterization and Modeling of Spot-Weld Joints in Press Hardening Steels Associated with Softening in Heat Affected Zone. *11th European LS-DYNA Conference*.

Graf, T., Haufe, A., & Andrade, F. (s.f.). *Adhesives modeling with LS-DYNA: Recent developments and future work.* Stuttgart: DYNAmore GmbH.

Haufe, A., & Pietsch, G. (2009). Spotweld and Failure Modelling in Crashworthiness Applications with LS-DYNA. *Eksen Engineering Users Conference*.

Haufe, A., Pietsch, G., Feucht, M., & Kolling, S. (2007). FE-Modeling of Spotwelds and Adhesive Joining for Crashworthiness Analysis. *6th European LS-DYNA Users' Conference*.

Haufe, A., Pietsch, G., Graf, T., & Feucht, M. (2010). Modelling of Weld and Adhesive Connections in Crashworthiness Applications with LS-DYNA. *NAFEMS Seminar: "Simulation of Connections and Joints in Structures"*.

Kirov, G., Grabner, F., Fellner, B., Mukeli, E., & Khalil, Z. (2014). Numerical and Experimental Investigating on Adhesive Joint Parts for Crash Applications. *LS-DYNA forum*.

Livermore Sofware Technology Corporation (LSTC). (2016). *LS-Dyna® Keyword User's Manual.*

Matzenmiller, A., & Burbulla, F. (2008). Kontinuumsmechanische Modellierung von Stahlblechklebverbindungen für die FE-Crashanalyse. *LS-DYNA Anwenderforum*.

Matzenmiller, A., & Kühlmeyer, P. (2016). Temperature dependent TAPO model for failure analysis of adhesive bonds subjected to thermal service loading. *LS-DYNA Forum*.

Matzenmiller, A., Gerlach, S., & Fioka, M. (2006). Progressive Failure Analysis of Adhesively Bonded Joints in Crash Simulations. *LS-DYNA Forum*.

Meschut, G., Hahn, O., Klokkers, F., & Hein, D. (2012). Charakterisierung und Modellierung des Bruchverhaltens von Punktschweissverbindungen in pressgehärteten Stählen. *11th LS-DYNA Forum*.

Pap, J.-S., Kästner, M., Müller, S., & Jansen, I. (2013). Experimental characterization and simulation of the mechanical behavior of an epoxy adhesive. *Procedia Materials Science 2*.

Petrie, E. M. (1999). *Handbook of Adhesives and Sealants.* McGraw-Hill Handbooks.

Seeger, F., Feucht, M., Frank, T., Keding, B., & Haufe, A. (2015). An Investigation on Spot Weld Modelling for Crash Simulation with LS-DYNA. *LS-DYNA Anwenderforum*.

Teutenberg, D., Meschut, G., Schlimmer, M., Kroll, U., & Matzenmiller, A. (2013). Testing, Material Data and identification of model parameters for toughened structural adhesives. *Universität Paderborn*.

Zienkiewicz, O., Taylor, R., & Zhu, J. (2013). *The Finite Element Method: Its Basis and Fundamentals.* Butterworth-Heinemann.